

Studying Greenland Ice Sheet Mass Balance Using the Mascon Approach

Jiangjun Ran et al.

Map Content Number: GS(2023)0309 号

Responsible Editor: Han Peng, Cui Yan

ISBN 978-7-03-074440-1

Copyright© 2024 by Science Press

Published by Science Press

16 Donghuangchenggen North Street

Beijing 100717, P. R. China

Printed in Beijing

All rights reserved. No part of this publication may be reproduced, stored in a retrieval system, or transmitted in any form or by any means, electronic, mechanical, photocopying, recording or otherwise, without the prior written permission of the copyright owner.

Authors

Jiangjun Ran Pavel Ditmar Roland Klees
Min Zhong Yun Xiao Liming Jiang

Preface

This book is a compilation of my Ph.D. thesis at Delft University of Technology, and my representative research papers published in *The Cryosphere*, *Journal of Geophysical Research-Solid Earth*, *Journal of Geodesy*, and *Geophysical Journal International* under the common efforts of my colleagues and me during my worktime at the Institute of Geodesy and Geophysics, Chinese Academy of Sciences, Delft University of Technology, the Chinese University of Hong Kong, and Southern University of Science and Technology. Many thanks to my group members (Jinxian Yu and Zhipeng Zeng) for their participation in the correction and typesetting of this book.

The National Natural Science Foundation of China (42322403, 41974094, 42174096) and the National Key Research and Development Program of China (No.2017YFA0603103) are acknowledged here for the financial support of this book.

Jiangjun Ran
Shenzhen, China
November 23, 2023

Abstract

The Greenland Ice Sheet (GrIS) is currently losing mass, as a result of complex ice-climate interaction mechanisms that need to be understood for reliable projections of future sea-level rise. The thesis focuses on the estimation of mass anomalies in Greenland using data from the GRACE satellite gravity mission. Monthly GRACE gravity field solutions are post-processed using a new variant of the “mascon approach”. Greenland is covered by several distinctive “mascons”, assuming that mass anomalies within each mascon are laterally-homogeneous.

Gravity disturbances at the mean satellite altitude are synthesized from the GRACE spherical harmonic coefficients. They are used as pseudo-observations to estimate the mascon mass anomalies using weighted least-squares techniques. No regularization is applied. The full noise covariance matrix of the gravity disturbances is propagated from the full noise covariance matrix of the spherical harmonic coefficients using the law of covariance propagation. These matrices represent a complete stochastic description of random noise in the data, provided that it is Gaussian. The inverse noise covariance matrix is used as a weight matrix in the weighted least-squares estimation of the mascon mass anomalies. The limited spectral content of the gravity disturbances is accounted for by applying a low-pass filter to the design matrix, resulting in a spectrally consistent functional model.

Using numerical experiments with simulated signal and data, we demonstrate the importance of the data weighting and of the spectral consistency between the mascon model and the pseudo-observations. The developed methodology is applied to process real GRACE data using CSR RL05 monthly gravity field solutions with full noise covariance matrices. We distinguish 5 GrIS drainage systems. The obtained mass anomaly estimates per mascon are integrated over individual drainage systems, as well as over the whole of Greenland. We find that using a weighted least-squares estimator reduces random noise in the estimates by factors ranging from 1.5 to 3.0, depending on the drainage system. Furthermore, we compare the detrended mascon mass anomaly time-series with similar time-series from the Regional Atmospheric Climate Model (RACMO 2.3), which describes the Surface Mass Balance (SMB). We show that the weighted least-squares estimate reduces the discrepancies between the time-series by 24%–47%.

We then combine GRACE mass anomaly estimates, SMB model results, and ice discharge data to systematically analyze the mass budget of Greenland at different temporal and spatial scales. Among other things, we reveal a substantial seasonal meltwater storage, which peaks in July and reaches a total of 100 ± 20 Gt. Meltwater storage is particularly intense in the northern, northwestern and southeastern drainage systems. An analysis of outlet glacier velocities shows that the contribution of ice discharge to the seasonal mass variations is small, at a level of only a few Gt. In addition, we propose a simple way to use GRACE data to validate SMB model outputs in winter, based on the fact that ice discharge cannot be negative.

Currently, there are several research groups producing different mascon products from the GRACE data, such as Jet Propulsion Laboratory (JPL), Center for Space Research (CSR), and Goddard Space Flight Center (GSFC). However, there are noticeable discrepancies between these mascon products. We try to analyze the reasons for the discrepancies, by varying the regularization parameter when estimating mass anomalies using our variant of the mascon approach. Using both real data and simulations, we show that the observed discrepancies are likely dominated by differences in the applied regularization. Thereafter, we find that the quality of the mascon estimates in GrIS can be improved by 11%–56% by using an appropriate choice of the regularization parameter. The trend estimates for the South-West (SW) drainage system from the GOCO-06S model and the Input-Output Method are used as independent data, to validate the mascon-based solutions. It is found that the trends from CSR, JPL, and our estimates obtained with the modified spatial constraints are in good agreement with the independent data.

Finally, we use numerical simulations and real data to identify the optimal GRACE data processing strategy (primarily the size of the mascons) for three temporal scales of interest: monthly mass anomalies, mean mass anomalies per calendar month, and long-term linear trends. We show that the two main contributors to the error budgets are random errors and parameterization (model) errors; the latter are caused by a spatial variability of actual mass anomalies within individual mascons. We find that the errors in long-term linear trend estimates are mainly caused by the parameterization errors, and that accurate estimates require small size mascons in combination with the ordinary least-squares estimator. The error budget of the mean mass anomalies per calendar month is dominated by the parameterization error when the mascons are large, and by random errors otherwise. Thus, accurate estimates require mascons of intermediate size in combination with a weighted least-squares estimator. Finally, we find that random errors are the dominant error source in monthly mass anomalies. In this case, we advise

to use large mascons and a weighted least-squares estimator.

Our new variant of the mascon approach and the results of this book can be used to support future research on GrIS hydrology, glacier dynamics, and surface mass balance, as well as their mutual interactions.

Contents

Preface

Abstract

1 Challenges and opportunities of mass variations in Greenland	1
1.1 Climate change and ice melt in Greenland	1
1.2 Contemporary challenges	3
1.3 Opportunities	4
2 GrIS mass variation: an overview	7
2.1 Introduction	7
2.2 GrIS Glaciers	7
2.3 Mass balance of the Greenland Ice Sheet	8
2.4 GrIS mass variation estimation	9
2.4.1 Altimetry	9
2.4.2 The input-output method (IOM)	10
2.4.3 Satellite gravimetry	11
2.4.4 Comparison of GrIS mass anomalies estimated by different methods	12
2.5 Summary	13
3 GRACE post-processing methodologies: an overview	15
3.1 Introduction	15
3.2 Towards high spatial resolution methodologies	15
3.2.1 The mascon approach by Luthcke et al. (2006a)	16
3.2.2 The mascon approach by Luthcke et al. (2013)	17
3.2.3 The mascon approach by Sasgen et al. (2010)	18
3.2.4 The mascon approach by Schrama and Wouters (2011)	19
3.2.5 The mascon approach by Baur and Sneeuw (2011)	20
3.3 Summary	21
4 Statistically optimal estimation of Greenland Ice Sheet mass variations from GRACE monthly solutions using an improved mascon approach	23
4.1 Introduction	23
4.2 Methodology	26
4.2.1 Gravity disturbances	26
4.2.2 Parameterization	29
4.2.3 Distribution of data points	30

4.2.4	Data inversion	31
4.3	Numerical experiments	32
4.3.1	Experimental setup	32
4.3.2	Choice of the optimal data processing strategy	36
4.3.3	Spectral consistency	43
4.4	Real GRACE data analysis	46
4.4.1	Estimating mass anomaly uncertainties	47
4.4.2	Validation against modelled SMB time-series	48
4.4.3	Comparison with Greenland mass anomalies from other studies	52
4.5	Summary	54
5	Seasonal mass variations show timing and magnitude of meltwater storage in the Greenland Ice Sheet	57
5.1	Introduction	57
5.2	Adopted parameterization	59
5.3	Data	60
5.3.1	Ice discharge on multi-year scale	60
5.3.2	Ice discharge on intra-annual scale	60
5.4	Results and Discussion	63
5.4.1	Multi-year mass trend and acceleration budgets	63
5.4.2	Seasonal mass variations	67
5.5	Summary	76
6	Analysis and mitigation of biases in Greenland Ice Sheet mass balance trend estimates from GRACE mascon products	79
6.1	Introduction	79
6.2	Methods	81
6.2.1	Variant of the mascon approach adopted to estimate mass anomalies	81
6.2.2	Adopted spatial constraints	82
6.3	Data	85
6.3.1	GRACE	85
6.3.2	RACMO2.3	86
6.4	Results	86
6.4.1	Understanding the discrepancies between the CSR, JPL and GSFC mascon products	86
6.4.2	Numerical study to analyze regularization-driven biases in mascon-type estimates	89
6.4.3	Improved spatial constraints	92
6.5	Discussion	98
6.5.1	Global mass conservation	98

6.5.2 “Improved” regularization vs regularizations applied to other mascon solutions	98
6.5.3 Added value of the “improved” regularization	99
6.6 Summary	99
7 Optimal mascon geometry in estimating mass anomalies within Greenland from GRACE	103
7.1 Introduction	103
7.2 Methodology and parameterization	104
7.2.1 Adopted mascon approach	104
7.2.2 Parameterization of Greenland	105
7.3 Numerical study	107
7.3.1 Experimental set-up	107
7.3.2 Results	111
7.4 Analysis based on real GRACE data	126
7.4.1 Analysis of long-term linear trends	128
7.4.2 Analysis of the estimates at the intermediate and short time scales	130
7.5 Summary	134
8 Conclusions	137
References	143
A Eigenvalue decomposition of the noise covariance matrix C_d	153
B Robustness of GRACE-based estimates at the intra-annual time scale	157
C Supporting Information for Chapter 6	161

1

Challenges and opportunities of mass variations in Greenland

1.1. Climate change and ice melt in Greenland

The Earth's climate is changing rapidly, including sea level rise, with potentially severe impacts on coastal areas around the world. A major contribution to sea level rise is the melting of ice of the Greenland Ice Sheet (GrIS) and the Antarctic Ice Sheet (AIS). Over the past 10 years, the GrIS has become one of the largest contributors to sea level rise, accounting for 0.7–1.1 mm/yr out of 3.2 mm/yr (see e.g., Shepherd et al., 2012; Jacob et al., 2012; Stocker et al., 2013; Moon et al., 2014; Khan et al., 2015).

The GrIS, with an area of about 1, 710, 000 square kilometers, is smaller than the AIS, but its mass loss rate is much greater than that of the AIS. More importantly, there are indications that the GrIS mass loss has accelerated in the last 15 years (Velicogna and Wahr, 2006; Velicogna, 2009; Velicogna et al., 2014; Schrama et al., 2014). If this trend continues, its contribution to the overall sea level budget will become more significant in the future. Therefore, the state of the GrIS is receiving increasing attention from the scientific community (Khan et al., 2015).

The GrIS mass loss is a combined effect of ice discharge and changes in surface mass balance (SMB). Ice discharge refers to the dynamic loss of ice from outlet glaciers. It is usually derived from ice flow velocities provided by satellite Interferometric Synthetic Aperture Radar (InSAR) data and ice thickness measurements at flux gates. It can also be simulated by ice flow models, such as the Ice Sheet System Model (ISSM) (Larour et al., 2012). Ice discharge manifests itself as a long-term trend with small seasonal variations (van den Broeke et al., 2009). SMB is defined as the residual of total precipitation (rain and snow), meltwater runoff, and sublimation. SMB-related mass changes of the GrIS vary in time and space. Most of them are concentrated in the narrow coastal areas of Greenland and show strong inter- and intra-annual variations. SMB-related mass

changes can be simulated by a climate model, such as the Regional Atmospheric Climate Model (RACMO 2.3) (Noël et al., 2015) and the Community Earth System Model (CESM) (Gent et al., 2011). Future projections of both ice discharge and SMB-related mass changes are based on models. Even a small bias in a model can have a large impact on future projections. Therefore, the proper validation and calibration of the models are critical.

For this purpose, satellite gravimetry is one of the best sources of independent information on the mass change of the GrIS, as it is the only method that directly measures mass changes over time, with only a limited number of assumptions. In this book, satellite gravimetry refers to measurements from the Gravity Recovery And Climate Experiment (GRACE) satellite gravity mission, as it is the only satellite gravity mission that, can continuously monitor Earth's mass variations with relatively high spatial and temporal resolutions. Typically, GRACE data are used to compute monthly gravity field solutions consisting of Spherical Harmonic Coefficients (SHCs) that are complete to a certain maximum, e.g., 96 for the CSR RL05 solutions (Bettadpur, 2012) or 90 for the GFZ RL05 solutions (Dahle et al., 2012). Alternatively, monthly gravity solutions in terms of mass anomalies per mass concentration block ("mascon") have also been released by the Jet Propulsion Laboratory (JPL) (Watkins et al., 2015), the Goddard Space Flight Center (GSFC) (Luthcke et al., 2013) and CSR (Save et al., 2016). To clean the monthly SHCs from the contribution of high-frequency mass variations, model of ocean tides (e.g., EOT11a (Savcenko and Bosch, 2010)), a model of non-tidal components of the atmospheric and oceanic mass variations (e.g., the Atmosphere and Ocean De-aliasing model (AOD) (Dobslaw et al., 2013)), and other background models are routinely being used. Since the sensitivity of GRACE is anisotropic, the monthly SHCs are strongly contaminated by north-south "stripes". The amplitude of the "stripes" depends on the latitude with smaller amplitudes in the polar regions and larger amplitudes near the equator.

The conversion of the gravity field variations into mass anomalies at the Earth's surface can be done and appropriate scaling of the SHCs (Wahr et al., 1998). To suppress stripes and high-frequency noise in the solutions, low-pass filters and/or destriping schemes are frequently used (Jekeli, 1981; Wahr et al., 1998; Swenson and Wahr, 2006). Problems caused by spatial filtering include a reduction in spatial resolution, distortions of the derived mass anomalies, and signal leakage into areas surrounding the area where the mass change occurred (Bonin and Chambers, 2013).

As an alternative to estimating SHCs, mass anomalies can be estimated for a set of

predefined regions called "mascons". Low-pass filters and de-striping can be avoided in the mascon approach. High-frequency noise in the SHCs is suppressed by making some realistic assumptions, like the one that a mass anomaly as a function of geographic coordinates is constant within a given mascon. Furthermore, the geometry of the mascons can be chosen to take into account available physical constraints, like the geometry of the coastal line. All this mitigates signal distortions and can allow for a relatively high spatial resolution. A side effect of the mascon approach, however, is that it comes with a parameterization error, i.e., a mismatch between the assumption of uniformly mass distribution within each mascon and the continuous mass change signal in reality.

Originally, the mascon representation was proposed by Muller and Sjogren (1968) in their efforts to model the static gravity field of the Moon. Luthcke et al. (2006a) used this idea to derive mass anomalies from GRACE K-band Ranging (KBR) data. Variations of the mascon approach using monthly solutions in terms of SHCs as input have been proposed by Forsberg and Reeh (2007), Baur and Sneeuw (2011) and Schrama and Wouters (2011). According to them, monthly SHCs are used to synthesize gravity data (e.g., gravity disturbances, water thickness values). Then the mass anomalies per mascon are derived by means of a least-squares adjustment.

During the last 10 years, GRACE data have been widely used to investigate the mass balance of GrIS. Velicogna and Wahr (2005) were the first to derive the ice loss rate for 2002–2004, which was -75 ± 26 Gt/yr. After this, Velicogna and Wahr (2006) and Chen et al. (2006) reported that GrIS was losing mass with an acceleration in the southern part. In 2003–2013, the linear mass loss trends of GrIS estimated by both Velicogna et al. (2014) and Schrama et al. (2014) were about -280 Gt/yr, which is equivalent to ~ 0.8 mm/yr of sea level rise. The mass loss is concentrated in the northwest and southeast parts of Greenland.

1.2. Contemporary challenges

Although previous works have provided much new information about the GrIS mass balance, there are still many open questions that require further investigation. First, by now, most of the studies on the mass balance of the GrIS using GRACE focus on either the long-term trend or the acceleration (see e.g., Chen et al., 2006; Wouters et al., 2008; van den Broeke et al., 2009; Baur and Sneeuw, 2011; Jacob et al., 2012; Shepherd et al., 2012; Wouters et al., 2013; Velicogna et al., 2014; Schrama et al., 2014). To better understand mass changes of the GrIS and the associated control mechanisms,

an investigation of the intra-annual mass variation of the GrIS is required.

Second, mass anomalies obtained by the existing variants of the mascon approach are statistically suboptimal, in the sense that the spatial correlations of the random noise in the SHCs are not taken into account. This random noise is highly correlated due to the aforementioned anisotropic sensitivity of GRACE. However, so far, it is not yet known to what extent mass anomalies of the GrIS are improved by taking the noise correlations into account.

Furthermore, the spectrum of the synthesized GRACE-based gravity data is limited to the maximum spherical harmonic degree of the monthly solutions, while the mascon representation is more flexible in this sense. However, when using mascons, one has to explicitly enforce a spectral consistency between the monthly GRACE solution and the functional model. This has not been done yet.

Finally, when mascons are used, the estimated mass anomalies strongly depend on the chosen parameterization, i.e., the number and the geometry of the mascons. In the past, two typical approaches to the parameterization have been used. A commonly-used "geophysical" approach is based on the geometry of GrIS drainage systems. In this case, each mascon is formed as a combination of several neighboring drainage systems. For example, Luthcke et al. (2006a) divided GrIS into 6 mascons. Each mascon was further devided into two parts: above and below 2000 m elevation. A disadvantage of this approach is that it is not flexible enough. The mascon size is defined a priori and can hardly be adjusted in line with the actual spatial resolution of the GRACE data. Another common approach is "geometric": the GrIS is divided into blocks of a regular shape (e.g., equal angles or equal area) (Rowlands et al., 2005; Baur and Sneeuw, 2011; Luthcke et al., 2013; Schrama et al., 2014). In this case, however, it is problematic to take into account the geometry of the coast line. An additional disadvantage of equal-angular blocks is that their areas depend on the latitude: the blocks in the north of Greenland are much smaller than those in the south of Greenland. This does not allow to choose of a parameterization of the GrIS that is optimally adapted to the spatial resolution of the GRACE data. Therefore, the optimal parameterization of the GrIS still needs further investigation.

1.3. Opportunities

The primary goal of this book is to better understand the mass balance of the GrIS at high

spatial resolution using satellite gravimetry, supported by satellite altimetry, a regional climate model, and InSAR data. To that end, we

- investigate the intra-annual mass variations for the whole GrIS and for individual drainage systems, by combining GRACE- and SMB- based estimates.
- derive statistically-optimal mass anomalies from monthly GRACE level-2 products. For this purpose, we develop an adapted mascon approach based on the mascon variants proposed by Forsberg and Reeh (2007) and Baur and Sneeuw (2011), which uses the full noise covariance matrix of the monthly SHCs and propagates them into the full-noise variance covariance matrices of the synthesized gravity data using the law of covariance propagation. The latter are used to estimate the mascon coefficients using weighted least-squares techniques.
- reformulate the functional model of the mascon approach to make it spectrally consistent with the monthly SHCs.
- understand the performance of the proposed methodology, by conducting a well-designed numerical study and validating the results with independent data.
- propose a parameterization of the GrIS that better exploits the resolution of the GRACE data, by taking into account appropriate physical constraints.
- investigate the optimal choice of the mascon size depending on temporal scale.

The book is organized as follows.

Chapter 2 briefly describes the types and distribution of glaciers of the GrIS. The methods currently used to estimate the mass anomalies of the GrIS, i.e., satellite altimetry, the input-output method and satellite gravimetry, are then briefly discussed. More importantly, the state-of-the-art of the mass balance of the GrIS estimated by different methods is also discussed. It should be noted that this chapter is dedicated to a general review of what is known about the state of the GrIS. More detailed introductions of different research questions are given in later chapters.

Chapter 3 focuses on a review of the mascon approach and its variants, which aim to estimate the mass variations of the GrIS from GRACE data with a high spatial resolution. In particular, the advantages and disadvantages of each variant are discussed in detail.

In order to produce statistically-optimal mass anomaly estimates of GrIS from monthly SHCs, an adapted mascon approach is developed in Chapter 4. Novel elements include the optimal data weighting, a scheme for an automatically dividing the GrIS into mascons of equal area, and the spectral consistency of the functional model with monthly SHCs. The GrIS mass anomalies obtained with this approach are then validated with independent estimates produced by RACMO 2.3.

Using the optimal data processing scheme, the seasonal mass anomalies of the GrIS are obtained from GRACE in Chapter 5. In particular, it is discussed to what extent the SMB contributes to the total mass variations observed by GRACE at intra-annual scales. Furthermore, using multi-year ice discharge observations, this chapter presents an attempt to close the budgets of long-term linear trends and accelerations of GrIS mass variations. Based on the monthly ice discharge computed by ice velocities and ice thickness values of outlet glaciers, the contribution of ice discharge seasonality to variations of the Greenland mass balance during summer is quantified.

The analysis of different mascon products from the GRACE data reveals remarkable discrepancies between them. Therefore, Chapter 6 is dedicated to analyze the causes of these discrepancies, by varying the regularization parameter when estimating mass anomalies using the variant of the mascon approach proposed by Ran et al. (2018a). A novel modification of the spatial constraint is introduced to minimize the signal leakage.

In order to understand the optimal parameterization, Chapter 7 analyzes the impact of the parameterization on the mass anomaly estimates from GRACE at different time scales, i.e., monthly, intra-annual and multi-year scales.

2

GrIS mass variation: an overview

2.1. Introduction

The ongoing mass loss of the GrIS has drawn the attention of the scientific community, due in part to its potential to exacerbate future sea level rise. In this chapter, we first review the types of glaciers in Greenland and their distribution. Next, an introduction to the GrIS mass balance is given. After that, the methods used to estimate the GrIS mass variations are discussed. Note that this chapter aims to give a basic overview of GrIS mass balance. Further information related to each specific research question is presented in the introductory section of later chapters.

2.2. GrIS Glaciers

Outlet glaciers of the GrIS can be divided into land-terminating glaciers, ice-shelf-terminating glaciers, and marine-terminating glaciers (cf. Fig. 2.1). A land-terminating glacier has a terminus on land. On Greenland, the land-terminating glaciers are mainly located in the southwest, although a few are also located in the northeast. Their velocities are around 10–100 m/yr (Moon et al., 2012). An ice-shelf-terminating glacier means a glacier with floating tongue in the ocean. There are only a few large ice-shelf-terminating glaciers on Greenland, mainly in the northern part of Greenland. Mean velocities of ice-shelf-terminating glaciers are generally around 300–1670 m/yr. Marine-terminating glaciers, like ice-shelf-terminating glaciers, have termini in the ocean, but do not form floating tongues. Marine-terminating glaciers, like ice-shelf-terminating glaciers, have termini in the ocean, but do not form floating tongues outside the grounding line. Note that the grounding line is the boundary where the floating tongue begins. Most of the glaciers in GrIS are marine-terminating glaciers and are common in the northwest and southeast of Greenland. The mean velocities of the marine-terminating glaciers are 2830 m/yr and 1630 m/yr, respectively (Moon et al., 2012). Some glaciers in the northern part of Greenland are also marine-terminating. However, their

flow velocities are quite low, i.e., <200 m/yr.

2

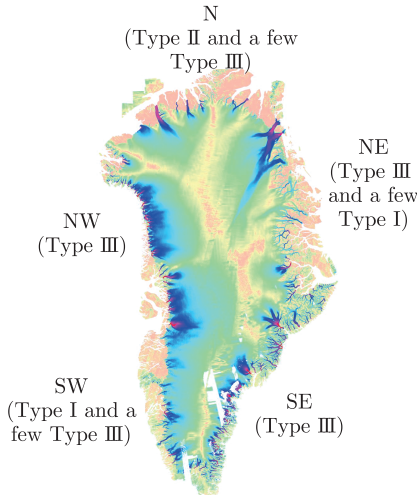


Figure 2.1 Schematic view of three types of GrIS outlet glaciers. Type I stands for land-terminating glaciers, whereas Type II and III refer to ice-shelf-terminating glaciers and marine-terminating glaciers, respectively. The velocity map over 2007–2010 by Moon et al. (2012) is shown as a background.

2.3. Mass balance of the Greenland Ice Sheet

This section is dedicated to the mass balance of the GrIS, which can be divided into two parts, i.e., the surface mass balance and the ice discharge. As shown in Fig. 2.2, the GrIS gains mass from snowfall (~94%) and rainfall (~6%) (Ettema et al., 2009). Some of the rainwater runs off, while some infiltrates into deeper layers. The snow at the top of a glacier gradually becomes firn, and is eventually compacted as ice. The surface mass balance also depends on the processes related to ablation, such as runoff (~90%) and sublimation/evaporation (~10%) (Ettema et al., 2009). During periods of positive air temperature and strong solar radiation, some of snow/ice melts and becomes liquid water. The melt water is divided into two parts. One part forms surface runoff. The other part percolates into deeper layers, where much of the water is refrozen or retained. In addition, there is still water that penetrates to the ice-bedrock interface and forms deep runoff.

In summary, the GrIS accumulates mass via snowfall (SN) and rainfall (RA) and loses mass by melt water runoff (RU), sublimation (SU), evaporation (EV), and ice discharge

(ID). By comparing the input and output using Eq. (2.1), the mass balance of the GrIS, $\frac{dM}{dt}$, can be written as

$$\frac{dM}{dt} = SN + RA - SU - RU - EV - ID. \quad (2.1)$$

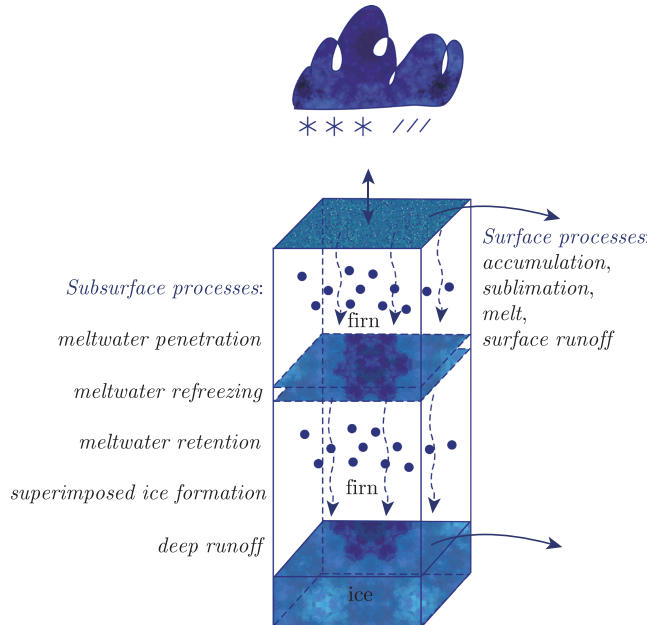


Figure 2.2 Processes represented by the surface mass balance model (Ettema et al., 2009).

2.4. GrIS mass variation estimation

The widely used tools to estimate the mass balance of the GrIS are satellite altimetry, the input-output method (IOM), and satellite gravimetry (see e.g., Zwally, 2002; van den Broeke et al., 2009; Tapley et al., 2004). A brief introduction to the three methods is given below.

2.4.1. Altimetry

Since 1978, space-borne radar missions have been widely used to derive the surface elevation changes of polar ice sheets (Wingham et al., 1998; Davis, 1998). The only dedicated ice radar altimetry missions are Envisat (2002–2012) and Cryosat-2 (2010–). The only laser altimetry satellite mission to date is ICESat. A short description of ICESat

is given below, as data from this mission are used in this book.

2

ICESat was launched in 2003 and ended in 2010. Its main scientific objectives were to investigate the mass variations of the GrIS and the AIS and their contributions to global sea level rise (Zwally, 2002). Using the on-board Geoscience Laser Altimeter System (GLAS), ICESat could accurately measure the two-way travel time of the pulse sent from one of the three lasers, and thus the distance between the satellite and the surface.

Satellite laser altimetry can detect long-term changes in the surface elevation of the ice sheet. Mass changes are derived by multiplying the surface elevation changes with the firn/ice mass densities. The advantage of satellite laser altimetry is that it can reach a relatively high spatial resolution of a few kilometers. However, it has several shortcomings. First, when converting the surface elevation changes to mass changes, the densities of the components (i.e., snow, firn, and ice) at the location where the elevation changes are measured need to be known. However they are difficult to determine accurately. Second, the compaction of snow and firn also causes elevation changes, but is not related to any mass change. Therefore, corrections for compaction need to be applied. Third, laser altimetry cannot collect data in the presence of cloud cover. Finally, the temporal coverage of the ICESat mission was rather limited.

The multi-year mass loss of the GrIS has been investigated in many studies based on ICESat data. For example, Sørensen et al. (2011) reported that the ICESat-based mass balance estimates over 2003–2008 are in the range of -191 ± 23 Gt/yr to -240 ± 28 Gt/yr, depending on different processing schemes. However, a much smaller estimate of -139 ± 68 Gt/yr for 2003–2007, was obtained by Slobbe et al. (2009). More recently, Shepherd et al. (2012) estimated a linear mass change trend for the entire GrIS of -185 ± 24 Gt/yr over the period October 2003 to December 2008.

2.4.2. The input-output method (IOM)

The IOM obtains the mass balance by examining the surface mass balance (SMB) and ice discharge separately. In order to quantify the SMB, a SMB model is widely used to account for the input and the output, as shown in Fig. 2.3. One of the most popular SMB models is the regional atmospheric climate model (RACMO) (Ettema et al., 2009), whose output is used in this book to describe the SMB-based mass changes of GrIS. Based on RACMO, Velicogna et al. (2014) obtained a contribution of SMB to the long-term trend of the GrIS of -180 ± 33 Gt/yr over the years 2003–2012 relative with respect to the reference period 1961–1990.

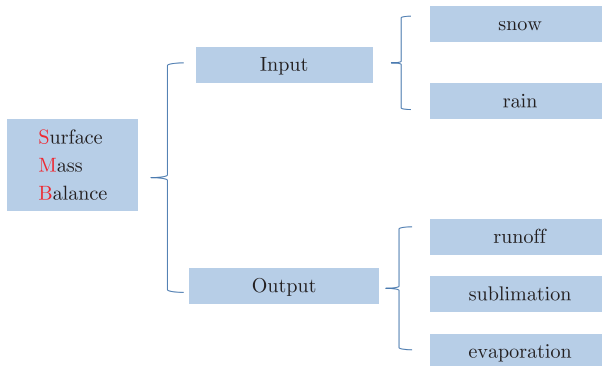


Figure 2.3 Surface mass balance components

Ice discharge can be derived from ice flow velocities \mathbf{V} and ice thickness T at the flux gates of outlet glaciers,

$$\text{ID} = \int_p \mathbf{V} T d\mathbf{p}, \quad (2.2)$$

where $d\mathbf{p} = d\mathbf{p} \cdot \mathbf{n}$, \mathbf{n} is the unit normal vector of the flux gate. A flux gate \mathbf{p} stands for a cross-section of a glacier that is used to evaluate the glacier's ice discharge. Many attempts have been made to estimate the mass balance of the GrIS using IOM, after the pioneering study conducted by Thomas et al. (2000). For example, van den Broeke et al. (2009) estimated the mean GrIS mass loss rate for 2003–2008 to be -237 ± 20 Gt/yr. Recently, by using the image data of the Landsat 7 Enhanced Thematic Mapper Plus and the Advanced Space-borne Thermal and Reflectance Radiometer (ASTER), Enderlin et al. (2014) derived the ice flow velocities for about 178 outlet glaciers. After combining this information with the ice thickness profiles (Korona et al., 2009), they estimated the annual ice discharge of the GrIS to be at an average level of around 535 Gt/yr from 2005 to 2012. By combining this estimate with the SMB-based mass changes from RACMO, they found that the mass change trend of the GrIS was -378 Gt/yr over the period 2009–2012. The difference with the estimate by van den Broeke et al. (2009) may be caused by an on-going acceleration of GrIS mass anomalies.

2.4.3. Satellite gravimetry

In 2002, the Gravity Recovery and Climate Experiment (GRACE) satellite mission was launched to measure the gravity field of the Earth. Its results are used extensively in this dissertation to investigate the mass variations of the GrIS. The GRACE mission consists of two identical satellites flying in the same orbit separated by about 200 km. GRACE is the first satellite gravimetry mission to use an accurate inter-satellite ranging

system to measure variations in the distance between the two satellites with micrometer accuracy. In addition, the on-board accelerometers can measure the non-gravitational accelerations of the satellites to an accuracy of about 3.0×10^{-10} m/s². These two instruments make GRACE capable for measuring the Earth's mass re-distribution with an unprecedented accuracy and spatial temporal resolution of about ~ 300 by 300 km and one month, respectively.

GRACE directly measures the total mass variations of the GrIS without any additional assumptions about the density of the firm. However, GRACE cannot distinguish GrIS mass anomalies from the Glacial Isostatic Adjustment (GIA) signal, which is triggered by the non-elastic rebound of the Earth caused by a relief of ice load, from the mass variations of the GrIS. Usually, the effect of GIA is corrected by models (A et al., 2013; Simpson et al., 2009).

In the early time, there were some differences among the linear trends estimated by different researchers, e.g., -219 ± 21 Gt/yr over 2002–2005 by Chen et al. (2006), -230 ± 33 Gt/yr over 2002–2009 by Velicogna (2009), -179 ± 25 Gt/yr over 2003–2008 by Wouters et al. (2008), etc. However, by now, the differences have been largely eliminated. For instance, Velicogna et al. (2014) and Schrama et al. (2014) provided very similar estimates of a linear mass change trend of GrIS over the period 2003–2013 as -280 ± 59 Gt/yr and -278 ± 19 Gt/yr, respectively. Most of the mass loss occurred in the southeastern and northwestern parts of Greenland, while little mass gain was observed in the interior of Greenland. It is also worth mentioning that there are indications from GRACE data that the GrIS is losing mass at an acceleration of ~ 31 Gt/yr², which concentrates in the southeast and northwest of Greenland (Schrama et al., 2014; Velicogna et al., 2014).

2.4.4. Comparison of GrIS mass anomalies estimated by different methods

The three methods mentioned above, i.e., IOM, satellite laser altimetry and gravimetry, have their own strengths and weaknesses. In general, the mass anomalies obtained by these methods show some agreement (Slobbe et al., 2009; Ettema et al., 2009; van den Broeke et al., 2009; Sørensen et al., 2011; Velicogna et al., 2014; Enderlin et al., 2014; Schrama et al., 2014). For example, all of them observed large mass variations in the coastal areas of Greenland, while relatively small mass gains were found in the inner part. Furthermore, the northwest and southeast parts of Greenland were identified by all methods as the two largest contributors to the total GrIS mass loss, while the northern, southwest and northeast parts contributed less.

However, some differences were also observed among the mass estimates of GrIS by the three methods. The intercomparison study conducted by Shepherd et al. (2012) provided a good opportunity to understand the differences in GrIS mass anomalies estimated by different methods. The time interval chosen was the period from October 2003 to December 2008 because both the laser altimetry satellite and the gravimetry satellite were operating optimally during this period (Shepherd et al., 2012). The trends of GrIS mass anomalies derived by IOM, satellite laser altimetry, and gravimetry were -284 ± 65 Gt/yr, -185 ± 24 Gt/yr and -228 ± 30 Gt/yr, respectively (Shepherd et al., 2012). Note that the mass loss trend observed by GRACE was obtained by averaging the estimates obtained by different groups (Shepherd et al., 2012). The trend inferred from the laser altimetry data is the smallest one; it is 19% and 35% smaller than the estimates from IOM and gravimetry, respectively. This might be caused by the large uncertainty of firn density, which was used to convert the volume changes to mass changes.

2.5. Summary

There are three types of glaciers in GrIS, land-terminating glaciers, ice-shelf-terminating glaciers and marine-terminating glaciers. At present, the mass variations of GrIS are estimated using three methods, i.e., satellite altimetry, IOM and satellite gravimetry. Surface elevation changes with a high spatial resolution are provided by satellite altimetry. However, converting the elevation changes to mass changes requires a model of the ice/firn densities, and model errors contribute to the overall error budget. The IOM models the physical surface processes, which helps to understand the mechanism of GrIS mass variations. However, information on ice thickness and flow velocities is required, which is usually difficult to obtain in practice. Satellite gravimetry is able to measure the mass changes directly without any assumptions, but its spatial resolution is limited to about 300 km, and corrections for GIA have to be applied.

3

GRACE post-processing methodologies: an overview

3.1. Introduction

The monthly gravity field solutions delivered by GRACE are one of the most valuable sources of information on the mass variations of the GrIS (see e.g., Velicogna and Wahr, 2006; Chen et al., 2006; Velicogna, 2009; Velicogna et al., 2014; Schrama et al., 2014). Unfortunately, the monthly GRACE SHCs are highly contaminated by random noise. This is due to the fact that GRACE measures mass variations anisotropically, i.e., GRACE data are more sensitive to mass variations in the along-track direction than to those in the cross-track direction. To minimize errors in the estimation of mass anomalies, many post-processing approaches have been proposed, such as the de-striping scheme (Swenson and Wahr, 2006), the basin-averaging technique (Velicogna, 2009), and the mascon approach (Forsberg and Reeh, 2007; Baur and Sneeuw, 2011; Schrama and Wouters, 2011; Schrama et al., 2014). We also develop a software called ANGELS-PS3 that integrates different post-processing methods for GRACE data (<https://github.com/JiangjunRAN/ANGELS-PS3>). Due to its ability to achieve higher spatial resolution and reduced signal leakage, the mascon approach has become one of the most popular methods for GRACE data post-processing. In this chapter, the mascon approach and its variants are reviewed, and their advantages and disadvantages are discussed.

3.2. Towards high spatial resolution methodologies

The mascon approach typically assumes that the mass variation is uniform within each mascon. This idea originates from Muller and Sjogren (1968), who modelled the static gravity field of the Moon. Then, it was applied to estimate surface mass variations of the GrIS from GRACE Level 1B data (Luthcke et al., 2006a). After that, the mascon approach was further developed to deal with GRACE Level 2 data, i.e., monthly SHCs, by Forsberg

and Reeh (2007), Sasgen et al. (2010), Baur and Sneeuw (2011), Schrama and Wouters (2011) and Schrama et al. (2014). A summary of each mascon approach variant is given in Sect. 3.2.1 to 3.2.5.

3.2.1. The mascon approach by Luthcke et al. (2006a)

Let's assume that a mass variation takes place in a mascon W at time t at the Earth surface. Then, the mass variation can be represented by a set of differential SHCs ($\Delta\bar{C}_{lm}^{(W)}(t)$, $\Delta\bar{S}_{lm}^{(W)}(t)$) relative to a prior mean static gravity field model (Luthcke et al., 2006a; Rowlands et al., 2010). The relation between the differential SHCs and the surface density $\sigma^{(W)}(t)$ of mascon W is

$$\begin{aligned}\Delta\bar{C}_{lm}^{(W)}(t) &= \frac{\sigma^{(W)}(t)(1+k_l)a^2}{(2l+1)M} \int_W \bar{P}_{lm}(\sin\phi) \cos m\lambda d\Omega \\ \Delta\bar{S}_{lm}^{(W)}(t) &= \frac{\sigma^{(W)}(t)(1+k_l)a^2}{(2l+1)M} \int_W \bar{P}_{lm}(\sin\phi) \sin m\lambda d\Omega,\end{aligned}\quad (3.1)$$

where M is the mass of the Earth; k_l is the loading Love number of degree l ; a is the semi-major axis of the reference ellipsoid; $d\Omega$ is a surface element of the unit sphere; (r, ϕ, λ) are spherical coordinates; \bar{P}_{lm} is the fully normalized associated Legendre function of degree l and order m .

After converting the surface mass density $\sigma^{(W)}(t)$ to the commonly used Equivalent Water Height (EWH) $H^{(W)}(t)$, Eq. (3.1) becomes

$$\begin{aligned}\Delta\bar{C}_{lm}^{(W)}(t) &= H^{(W)}(t) \frac{\rho_w(1+k_l)a^2}{(2l+1)M} \int_W \bar{P}_{lm}(\sin\phi) \cos m\lambda d\Omega \\ \Delta\bar{S}_{lm}^{(W)}(t) &= H^{(W)}(t) \frac{\rho_w(1+k_l)a^2}{(2l+1)M} \int_W \bar{P}_{lm}(\sin\phi) \sin m\lambda d\Omega,\end{aligned}\quad (3.2)$$

where ρ_w is the density of water. By combining Eq. (3.2) with the variational equations approach, which links the SHCs to the raw satellite-to-satellite tracking data, surface densities of mascons can be estimated using least-square techniques (Luthcke et al., 2006b; Rowlands et al., 2010). In order to stabilize the normal matrix, additional constraints in space and time are incorporated into the estimation process. The constraint equation for any mascon pair (I, J) is (Rowlands et al., 2010)

$$H^{(I)} - H^{(J)} = 0. \quad (3.3)$$

The weight of the constraint equation is defined as

$$WT^{(IJ)} = S \cdot \exp(2 - d^{(IJ)}/D - t^{(IJ)}/T), \quad (3.4)$$

where $d^{(IJ)}$ is the distance between the centers of mascon I and J ; D is the correlation distance, and T is time; $t^{(I)}$ and $t^{(J)}$ are the time tags of the mass variations taking place in the mascon I and J, respectively; $t^{(IJ)}$ is the difference of $t^{(I)}$ and $t^{(J)}$; S is a scale factor to adjust the weight of the constrain equation. For more details, we refer to Rowlands et al. (2010).

It is worth mentioning that two new variants of the mascon approach, which also estimate mass anomalies from GRACE Level 1B data, have recently been developed by Watkins et al. (2015) and Save et al. (2016). However, since the basic ideas are similar to the variant by Luthcke et al. (2006a), we do not discuss them in more detail. However, their main differences from Luthcke et al. (2006a) are briefly described below. The major difference of Watkins et al. (2015) is that they analytically link the KBRR to the unknown mascon parameters, instead of taking SHCs as an intermediate. The innovation of Save et al. (2016) is to use different spatial constraints which are purely extracted from GRACE information. For more detail, we refer to Watkins et al. (2015) and Save et al. (2016).

3.2.2. The mascon approach by Luthcke et al. (2013)

Luthcke et al. (2013) made an attempt to estimate solutions with higher accuracy, compared with the mascon approach by Luthcke et al. (2006a). The major methodological difference between the two variants is that the latter uses multiple iterations in the least-square approach, by defining the cost function

$$J(\Delta \mathbf{h}_k) = (\mathbf{n} - \mathbf{A}\mathbf{L}\Delta \mathbf{h}_k)^T \mathbf{W} (\mathbf{n} - \mathbf{A}\mathbf{L}\Delta \mathbf{h}_k) + \mu(\tilde{\mathbf{h}}_k + \Delta \mathbf{h}_k)^T \mathbf{P}_{hh} (\tilde{\mathbf{h}}_k + \Delta \mathbf{h}_k), \quad (3.5)$$

where $\tilde{\mathbf{h}}_k$ is the vector of unknown parameters at step $k - 1$, i.e., the mass anomaly per mascon in meters of EWH, k is the iteration index, $\Delta \mathbf{h}_k$ is the correction of $\tilde{\mathbf{h}}_k$, \mathbf{n} is the residual between the GRACE KBRR observations and a model prediction generated by \mathbf{h}_k , \mathbf{A} is the matrix of partial derivatives of the KBRR observations with respect to the Stokes coefficients $(\Delta \bar{C}_{lm}, \Delta \bar{S}_{lm})$ in Eq. (3.2), \mathbf{L} is the matrix of partial derivatives of the differential Stokes coefficients with respect to \mathbf{h}_k , \mathbf{W} is the data weight matrix, \mathbf{P}_{hh} is the mascon regularization matrix as defined by Eq. (3.4), and μ is the regularization factor that controls the amount of regularization.

Then the iterated mascon solution \mathbf{h}_{k+1} is given by $\mathbf{h}_{k+1} = \tilde{\mathbf{h}}_k + \Delta \mathbf{h}_k$, where

$$\Delta \mathbf{h}_k = (\mathbf{L}^T \mathbf{A}^T \mathbf{W} \mathbf{A} \mathbf{L} + \mu \mathbf{P}_{hh})^{-1} (\mathbf{L}^T \mathbf{A}^T \mathbf{W} \mathbf{n} + \mu \mathbf{P}_{hh} \tilde{\mathbf{h}}_k). \quad (3.6)$$

According to Luthcke et al. (2013), the iterated variant of the mascon approach strengthens the signal amplitude. Moreover, unlike applying a uniform statio-temporal

constraint to any mascon pair globally as in Luthcke et al. (2006a), Luthcke et al. (2013) apply anisotropic constraints by dividing the Earth's surface into seven regions: Greenland coastal area (< 2000 m elevation), Greenland inner area (> 2000 m elevation), Antarctica coastal area (< 2000 m elevation), Antarctica inner area (> 2000 m elevation), Gulf of Alaska, land and ocean.

3

The mascon approaches of Luthcke et al. (2006a), Watkins et al. (2015), Save et al. (2016) and Luthcke et al. (2013) are able to derive mass variations from GRACE data with high spatial and temporal resolutions and with less signal distortions compared to the mass anomalies represented in terms of SHCs. Direct operation on GRACE Level 1B data (i.e., K-band range-rate observations, orbit data, accelerometer data, etc.), makes these approaches very complex, and the implementation and further improvement of them is almost impossible for others (Baur and Sneeuw, 2011).

3.2.3. The mascon approach by Sasgen et al. (2010)

Sasgen et al. (2010) propose a variant of the mascon approach to estimate the mass loss trend in the Amundsen Sea sector from GRACE Level 2 data. Using time series of GRACE monthly spherical harmonic coefficients, they fit an analytic model consisting of a linear trend, a bias, and annual and semiannual components for each spherical harmonic coefficient. The fitted trend is converted into gridded geoid heights, which form the observations to estimate a model of total mass change for the Amundsen Sea section. This model consists of 8 parameters, corresponding to a subdivision of the Amundsen Sea sector into 8 drainage systems. Each parameter, e.g., m_k , represents the total mass change over the drainage system k . The distribution of the total mass change over the drainage system is given by a spatially varying function w_k , which is proportional to the observed ice flow velocities from InSAR inside the drainage system k and zero outside. If w_k is normalized to

$$\int_{\sigma_R} w_k(x) d\sigma_R = 1, \quad (3.7)$$

where x is a point on the surface of the sphere σ_R of radius R , we may expand $w(x)$ in surface spherical harmonics,

$$w(x) = \sum_{n,m} w_{nm}^{(k)} \bar{Y}_{nm}(\hat{x}), \quad (3.8)$$

where \bar{Y}_{nm} is a surface spherical harmonic of degree n and order m and $\hat{x} = \frac{x}{|x|}$ is a point on the unit sphere. Then, the geoid height signal of a unit total mass change over

the drainage system k can be written as

$$\bar{N}_k(x) = \frac{GM}{Rg_0} \sum_{n_{\min}}^{n_{\max}} \frac{4\pi R^2}{2n+1} (1 + q_n) \sum_m w_{nm}^{(k)} \bar{Y}_{nm}(\hat{x}), \quad (3.9)$$

where G is the universal gravitational constant, g_0 is a representative value of gravity at the Earth's surface (e.g., 9.81 m/s²), and $\{q_n\}$ are the elastic-compressive surface load Love numbers. Sasgen et al. (2010) suggest a value of $n_{\min} = 7$ to suppress signal leakage from outside Antarctica. n_{\max} is set equal to 55. The functional model which relates the pseudo-observations to the model parameters then follows the superposition principle,

$$N(x) = \sum_{k=1}^8 \zeta_k(x) m_k. \quad (3.10)$$

An estimate of the model parameters $\{m_k\}$ is then obtained using weighted least-squares techniques with regularization.

This variant of the mascon approach provides a reasonable estimation of the trend in mass variations in the Amundsen Sea sector at the drainage system scale. It allows for spatial variations of mass changes within each drainage system, instead of assuming a uniform mass distribution.

3.2.4. The mascon approach by Schrama and Wouters (2011)

In Schrama and Wouters (2011) and Bonin and Chambers (2013), a unit basin function is introduced for each mascon to represent the spatial pattern of the signal at the Earth's surface. Each basin function is equal to 1 inside its domain and 0 outside on a pre-defined grid which covers not only Greenland, but also the neighboring areas. Then, a spherical harmonic synthesis (complete to degree 60) is applied to each basin function separately. Due to the finite spatial resolution provided by GRACE monthly solutions, a Gaussian smoothing is applied to the converted harmonic coefficients of each mascon. Then, for each mascon, a set of smoothly varying leakage weights between 0 and 1 on the grid is produced and denoted as $w(\phi, \lambda)$. Let's denote α_j as unknown parameter to represent a uniform signal amplitude of mascon j . Then the full modelled signal h (EWH in units of metres) can be represented as a linear combination of the product of each mascon amplitude and its spatially smoothed leakage weights.

$$h(\phi, \lambda) = \sum_{j=1}^N \alpha_j w_j(\phi, \lambda), \quad (3.11)$$

where N is the number of mascons. Then, Eq. (3.11) could also be rewritten in matrix form

$$\mathbf{h} = \mathbf{S}\boldsymbol{\alpha}, \quad (3.12)$$

where \mathbf{S} is the design matrix formed by $w_j(\phi, \lambda)$ and $\boldsymbol{\alpha}$ is the vector of unknown parameters to be estimated using a least-square adjustment

$$\boldsymbol{\alpha} = (\mathbf{S}^T \mathbf{S})^{-1} \mathbf{S}^T \mathbf{h}. \quad (3.13)$$

3

To stabilize the normal matrix, Tikhonov regularisation with regularization matrix \mathbf{W}^{-1} is used, i.e., Eq. (3.13)

$$\boldsymbol{\alpha} = (\mathbf{S}^T \mathbf{S} + \mathbf{W}^{-1})^{-1} \mathbf{S}^T \mathbf{h}. \quad (3.14)$$

Similar to the variant of the mascon approach by Sasgen et al. (2010), this method also works with GRACE Level 2 data. However, Schrama and Wouters (2011) forced a uniform mass re-distribution within each mascon as was also done by Luthcke et al. (2006a).

3.2.5. The mascon approach by Baur and Sneeuw (2011)

Inspired by Forsberg and Reeh (2007), Baur and Sneeuw (2011) relate individual point mass variations at the Earth's surface to gravitational disturbances at satellite altitude (cf. Fig. 3.1). Their functional model can be written as

$$\delta g_i = G \sum_{j=1}^N \delta m_j (r_{S_i}^2 + r_{P_j}^2 - 2r_{S_i} r_{P_j} \cos \Psi_{ij})^{-\frac{3}{2}} (r_{S_i} - r_{P_j} \cos \Psi_{ij}), \quad (3.15)$$

where δg_i is the gravity disturbance at point S_i at satellite altitude (e.g., 500 km), δm_j is the mass variation at point P_j , Ψ_{ij} is the spherical distance between S_i and P_j , and r_{S_i} and r_{P_j} are the spherical radii of point S_i and P_j . The point masses are located at a mean Earth sphere of radius a .

The gravity disturbance at point S_i is synthesized from the GRACE Level 2 data as

$$\delta g = \frac{GM}{r^2} \sum_{l=1}^L \frac{l+1}{1+k'_l} \left(\frac{a}{r}\right)^l \sum_{m=0}^l \bar{P}_{lm}(\sin \phi) (\Delta C_{lm} \cos m\lambda + \Delta S_{lm} \sin m\lambda), \quad (3.16)$$

where GM is the geocentric constant. Then, the mass variations at the Earth's surface can be estimated using least-squares.

In contrast to the variant by Sasgen et al. (2010) and Schrama and Wouters (2011), the mascon approach proposed by Baur and Sneeuw (2011) links the mass variations at the Earth's surface to the gravity disturbances synthesized from GRACE level-2 data at a

mean satellite altitude. This makes the data noise less subject to artificial manipulations (such as downward continuation and low-pass filtering). However, they use ordinary least-squares, even though the noise covariance matrix of the gravity disturbances is a full matrix.

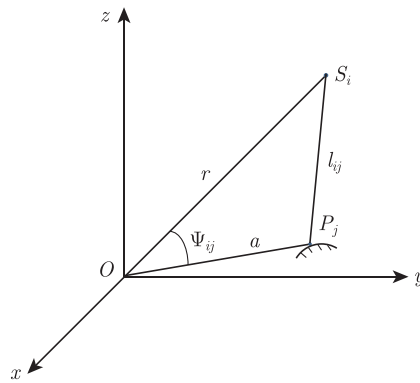


Figure 3.1 Schematic plot of the mascon approach proposed by Baur and Sneeuw (2011). P_j and S_i are used for data points at the satellite altitude and the point masses at the Earth's surface, respectively.

3.3. Summary

In this chapter, we have briefly reviewed the most important mascon approaches proposed in the literature. The approaches of Luthcke et al. (2006a), Luthcke et al. (2013), Watkins et al. (2015), and Save et al. (2016) operate directly on GRACE Level 1B data, which makes them very complex and difficult to reproduce by others. The approaches of Forsberg and Reeh (2007), Sasgen et al. (2010), Baur and Sneeuw (2011), and Schrama and Wouters (2011) use GRACE monthly spherical harmonic models as input. From these, pseudo-observations are synthesized, e.g., geoid heights (Sasgen et al., 2010), low-pass filtered EWHs (Schrama and Wouters, 2011), and gravity disturbances at mean satellite altitude (Forsberg and Reeh, 2007; Baur and Sneeuw, 2011). These approaches are much simpler to implement.

The mascon variant of Forsberg and Reeh (2007) is chosen as the basis for further developments in the framework of this book (cf. Chapter 4). We consider this variant to be more natural, as the synthesized data in this case better resemble the original satellite observations, without the need to apply a low-pass filter as in Schrama and Wouters (2011).

4

Statistically optimal estimation of Greenland Ice Sheet mass variations from GRACE monthly solutions using an improved mascon approach

4.1. Introduction

One of the primary sources of information on mass variations of the Greenland Ice Sheet (GrIS) is the Gravity Recovery and Climate Experiment (GRACE) satellite mission. Primarily using K-band ranging (KBR) data between the two GRACE satellites, monthly sets of spherical harmonic coefficients (SHCs) are computed complete to some maximum degree, e.g., 96 for CSR (the Center of Space Research of the University of Texas at Austin) RL05 solutions (Bettadpur, 2012) and 90 for GFZ (GeoForschungsZentrum) RL05 solutions (Dahle et al., 2012). Alternatively, gravity solutions in terms of mass anomalies per mass concentration block (“mascon”) have also been released by Jet Propulsion Laboratory (JPL) (Watkins et al., 2015; Wiese, 2016; Wiese et al., 2016), Goddard Space Flight Center (GSFC) (Luthcke et al., 2013) and CSR (Save et al., 2016). To clean the KBR data from the contribution of high-frequency mass variations, an ocean tide model (e.g., EOT11a (Savcenko and Bosch, 2010)), a model of the non-tidal components of the atmospheric and oceanic mass variations (e.g., the Atmosphere and Ocean De-aliasing model (AOD) (Dobslaw et al., 2013)), and other background models are routinely used.

The sensitivity of GRACE measurements is known to be anisotropic: it is higher in the along-track direction and lower in the cross-track direction (Condi et al., 2004; Ditmar et al., 2012). A higher sensitivity amplifies data errors, caused by, among other things, noise in the data provided by the on-board sensors and imperfection in the background models. As a result, monthly sets of SHCs are contaminated by strong north-south “stripes”, with amplitudes that depend on the latitude (Wahr et al., 2006).

These amplitudes are smaller in polar areas and larger near the equator (Wahr et al., 2006; De Linage et al., 2009).

In principle, gravity field variations expressed in spherical harmonics can be converted into mass anomalies at the Earth's surface by a spectral transfer using an appropriate scaling of the SHCs (Wahr et al., 1998). To suppress stripes and high-frequency noise, low-pass filters and/or de-striping schemes are typically used (Jekeli, 1981; Wahr et al., 1998; Swenson and Wahr, 2006), at the cost of a reduced spatial resolution and distortions in the estimated mass anomalies (Duan et al., 2009).

4

Alternatively, the mass anomalies can be estimated from the SHCs using least-squares techniques. In this case, they are modelled as a thin mass layer located at the Earth's surface, or an approximation to it. The mass layer is introduced as a constant function over mascons of predefined geometries. The geometry of the mascons can be chosen to take into account of existing physical constraints, such as the geometry of the coastline. A proper choice of the mascons size allows for noise suppression without the need for any additional filtering of the SHCs, e.g., a destriping scheme.

This helps to reduce distortions in the estimated mass anomalies. Luthcke et al. (2006a) was the first to use the mascon representation to derive mass anomalies over Greenland from GRACE Level-1b data, followed by Luthcke et al. (2013), Watkins et al. (2015) and Save et al. (2016). To reduce the numerical complexity, variants of the mascon approach using monthly sets of SHCs as input have been proposed, e.g., Forsberg and Reeh (2006); Baur and Sneeuw (2011); Schrama and Wouters (2011). Following Forsberg and Reeh (2006); Baur and Sneeuw (2011), we compute monthly sets of gravity disturbances at an average satellite altitude from the monthly sets of SHCs as data to estimate mass anomalies per mascon.

The major objective of the present study is to develop a statistically optimal variant of the mascon approach applicable to the estimation of Greenland mass anomalies. We propose a number of improvements upon Forsberg and Reeh (2006) and Baur and Sneeuw (2011). Two of the major improvements are described here. Firstly, we properly propagate the full error covariance matrices of the monthly SHCs into gravity disturbances at satellite altitude using the law of covariance propagation. These noise covariance matrices of the gravity disturbances are used in the subsequent least-squares adjustment. We expect a noticeable improvement of the estimated mass anomalies and their uncertainties, as the noise in the SHCs is highly correlated (Swenson and Wahr, 2006), among others due to the anisotropic sensitivity of the GRACE KBR data. To

address the ill-conditioning of the propagated noise covariance matrices, we develop an approximate inversion scheme based on an eigenvalue decomposition. Secondly, we ensure a spectral consistency between the GRACE-based gravity disturbances and the unknown mascon parameters. The spectrum of the GRACE-based gravity disturbances is limited by the maximum spherical harmonic degree of the monthly sets of SHCs, while the mascon representation implies that gravity disturbances also contain energy at higher frequencies. The spectral consistency has not been considered in previous studies, in part because these studies used scaled unit matrices to represent the data noise. When full noise covariance matrices are used as in this book, spectral consistency between model and data noise is essential to obtain high-quality solutions.

Typically, the mascon approach uses regularization or other spatial constraints to suppress noise at the cost of introducing a bias in the solution. In this book, no spatial constraints in the form of regularization are used. Instead, the size of the mascons is carefully chosen to control the noise.

To demonstrate the performance of the proposed methodology, we use both synthetic and real data. In the latter case, we use GRACE Release-05 monthly solutions provided by CSR. To investigate the importance of proper data weighting and for validation, we compare the estimated mass anomalies with Surface Mass Balance (SMB) estimates from the Regional Atmospheric Climate Model (RACMO 2.3) (Noël et al., 2015). However, a direct comparison of GRACE-based and SMB-based mass anomalies is not possible because the latter time-series lacks the ice discharge signal. To overcome this problem, we estimate and remove linear trends from both time-series. This is justified because the seasonal mass variation signals of Greenland are dominated by SMB-related signals (Van den Broeke et al., 2009).

The improved mascon approach put forward by Ran et al. (2018a) is summarized in this chapter, the rest of which is organized as follows. In Sect. 4.2, we present the statistically optimal mascon approach. The performance of this approach is demonstrated on simulated data, which is the subject of Sect. 4.3. In particular, we investigate the extent to which the estimates are improved by incorporating the full noise covariance matrices and by ensuring the spectral consistency between the data and the mascon parameters. In Sect. 4.4, we present the results of real data processing and validate them against SMB time-series. Finally, we provide a summary and the main conclusions in Sect. 4.5.

4.2. Methodology

We propose an improved mascon approach compared to previous studies by Forsberg and Reeh (2007) and Baur and Sneeuw (2011). Sect. 4.2.1 describes the functional model used, which is forced to be spectrally consistent with the monthly GRACE SHCs. In Sect. 4.2.2, we discuss a practical way to divide the territory of Greenland into nearly equal-area patches of irregular shape. The proper choice of the area over which gravity disturbances are generated at satellite altitude is discussed in Sect. 4.2.3. Sect. 4.2.4 describes the statistically-optimal inversion of the gravity disturbances into mass anomalies per mascon.

4

4.2.1. Gravity disturbances

Monthly sets of gravity disturbances at mean satellite altitude are computed from monthly GRACE SHCs using spherical harmonic synthesis. They are then related to the gravitational attraction of mascons at the Earth's surface. Finally, mascon parameters are estimated using least-squares techniques.

GRACE-based gravity disturbances

In the context of this study, a gravity disturbance g is understood to be the negative radial derivative of the gravitational potential V , generated by a mass anomaly:

$$\delta g = -\frac{\partial V}{\partial r}. \quad (4.1)$$

They are linked to a set of GRACE SHCs ΔC_{lm} and ΔS_{lm} complete to degree L as

$$\delta g_p = \frac{GM}{r_p^2} \sum_{l=1}^L \frac{l+1}{1+k'_l} \left(\frac{a}{r_p} \right)^l \sum_{m=0}^l \bar{P}_{lm} (\sin \phi_p) (\Delta C_{lm} \cos m\lambda_p + \Delta S_{lm} \sin m\lambda_p), \quad (4.2)$$

where GM is the geocentric constant; a is the semi-major axis of the reference ellipsoid; (r_p, ϕ_p, λ_p) are spherical coordinates of a data point p , assumed in this book is to be located at an altitude of 500 km above a mean Earth sphere; L is the maximum degree of the monthly GRACE solutions; and \bar{P}_{lm} is the normalized associated Legendre function of degree l and order m . Note that the expression includes the load Love numbers k'_l , which are introduced to account for the effect of the elastic response of the Earth to a load, which is included in the SHCs. The lateral distribution of the data points is discussed in Sect. 4.2.3.

Gravity disturbances generated by a set of mascons

Suppose we have N mascons M_i ($i = 1, 2, \dots, N$). The surface density (mass per unit area) of mascon i is denoted as ρ_i . Then, Eq. (4.1) can be re-written as

$$\delta g_p = -\frac{\partial}{\partial r} \left(G \sum_{i=1}^N \rho_i \int_{M_i} \frac{ds}{l_p} \right) = -\frac{\partial}{\partial r} \left(G \sum_{i=1}^N \rho_i I_{i,p} \right), \quad (4.3)$$

where G is the universal gravitational constant, and

$$I_{i,p} = \int_{M_i} \frac{ds}{l_p} \quad (4.4)$$

with l_p being the distance between an integration point and the data point p .

$I_{i,p}$ has to be computed using numerical integration. Here, we use a composed Newton-Cotes formula. The nodes are located on a Fibonacci grid (González, 2010). The number of nodes of mascon i is denoted K_i . Then,

$$I_{i,p} \approx \sum_{j=1}^{K_i} w_{ij} \frac{1}{l_{ij,p}}, \quad (4.5)$$

where $w_{ij} = S_i / K_i$ with S_i as the surface area of mascon i . The distance $l_{ij,p}$ between a Fibonacci point with spherical coordinates $(r_{ij}, \phi_{ij}, \lambda_{ij})$ and the data point p with spherical coordinates (r_p, ϕ_p, λ_p) can be computed as

$$l_{ij,p} = (r_{ij}^2 + r_p^2 - 2r_{ij}r_p \cos \Psi_{ij,p})^{\frac{1}{2}}, \quad (4.6)$$

where $\cos \Psi_{ij,p} = \sin \phi_p \sin \phi_{ij} + \cos \phi_p \cos \phi_{ij} \cos(\lambda_p - \lambda_{ij})$.

Then,

$$\delta g_p \approx G \sum_{i=1}^N \rho_i \sum_{j=1}^{K_i} w_{ij} (r_{ij}^2 + r_p^2 - 2r_{ij}r_p \cos \Psi_{ij,p})^{-\frac{3}{2}} (r_{ij} - r_p \cos \Psi_{ij,p}). \quad (4.7)$$

Eq. (4.7) represents the functional model that relates the gravity disturbances and the surface densities of the mascons. In matrix-vector form, Eq. (4.7) can be written as

$$\mathbf{d} \approx \mathbf{A}' \mathbf{x}, \quad (4.8)$$

where \mathbf{x} is the vector of surface densities, \mathbf{d} is the vector of gravity disturbances, and \mathbf{A}' is the design matrix. The vector \mathbf{x} is estimated from the vector of gravity disturbances \mathbf{d}

using weighted least-squares techniques.

The gravity disturbances of Eq. (4.2) have a limited bandwidth because the monthly GRACE solutions are limited to a certain maximum spherical harmonic degree. However, the gravity disturbances of Eq. (4.7) are not band-limited. Hence, the functional model, Eq. (4.8) is, not correct as there is a spectral inconsistency between the data and the model. To obtain a spectrally consistent functional model, we need to apply a lowpass filter to the design matrix \mathbf{A}' , i.e., \mathbf{A}' needs to be replaced by \mathbf{A} , where

$$\mathbf{A} = \mathbf{Y} \mathbf{A}', \quad (4.9)$$

and \mathbf{Y} represents the lowpass filter. Without such a lowpass filter, the short-wavelengths of the estimated mascon solution would be biased towards zero.

4

To define an appropriate lowpass filter, we must remember that each column of the design matrix \mathbf{A}' represents a set of gravity disturbances caused by a single mascon of unit surface density. Therefore, the filter operation can be implemented as follows. Firstly, gravity disturbances caused by a single mascon of unit surface density are computed on an equal-angle global grid. They are used as input to estimate an SH model of the gravity disturbances, complete to some maximum degree $L > L_G$, using spherical harmonic analysis. The SH model is truncated at the maximum degree L_G of the monthly GRACE spherical harmonic models, and successively used to synthesise a column of the design matrix \mathbf{A} corresponding to the single mascon. This procedure must be repeated for every mascon. The result is a design matrix \mathbf{A} that is spectrally consistent with the information content in the data and the data noise covariance matrix.

The spectrally consistent analog of Eq. (4.8) is written as

$$\mathbf{d} = \mathbf{Ax} + \mathbf{n}, \quad (4.10)$$

where the vector \mathbf{n} is introduced to account for noise in the GRACE-based gravity disturbances. This noise is assumed to be zero-mean and Gaussian. Furthermore, we assume that

$$D\{\mathbf{n}\} = \mathbf{C}_d, \quad (4.11)$$

where $D\{\mathbf{n}\}$ is the dispersion operator, and \mathbf{C}_d is the data noise covariance matrix. The latter is computed on a month-by-month basis from the full noise covariance matrix of the monthly SHCs using the law of covariance propagation.

Then, best-linear unbiased estimate (BLUE) of the mass anomalies is

$$\hat{\mathbf{x}} = (\mathbf{A}^T \mathbf{C}_d^{-1} \mathbf{A})^{-1} \mathbf{A}^T \mathbf{C}_d^{-1} \mathbf{d}. \quad (4.12)$$

The BLUE, Eq. (4.12), is referred to as the “statistically optimal estimator” in this book.

4.2.2. Parameterization

The correct choice of the mascon size is important to mitigate noise amplification during the data inversion. To facilitate experiments with different mascon sizes, we developed a procedure to automatically divide the territory of Greenland into nearly equal-area mascons of a desired size. The procedure consists of two steps. In the first step, Greenland is divided into latitudinal strips of equal width, chosen to be as close as possible to the desired size. In the second step, each strip is divided into individual mascons of an approximately desired size using straight segments in the rectangular projection. The orientation of the segments is adjusted to follow the orientation of the western and eastern borders of the current strip. Examples of the resulting parameterizations are shown in Fig. 4.1. Note that the mascons located on the Greenland coast are defined according to the coastal geometry.

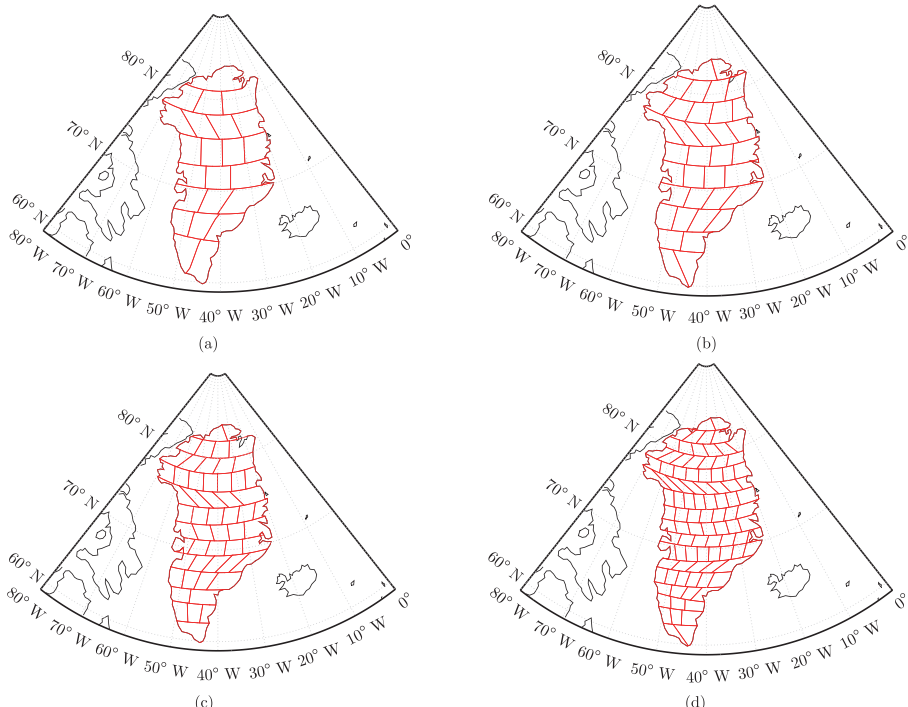


Figure 4.1 Partitioning of Greenland into 23 (size about $300 \text{ km} \times 300 \text{ km}$), 36 (size about $250 \text{ km} \times 250 \text{ km}$), 54 (size about $200 \text{ km} \times 200 \text{ km}$), and 95 (size about $150 \text{ km} \times 150 \text{ km}$) mascons, respectively.

We also define 9 mascons outside Greenland to reduce signal leakage from outside

Greenland into the Greenland mascons. These mascons cover Iceland, Svalbard, and the glaciers of the Canada's Arctic Archipelago, see Fig. 4.2. It is worth noting that we do not parameterize the nearby ocean areas, as the impact of the oceanic mascons is small, e.g., at the level of 7 Gt/yr for the trend over 2003–2013, when the optimal data weighting is applied.

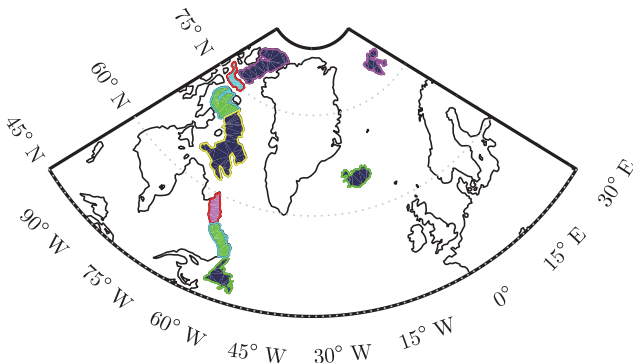


Figure 4.2 Mascons outside Greenland used in this book.

4.2.3. Distribution of data points

We followed the suggestion of Baur and Sneeuw (2011) for the altitude of the date grid: 500 km. Another option is to use altitudes between 480–500 km to account for the decrease in orbital altitude of the GRACE satellites, as was done by Forsberg et al. (2017). Numerical studies (not shown here) reveal that this leads to similar estimates (around 10 Gt/yr in terms of the trend over 2003–2013) when the data weighting is switched on. We attribute the observed minor differences to the fact that the applied data processing strategy, including the truncation of the matrix C_d spectrum, was fine-tuned for the grid altitude of 500 km. We expect that fine-tuning of the data processing for grid altitudes chosen to be consistent with actual GRACE orbits would further reduce these differences. This was beyond the scope of this study, but may be the subject of future research. The data area comprises Greenland and a buffer zone of 800 km around Greenland. The use of a buffer zone is justified by the fact that each gravity disturbance at satellite altitude is sensitive to a mass re-distribution in a neighbourhood of a few hundred kilometres around that point (Baur and Sneeuw, 2011). Thus, defining the data area in this way ensures a more comprehensive representation of the target signals. The data points are located on a Fibonacci grid with an average distance of 37.5 km. Additional data points on the oceans, but outside the data area are introduced for reasons discussed in Sect. 4.3.2. They are located on a Fibonacci grid with a mean

distance of 2000 km. The total number of data points is 6953 with 6867 points inside the data area and 86 points in ocean areas outside the data area.

4.2.4. Data inversion

The full noise covariance matrix of the GRACE-based gravity disturbances, \mathbf{C}_d , is ill-conditioned and has a gradually decreasing eigenvalue spectrum with many eigenvalues close to zero. Therefore, some kind of regularization is needed before this matrix is inverted. Here, we use an eigendecomposition to compute an approximate inverse, i.e.,

$$\mathbf{C}_d = \mathbf{Q} \Lambda \mathbf{Q}^T, \quad (4.13)$$

where \mathbf{Q} is a unitary matrix which contains the eigenvectors of \mathbf{C}_d and Λ is the square diagonal matrix of eigenvalues of \mathbf{C}_d . In Appendix A, we show that the matrices \mathbf{Q} and Λ can be computed without explicitly computing matrix \mathbf{C}_d , which helps to minimize the loss of significant digits.

Formally, the inversion of the matrix \mathbf{C}_d can be written as

$$\mathbf{C}_d^{-1} = (\mathbf{Q} \Lambda \mathbf{Q}^T)^{-1} = \mathbf{Q} \Lambda^{-1} \mathbf{Q}^T. \quad (4.14)$$

However, many eigenvalues of the matrix \mathbf{C}_d are small, reflecting the ill-conditioning of this matrix. Therefore, an approximate inverse of this matrix is computed as follows. The matrix Λ is truncated in such a way that only the eigenvalues exceeding a pre-defined threshold are retained:

$$\Lambda_t = \mathbf{J} \Lambda \mathbf{J}^T, \quad (4.15)$$

where $\mathbf{J} = [\mathbf{I} \ \mathbf{0}]$ is the truncation operator with \mathbf{I} being a unit matrix and Λ_t is the resulting diagonal matrix, containing a truncated set of eigenvalues. By retaining only sufficiently large eigenvalues, we stabilize the computation of the inverse of the matrix Λ_t . An approximate inverse $\tilde{\Lambda}^{-1}$ of the original matrix Λ is obtained by replacing the missing elements with zeros:

$$\tilde{\Lambda}^{-1} = \mathbf{J}^T \Lambda_t^{-1} \mathbf{J}. \quad (4.16)$$

After that, we define the approximate inverse $\tilde{\mathbf{C}}_d^{-1}$ of the matrix \mathbf{C}_d as

$$\tilde{\mathbf{C}}_d^{-1} = \mathbf{Q} \tilde{\Lambda}^{-1} \mathbf{Q}^T = \mathbf{Q} \mathbf{J}^T \tilde{\Lambda}_t^{-1} \mathbf{J} \mathbf{Q}^T = \mathbf{Q}_t \tilde{\Lambda}_t^{-1} \mathbf{Q}_t^T, \quad (4.17)$$

where

$$\mathbf{Q}_t = \mathbf{Q} \mathbf{J}^T \quad (4.18)$$

is the truncated matrix \mathbf{Q} containing only the eigenvectors related to the retained eigenvalues. Then, according to Eq. (4.12), the weighted least-squares solution $\hat{\mathbf{x}}$ is

$$\begin{aligned}\hat{\mathbf{x}} &= (\mathbf{A}^T \tilde{\mathbf{C}}_d^{-1} \mathbf{A})^{-1} \mathbf{A}^T \tilde{\mathbf{C}}_d^{-1} \mathbf{d} \\ &= (\mathbf{A}^T \mathbf{Q}_t \tilde{\Lambda}_t^{-1} \mathbf{Q}_t^T \mathbf{A})^{-1} \mathbf{A}^T \mathbf{Q}_t \tilde{\Lambda}_t^{-1} \mathbf{Q}_t^T \mathbf{d} \\ &= (\mathbf{B}^T \tilde{\Lambda}_t^{-1} \mathbf{B})^{-1} \mathbf{B}^T \tilde{\Lambda}_t^{-1} \mathbf{Q}_t^T \mathbf{d},\end{aligned}\quad (4.19)$$

where

$$\mathbf{B} = \mathbf{Q}_t^T \mathbf{A}. \quad (4.20)$$

This solution is still unbiased, but strictly speaking it is not a minimum dispersion solution.

4

4.3. Numerical experiments

We perform a series of numerical experiments to evaluate the performance of the improved mascon approach and to fine-tune some data processing parameters. In Sect. 4.3.1, we present the basic setup of the numerical experiments. Sect. 4.3.2 is devoted to the presentation and discussion of the results. The importance of the spectral consistency is discussed in Sect. 4.3.3.

4.3.1. Experimental setup

The basic setup used in all numerical experiments includes the definition of i) the “true” signal and ii) the error sources.

“True” signal

We define the “true” signal as the annual mass change, which is determined on the basis of trends extracted from ICESat altimetry data (see Table 4.1)(Felikson et al., 2017). As shown in Fig. 4.3, these trends represent the mean rate of mass change over the period 2003–2009 per 20 km × 20 km patch covering entire Greenland, converted from the surface elevation change rate by applying a density of 917 kg/m³ (Wahr et al., 2000). This signal is used directly to calculate the mass anomaly per mascon as “truth”. Using the proposed mascon approach, we generate gravity disturbances at satellite altitude from the ICESat altimetry data. We then lowpass-filter them to limit the spectrum to spherical harmonic degrees from 1 to 120. Finally, we estimate the mass anomaly per mascon and compare it with the “truth” to evaluate the performance of the method.

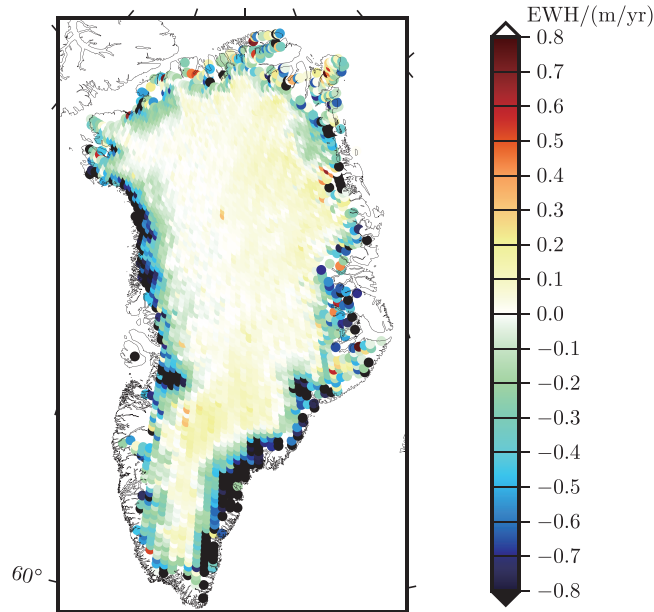


Figure 4.3 The “true” signal defined as the yearly mass change over the GrIS, in terms of EWH in units of metres.

Table 4.1 A summary of the data used in this book

Data	Role	Temporal resolution	Spatial resolution	Pre-Processing
ICESat elevation change rate	Simulating the true signal	2003-2009	20 km blocks	—
GRACE SHCs from DMT	Simulating signal leakage	Month	Degree 120	—
GRACE SHCs from CSR RL05	Real data	Month	Degree 96	—
Surface mass balance from RACMO2.3	Validating estimates	Daily	11 km blocks	Resampled to monthly mean SMB for each drainage system and entire Greenland

There is much freedom in defining the “true” signal in the presence of secular trends. The “true” signal can reflect the total mass change over an arbitrary time interval, ranging from one month to many years. The choice of the time interval determines the contribution of error sources like signal leakage and parameterization errors to the overall error budget. If the time interval is short (e.g., one month), signal leakage and parameterization errors may be small compared to the data noise. However, the relative contribution of these error sources to the overall error budget increases with increasing

time interval. In this book, we define the “true” signal as the yearly mass change, which represents a kind of intermediate choice between the two extremes of a monthly signal and a multi-year signal. Our time interval is slightly shorter than that used in the study by Bonin and Chambers (2013), which was 4 years. In any case, the amplitude of the true signal in real GRACE data processing may differ depending on the signal of interest, which can range from short-term mass variations to long-term trends.

Error sources

The data generated in the previous section are superimposed by errors. In this book, we consider 4 error sources, i.e., signal leakage, AOD noise, random noise in GRACE-based SHCs, and parameterization error. The latter is also sometimes referred to as the “model error” (e.g., Xu, 2010; Stedinger and Tasker, 1986)

4

Signal leakage. In this book, signal leakage refers to the impact of mass variations from outside Greenland on the estimated mascons. To simulate signal leakage, we introduce mass variations in Alaska, northern Canada, northern Russia, and Fennoscandia, see Fig. 4.4. The “true” signal over these areas is also defined as the yearly mass variation. It is generated using the available optimally filtered trend over 2003–2008 based on the Delft Mass Transport model (DMT) (Siemes et al., 2013).

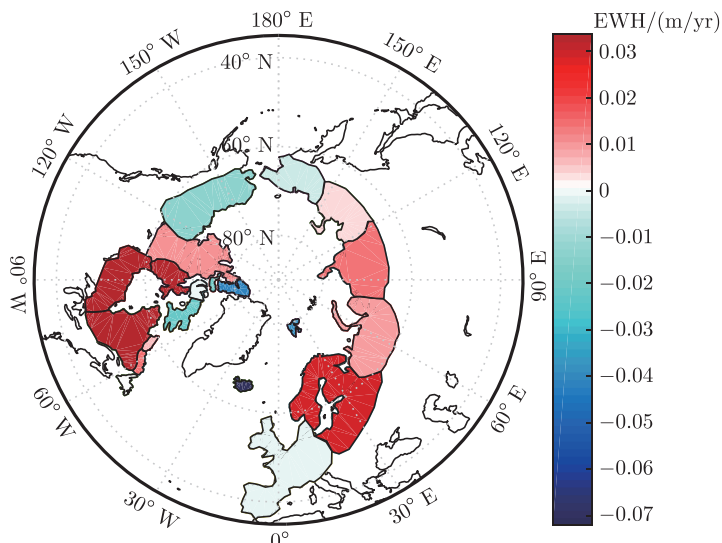


Figure 4.4 Mascons used to simulate signal leakage. The value of each mascon is the full signal generated using the trend over the period 2003–2008 derived from the DMT model, in terms of EWH in units of metres.

AOD noise. AOD noise refers to errors in the background models, which are used to reduce non-tidal mass transport in the atmosphere and ocean. AOD error is considered to be one of the major error sources in the monthly solutions. Here, we also take 10% of the difference of two AOD models (see Fig. 4.5) separated by one year as the AOD noise, according to the definition of the true signal (yearly mass accumulation). For this purpose, we choose AOD models in August of 2005 and 2006, because this period

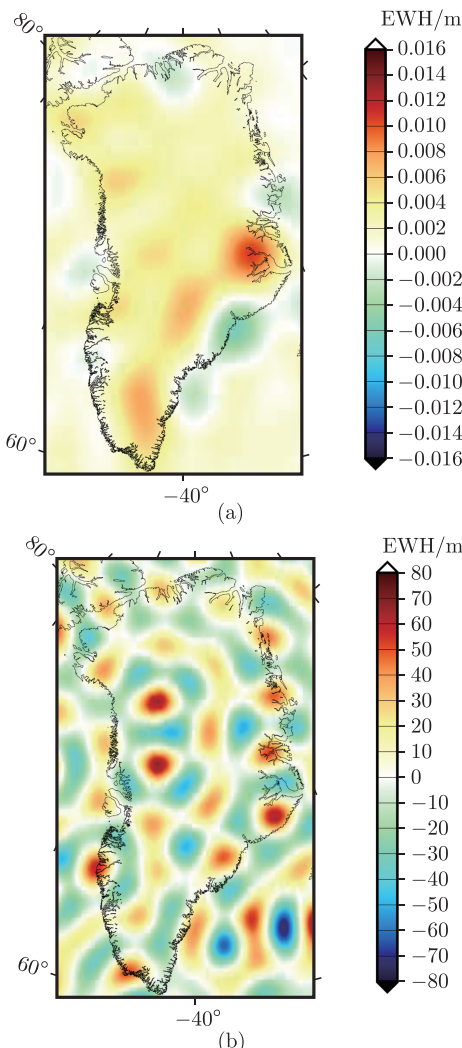


Figure 4.5 The top panel shows the AOD error taken on August 10, 2005 and August 2006. The bottom panel is a realization of simulated random errors based on the DMT noise covariance matrix of spherical harmonic coefficients for August 2006 (the matrix is complete up to degree 120). The units are metres of EWH.

is roughly in the middle of the true signal (ICESat trend over 2003–2009). Based on our numerical study, we find that the AOD noise plays a minor role. Therefore there would be negligible impact if a different time interval were chosen. Defining the AOD error as 10% of the AOD model signal is considered a reasonable choice in light of previous studies (Thompson et al., 2004; Ditmar et al., 2012).

Random noise. We assume that the yearly mass change is the result of the difference between two monthly solutions separated by a time interval of one year. Furthermore, we assume that there is no noise correlation between the monthly solutions. This implies that the random noise in the generated yearly mass change can be set equal to the noise in a monthly solution multiplied by a factor of $\sqrt{2}$. First, we generate a vector \mathbf{n} of zero-mean white Gaussian noise with unit variance; the length of \mathbf{n} is equal to the number of SHCs. Then, a realization of correlated noise with the covariance structure of the matrix \mathbf{C}_{δ_p} is obtained as

$$\mathbf{n}_c = \mathbf{L}\mathbf{n}, \quad (4.21)$$

where \mathbf{L} is the lower triangular Cholesky factor of the noise covariance matrix \mathbf{C}_{δ_p} of GRACE monthly SHCs:

$$\mathbf{C}_{\delta_p} = \mathbf{L}\mathbf{L}^T. \quad (4.22)$$

In this book, the noise covariance matrix is complete up to degree 120. It describes the noise in the GRACE SHCs in August 2006 and was produced together with the DMT model. Note that the noise in the degree-one coefficients is not included. One hundred random noise realizations are simulated in this way in order to make the results of the numerical study more representative. Fig. 4.5 shows one of these noise realizations in terms of EWHs (Equivalent Water Height).

Parameterization errors. Parameterization errors are caused by the fact that the adopted parameterization assumes a uniform surface density distribution within each mascon, while the actual distribution within a mascon may vary spatially. Here, parameterization errors are automatically introduced, as the “true” signals are generated with ICESat altimetry data with a spatial resolution of 20 km, which is much finer than the average size of a mascon.

4.3.2. Choice of the optimal data processing strategy

There are a number of choices to be made when using the improved mascon approach:

- the size of the buffer zone around Greenland;

- the number of additional data points in the oceans outside the data area;
- the number of mascons covering all of Greenland;
- the choice of the least-squares estimator (i.e., ordinary least-squares versus weighted least-squares);
- the number of eigenvalues to be retained when computing an approximate inverse of the noise variance-covariance matrix C_d .

In a series of numerical experiments, we have examined various choices. For each choice, 100 solutions were computed each with a different random noise realization. Other error sources were kept the same in all experiments. Each solution was converted to mass anomalies per mascon (in Gt), and then summed up over all the “Greenland” mascons to yield the total mass anomalies over entire Greenland. The total mass anomalies are then compared to the “true” ones; the RMS difference between the estimated and true total mass anomalies is used as a measure of the quality of the solution.

In this way, we found the optimal choice of the various parameters mentioned above, which is shown in Table 4.2. In the next sections, we show how the inversion results will deteriorate when a suboptimal choice is made. In each test, only one parameter is changed. Regarding the data weighting, we always compute two solutions; a weighted least-squares solution (weight matrix is the inverse of the full noise covariance matrix), and an ordinary least-squares solution (weight matrix is the unit matrix).

Table 4.2 Optimal set of parameters for the estimation of total mass variations of entire Greenland

Options	Optimal choice
Width of the buffer zone around Greenland	800 km
Using additional data points over the global oceans	Yes
Number of mascons within Greenland	23
Optimal data weighting applied	Yes
Number of eigenvalues retained in the approximate inversion of C_d	600
Spectral consistency maintained	Yes

Width of the buffer zone around Greenland

It is well-known that a buffer zone beyond the area of interest is necessary (Baur, 2013). In this book, the extension is referred to as the buffer zone. To investigate the impact of the choice of the buffer zone on the estimated mass anomalies over all of Greenland, we consider buffer zones varying from 100 km to 1,400 km (cf. Fig. 4.6). For each choice of the buffer zone a weighted least-squares solution and an ordinary least-squares solution

are computed. The other parameters are set equal to the values given in Table 4.2. The resulting RMS error of the recovered Greenland mass anomalies is shown in Fig. 4.7. Using a weighted least-squares estimator, the RMS error is minimal for a 800 km buffer zone, while other choices increase the RMS error by only a few Gt. This suggests that, the solution is quite robust against the choice of the buffer zone, provided that the correct data weighting is used. The situation is different when an ordinary least-squares estimator is used. The smallest RMS errors are obtained for buffer zones larger than 600 km with little variations. For smaller buffer zones, however, the RMS errors increase rapidly and reach values which are several tens of Gts higher than the minimum. Overall, the RMS error of a weighted least-squares solution is always smaller than the RMS error of an ordinary least-squares solution.

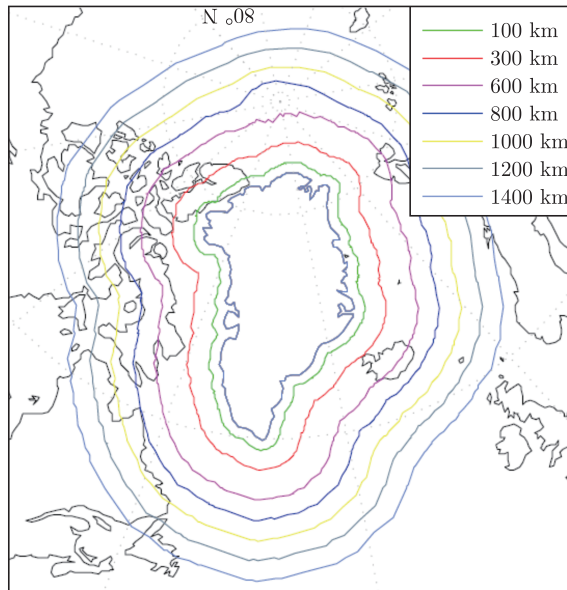


Figure 4.6 Buffer zones around Greenland considered in this book.

Using data points distributed over the oceans globally

GRACE-based SHCs at very low degrees (especially degree 2) are relatively inaccurate. In principle, the implemented data weighting should suppress the noise arising from these low-degree coefficients (Chen et al., 2005). However, in regional studies such as the one considered here, the contribution of different low-degree SHCs cannot be separated. Therefore, any attempt to suppress the noise in the very low-degree SHCs may lead to a bias in the estimated mass anomalies over all of Greenland. For example, eliminating the C_{20} may reduce the estimated trend of GrIS mass variation over 2003–2013 by ~18 Gt. To

avoid such a bias, we add additional data points. To avoid capturing the signal below them, they are confined to the oceans assuming that mass variations over the oceans are negligible. Figure 4.8 shows the geographic location of these additional data points.

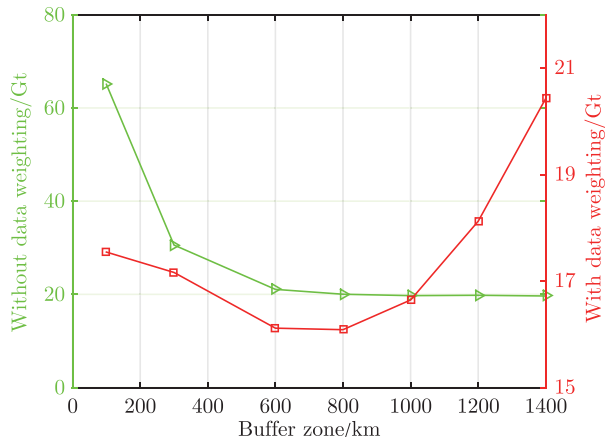


Figure 4.7 The RMS error of estimated mass anomalies as function of the buffer zone size. Red: with data weighting, green: without data weighting. Different vertical scales are used to plot the red and green curves.

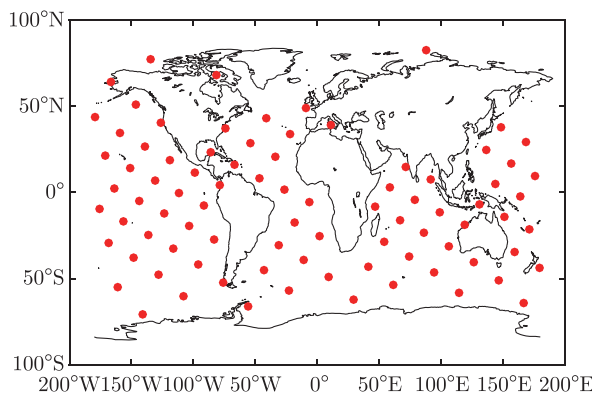


Figure 4.8 Location of additional data points over the oceans. The mean distance is about 2,000 km.

The additional data points are located on a Fibonacci grid with an average distance of about 2,000 km. Solutions are computed with and without the additional data points. A comparison of these solutions shows that the added value of using additional data points is 0.02% when using ordinary least-squares and 0.5% when using weighted least-squares. Although the improvement is small, we recommend adding additional data

points in regional studies. The numerical complexity does not change much because the total number of additional points is very limited.

Optimal number of mascons over Greenland

In this test, we divide Greenland into mascons of different sizes: from approximately $300 \text{ km} \times 300 \text{ km}$ to approximately $150 \text{ km} \times 150 \text{ km}$, corresponding to a number of mascons ranging from 23 to 95 (see Fig. 4.1). In addition, we also consider the division of Greenland into 6 or 12 mascons, as proposed in (Luthcke et al., 2006a) (Fig. 4.9). The RMS differences between the recovered and true mass anomaly estimates as a function of the number of mascons over the whole of Greenland, in are shown Fig. 4.10. We observe a significant reduction in the RMS error when a weighted least-squares estimator is used, ranging from 19% to 65%, depending on the size of the mascons.

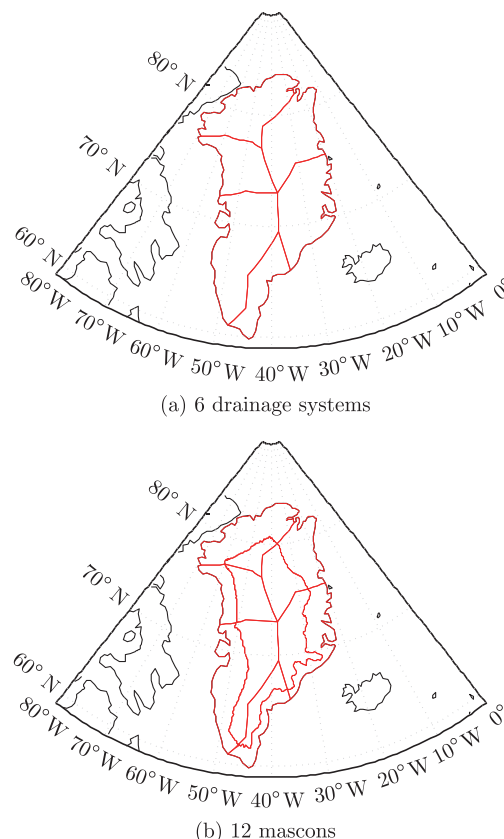


Figure 4.9 Partitioning of Greenland into 6 and 12 mascons, respectively, in line with Luthcke et al. (2006a).

From the green curve in Fig. 4.10, obtained without optimal data weighting, we can see that the RMS error when using 6 mascons is larger than the RMS error when using 23 mascons. Note that the numerical study showed in Fig. 4.10 considered all types of noise, including random noise, representation error, etc. It is also worth noting that when using weighted least-squares, the quality of the results based on 6 drainage systems is slightly higher than that based on 23 mascons (see the red curve in Fig. 4.10). This is caused by the fact that the random noise is reduced in the case of 6 mascons (i.e., from 15 to 9 Gt) compared to 23 mascons. The numbers of 15 and 9 Gt are the result of additional numerical studies where random noise was the only error source (not shown here). As the difference of the RMS values in the cases of 6 and 23 mascons (see the red curve in Fig. 4.10) is rather small and 23 mascons provide a much better spatial resolution than 6 mascons, we recommend using 23 mascons.

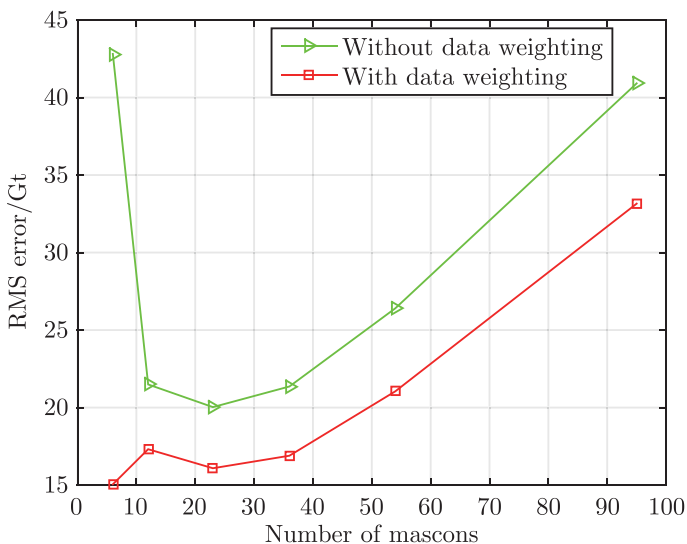
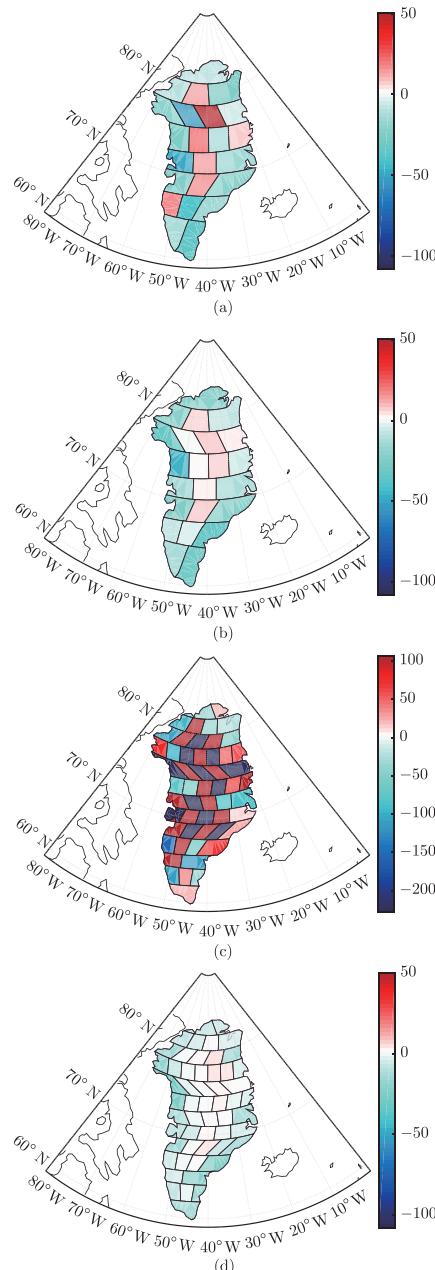


Figure 4.10 RMS errors in estimated mass anomalies over the Greenland as a function of the number of mascons.

The estimated mass anomalies for 23 mascons are shown in Fig. 4.11(a); they are estimated from the data contaminated by the errors shown in Figs. 4.4–4.5. We find that the recovered mass anomalies generally show some agreement with the true signal. For instance, the mass losses take place in the coastal region, and are mainly located in the northwest and southeast of Greenland. However, we could also see that the recovered mass per mascon does not exactly represent the spatial pattern of the signal. This



4

Figure 4.11 (a) The spatial pattern of recovered mass anomaly per mascon. They are estimated from the data that were contaminated by the errors presented in Figs. 4.4–4.5 (G_t). (b) For a better visual comparison, the true signal defined in Fig. 4.3 is spatially resampled to 23 mascons and shown in the unit of G_t . Similar to (a) and (b), (c) and (d) are for 54 mascons.

finding is consistent with Baur (2013) and Bonin and Chambers (2013). For instance, the recovered spatial pattern in the inner part of Greenland deviates significantly from the true signal. The recovered solution is much worse when too many (i.e., 54) mascons are used as shown in Fig. 4.11. Due to the small size of the mascons (about $150 \text{ km} \times 150 \text{ km}$), the recovered mean mass anomalies are quite unstable, with many positive and negative estimates next to each other.

Number of eigenvalues retained in the approximate inversion of the noise covariance matrix

The high condition number of the noise covariance matrix does not allow a stable computation of the weight matrix, and some regularization is necessary. In this book, we use a truncated eigenvalue decomposition to improve the condition number prior to inversion (cf. Sect. 4.2.4). To estimate the optimal number of eigenvalues to retain, we consider values between 200 and 1,600. The dimension of the noise covariance matrix is in our case $6,953 \times 6,953$.

The RMS error of the estimated mass anomalies over the Greenland is relatively large when only 200 eigenvalues are retained, but decreases by 49%, as the number of retained eigenvalues increases to 600 (see the red curve in Fig. 4.12(a)). A further increase also increases the RMS error. Therefore, we retain only the first 600 eigenvalues, i.e., about 10%. The condition number of the noise covariance matrix obtained in this way is 1.2×10^7 . From Fig. 4.12(b), which shows the same RMS error as a function of the condition number, we conclude that it is generally useful to keep the condition number below a value of about 10^7 .

4.3.3. Spectral consistency

As explained in Sect. 4.2, the parameterization of the signal must be spectrally consistent with the data. In this section, we demonstrate the importance of this requirement, as this requirement has not been met in previous studies. A series of tests are performed. For each test, two solutions are computed. One, already considered in the previous section, uses the lowpass-filtered design matrix \mathbf{A} , the other one the unfiltered design matrix, \mathbf{A}' (cf. Eq. (4.9)). In all tests, the “true” data are generated using the design matrix \mathbf{A} . The number of eigenvalues which are retained in the data weighting varies between 200 and 1,600.

Fig. 4.12(a), shows the RMS error of the estimated total mass anomalies as a function of the retained eigenvalues. There is little difference between the solutions using design matrix A' compared to A if no more than 600 eigenvalues are retained. Above 600 eigenvalues, the RMS error increases quickly if the design matrix A' is used and reaches values close to the signal. We explain this high RMS error by the fact that the estimated mass anomalies go to zero. When the spectrally consistent design matrix A is used, the RMS error is almost the same (around 20 Gt) if at least 400 eigenvalues are retained. From this experiment, we conclude that spectral consistency is important to obtain high-quality mass anomalies.

4

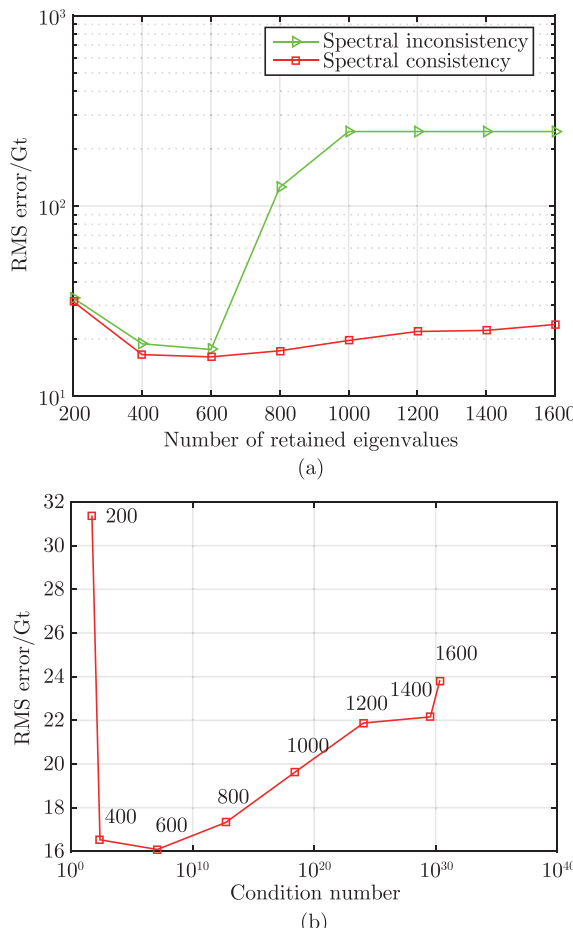


Figure 4.12 RMS errors in estimated mass anomalies as function of (a) the number of retained eigenvalues and (b) the condition number after truncation.

In addition, we perform a series of experiments to demonstrate the importance of using realistic signal spectra in GRACE numerical studies in general. In these tests, the unfiltered design matrix A' is used not only to invert gravity disturbances, but also to simulate them based on annual mass changes (Sect. 4.3.1). In this sense, the mascon functional model in these tests is consistent with the input data. At the same time, the simulated data are not realistic in the sense that the generated signal is not bandlimited unlike signals represented by a truncated spherical harmonic series. Furthermore, the only error source considered in these tests is random error. Data weighting is used to estimate the mass anomalies.

The tests are performed for different numbers of retained eigenvalues in the spectral representation of the matrix C_d . As shown in Fig. 4.13, an unrealistic (not bandlimited) signal spectrum provides error estimates of the mass anomalies that are much too small. If the number of retained eigenvalues exceeds 1,400, the estimated formal RMS uncertainties of the mass anomalies are 10^{-6} Gt. We explain this by a spectral mismatch between signal and noise. Whereas the signal bandwidth is not bandlimited in these experiments, the generated data noise is bandlimited up to a maximum spherical harmonic degree 120. Thus, the signal above degree 120 is considered to be noise-free. Then, the applied data inversion procedure, which suppresses data noise in a statistically-optimal way, manages to use this high-frequency error-free signal in the

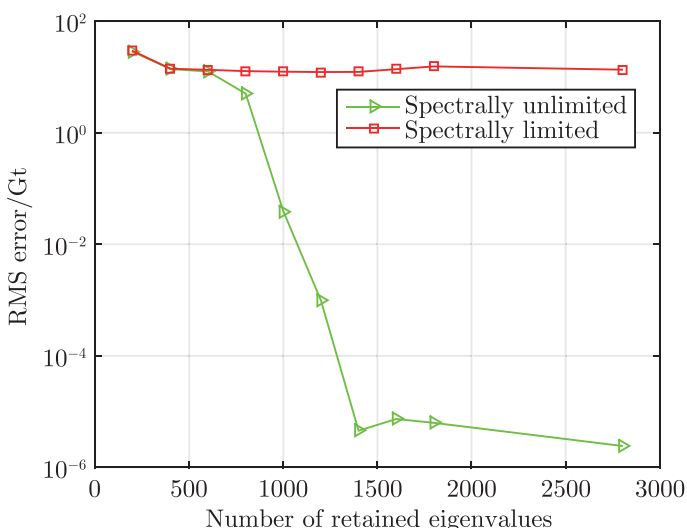


Figure 4.13 RMS errors of estimated mass anomalies over all of Greenland as a function of the number of eigenvalues retained. Data weighting is applied.

recovery of mass anomalies. From these experiments, we conclude that ignoring a proper reproduction of the signal content in numerical tests can lead to over-optimistic results, particularly when a weighted least-squares estimator is used.

This experiment also explains the poor performance of the statistically-optimal data inversion in the presence of spectral inconsistencies, which were discussed in the previous section. In this case, the applied data weighting assigns unrealistically high weights to the high-frequency components of the signal. These signal components, however, have been removed during the lowpassfiltering of the design matrix. Then, the estimated mass anomalies tend to zero when more and more eigenvalues of the matrix C_d are retained.

4.4. Real GRACE data analysis

The performance of the proposed approach is analyzed using real GRACE data. Here we use Release-05 GRACE monthly gravity field solutions from CSR from January 2003 – December 2013. Missing months are not interpolated, but simply omitted. Each monthly solution is provided as a set of SHCs complete to degree 96, including a full noise covariance matrix. We replace the C_{20} coefficient of all monthly solutions with estimates based on satellite laser ranging (Cheng et al., 2013). Degree-1 coefficients are taken from Swenson et al. (2008) including noise variances. The Glacial Isostatic Adjustment (GIA) signal in the GRACE data is removed using the model compiled by A et al. (2013).

The data are used to compute a time-series of Greenland mass anomalies. To that end, we follow the recommended data processing setup, which is summarized in Table 4.2. We compute both weighted least-squares solutions and ordinary least-squares solutions.

The results are analyzed in three different ways. In Sect. 4.4.1, we quantify the noise in the time-series of the estimated Greenland mass anomalies using only the data themselves. The method applied is briefly described in Sect. 4.4.1. In Sect. 4.4.2, we compare the GRACE-based time-series (after correction for ice discharge) with time-series of SMB synthesized from the RACMO 2.3 model. We evaluate mass anomalies not only for Greenland as a whole, but also for individual drainage systems. In line with van den Broeke et al. (2009), we group the 23 patches into five drainage systems: North (N), Northwest (NW), Southwest (SW), Southeast (SE) and Northeast (NE), cf. Fig. 4.14. In Sect. 4.4.3, a comparison between the estimates in this book and other mascons

solutions is presented.

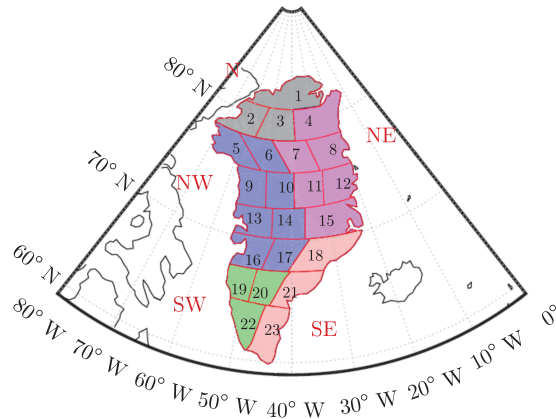


Figure 4.14 Partitioning of Greenland into 23 mascons and the definition of the five individual drainage systems.

4.4.1. Estimating mass anomaly uncertainties

First of all, we quantify the noise in mass anomaly time-series using an original approach that does not require an independent reference. The approach is based on the assumptions that i) the true signal in the data time-series is close (but not necessarily equal) to a combination of an annual periodic signal and a linear trend; ii) the noise in the data time-series is uncorrelated and (optionally) non-stationary; and iii) the time-series of the noise variances is known up to a constant scaling factor. The basic idea is to approximate the original data time-series \mathbf{d} with a regularized one \mathbf{x} , for which purpose the following function is minimized:

$$\Phi[\mathbf{x}] = \frac{1}{\sigma_d^2} (\mathbf{d} - \mathbf{x})^T \mathbf{P} (\mathbf{d} - \mathbf{x}) + \frac{1}{\sigma_x^2} \mathbf{x}^T \mathbf{R} \mathbf{x}, \quad (4.23)$$

where \mathbf{P} is a diagonal weight matrix that accounts for temporal variations of noise level; σ_d^2 is the noise variance; σ_x^2 is the signal variance; and \mathbf{R} is a regularization matrix designed to avoid periodic annual signals and a linear trend in the data. An estimation of the noise variance σ_d^2 and the signal variance σ_x^2 is a part of the regularization procedure. To that end, the Variance Component Estimation (VCE) technique (Koch and Kusche, 2002) is used. This technique is iterative: at each iteration, the estimates of σ_d^2 and σ_x^2 are updated, which allows for a better regularization of the original time-series and thus

a better estimation of σ_d^2 and σ_x^2 at the next iteration. Once the procedure converges, the latest estimate of σ_d is used as a measure of the standard deviation of the random noise in the data under consideration. A more detailed presentation of this approach will be the subject of a separate publication.

In this book, we use this approach to quantify the uncertainties in mass anomaly estimates both for all of Greenland and for the five drainage systems mentioned above.

Table 4.3 summarizes the main results. They confirm that, compared to an ordinary least-squares solution, optimal data weighting significantly reduces random noise in mass anomaly estimates. The largest reduction, 69%, is observed for the SW drainage system. This is likely due to a relatively large contribution of random noise to the estimated mascon of this drainage system, making the statistically-optimal data weighting particularly efficient. An increased level of random noise over the SW drainage system can be explained by its relatively small size. The smallest reduction in random noise observed in the NE drainage system, is still substantial, about 35%. For the whole of Greenland, the random noise is reduced by a factor of two.

Table 4.3 VCE-based noise standard deviations (in Gt) of estimated mass anomalies for i) the whole of Greenland, and ii) five individual drainage systems

Data weighting	N	NW	SW	SE	NE	GrIS
No	14	49	30	39	34	33
Yes	9	16	9	17	17	16
Reduction	35%	67%	69%	56%	52%	50%

4.4.2. Validation against modelled SMB time-series

The estimated mass anomalies are compared with modeled SMB estimates over the 2003–2013 period, computed with the Regional Atmospheric Climate Model (RACMO) version 2.3 (Noël et al., 2015). The spatial resolution of the RACMO 2.3 model is 11 km × 11 km (see Table 4.1). We integrate the daily SMB estimates over time to produce daily mass anomalies, and then compute on their basis monthly mean values to match the temporal resolution of GRACE. Finally, the computed mass anomalies are spatially integrated over individual drainage systems and over all of Greenland, respectively.

The mass anomalies derived from GRACE account for both SMB and ice discharge. According to van den Broeke et al. (2009), ice discharge manifests itself mainly as a long-

term trend, while the seasonal mass variations are largely attributed to surface processes. In view of that, we de-trend both SMB- and GRACE-based time-series before comparing them. For this purpose, we approximate each of them with the analytic function $f(t)$:

$$\begin{aligned} f(t) = & A + B(t - t_0) + C \sin \omega(t - t_0) + D \cos \omega(t - t_0) + \\ & E \sin 2\omega(t - t_0) + F \cos 2\omega(t - t_0), \end{aligned} \quad (4.24)$$

where A to F are constant coefficients estimated by ordinary least-squares, t_0 is the reference epoch defined as the center of the considered time interval, and $\omega = \frac{2\pi}{T}$ with $T = 1$ year. The de-trending includes the first two terms of $f(t)$. After de-trending, the remaining GRACE-based and SMB-based time-series are compared. In the comparison, GRACE-based mass anomalies produced both with and without data weighting are considered. The de-trended GRACE-based and SMB-based time-series are shown in Fig. 4.15 with and without using data weighting. Remarkable is the erratic behavior of the GRACE-based time-series per drainage system when no data weighting is used. This erratic behavior is averaged out when computing mass anomaly times-series for all of Greenland.

Fig. 4.16 shows the time-series of the differences between GRACE-based and SMB-based time-series of mass anomalies. The statistics of the differences are given in Table 4.4. When data weighting is used, the differences are much smaller compared to the solutions without data weighting. The most significant improvement is achieved in the SW drainage system, which is consistent with the results obtained with the VCE technique (cf. Sect. 4.4.1). At the same time, the improvement observed for all of Greenland is smaller, about 17%, than that of individual drainage systems (24%–47%). This is probably due to the fact that when summing up mass anomalies per mascon to get the mass anomalies for the whole of Greenland, the random noise is reduced by averaging out. Therefore a relatively low level of random noise can be achieved for the estimates of Greenland as a whole, compared with the estimates per mascon. However this does not affect the determination of other optimal parameters in Table 4.2. Since our operation (i.e., summing up mass anomalies per mascon to get the mass anomalies of all of Greenland) is applied to the final estimates. As a result, the remaining difference in Fig. 4.16(f) should be explained by residual physical signals rather than by noise. Such signals may reflect non-linear mass variations not related to SMB, such as inter-annual variability in ice discharge or meltwater retention. A physical interpretation of these signals is beyond the scope of this study.

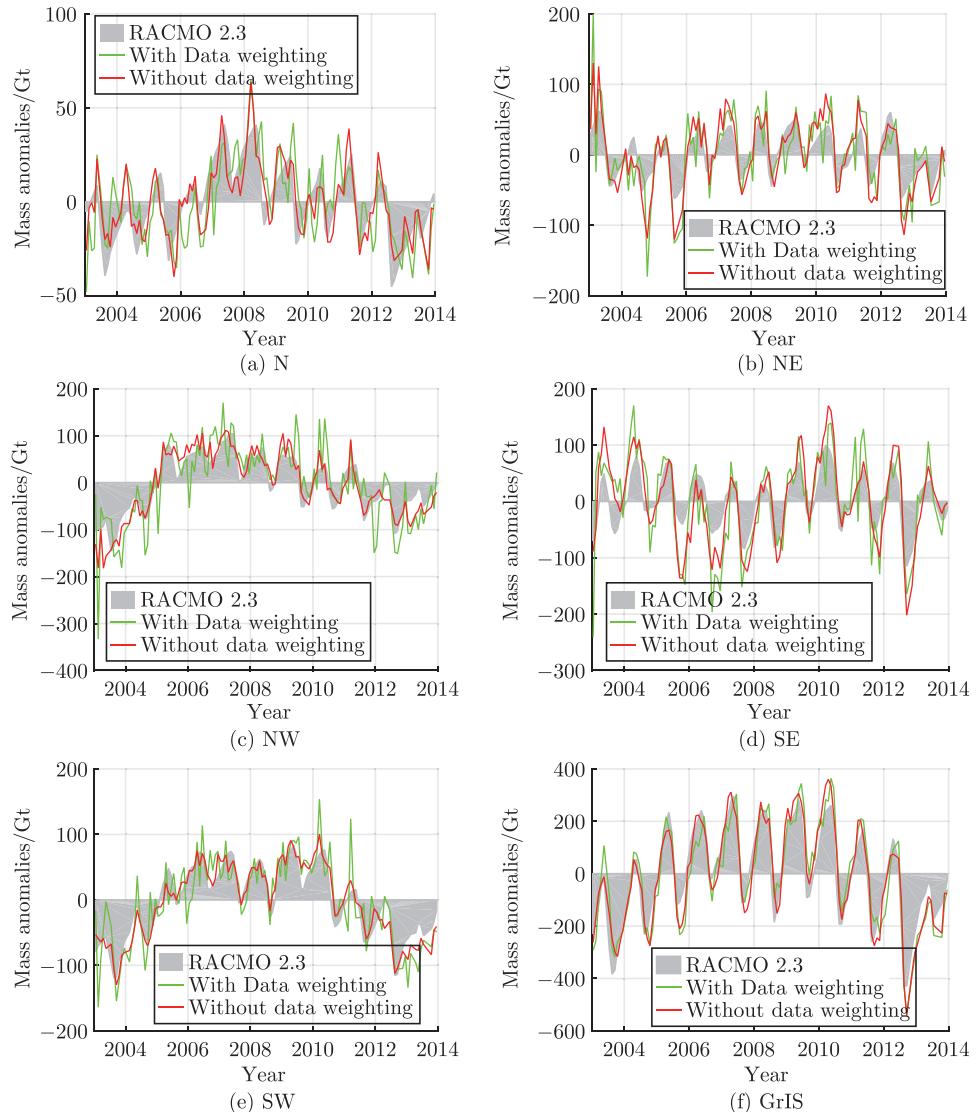


Figure 4.15 De-trended mass anomaly time-series based on modelled SMB and GRACE data, respectively, for individual drainage systems and the whole of Greenland. GRACE-based time-series were computed with (red) and without (green) data weighting.

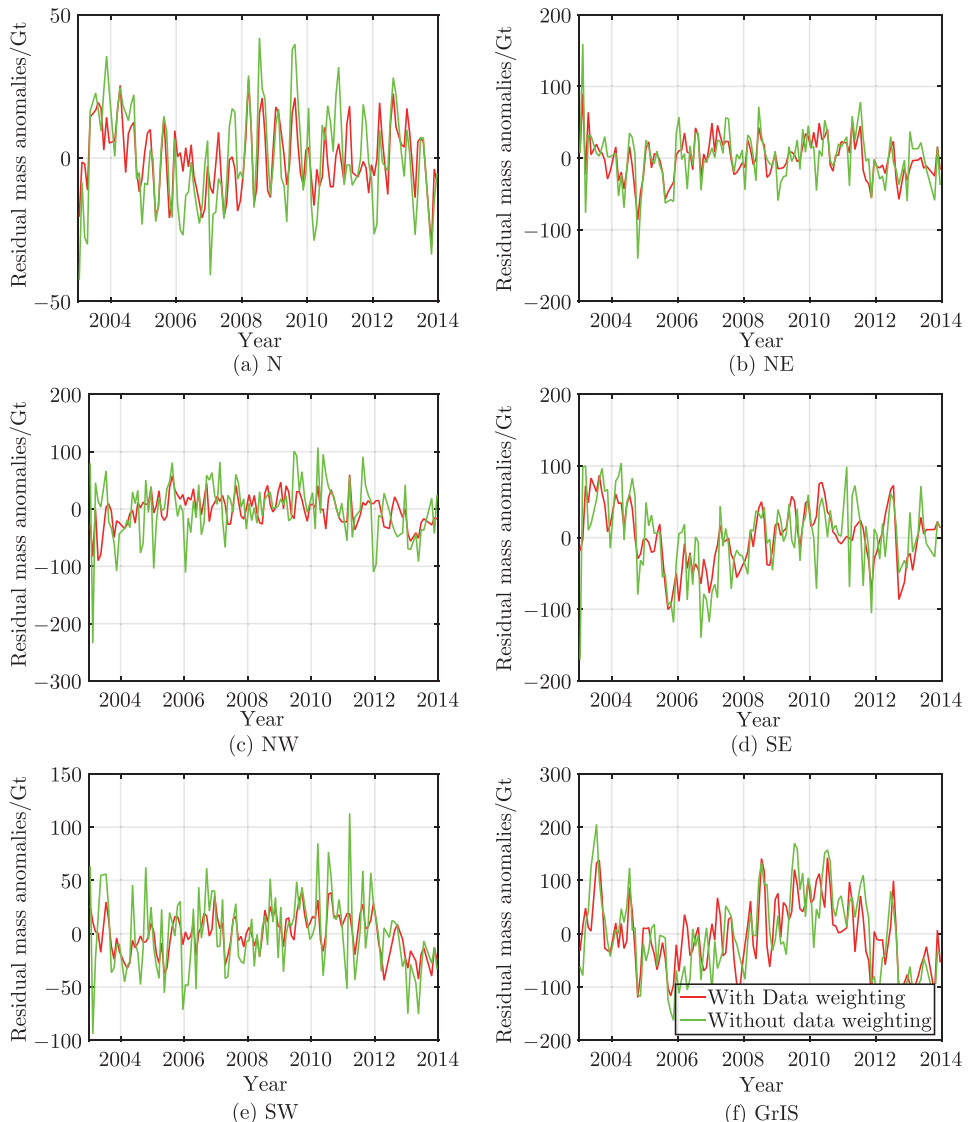


Figure 4.16 Differences of SMB-based and GRACE-based de-trended mass anomaly time-series for individual drainage systems and the whole of Greenland. GRACE-based time-series were computed with (red) and without (green) data weighting.

Table 4.4 Ice discharge-corrected RMS differences (in Gts) between GRACE-based mass anomaly estimates and SMB-based mass anomalies for i) all of Greenland and ii) five individual drainage systems

Data weighting	N	NW	SW	SE	NE	GrIS
No	16	48	34	54	37	76
Yes	12	27	18	41	27	63
Reduction	28%	44%	47%	24%	27%	17%

4.4.3. Comparison with Greenland mass anomalies from other studies

The mass anomaly estimates are further compared with those based on existing global and regional mascon solutions, as well as with results from the literature. The available global mascon solutions discussed in this book are the products released by JPL (Watkins et al., 2015), GSFC (Luthcke et al., 2013) and CSR (Save et al., 2016). Note that these mascon solutions are estimated from GRACE KBR data, whereas the method developed in this book uses GRACE SHCs. We also include the regional mascon solution from Wouters et al. (2008), which also uses GRACE SHCs as input. As shown in Fig. 4.17,

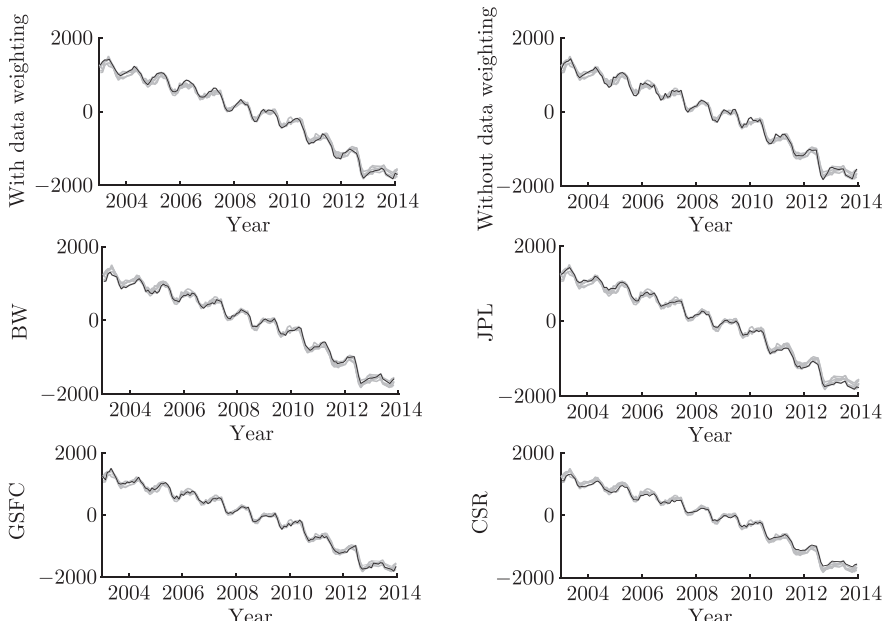


Figure 4.17 The mass anomaly time-series produced in this book with data weighting and without data weighting, as well as by Wouters et al. (2008) (marked as “BW”), JPL, GSFC and CSR. The unit of Y-axis is mass variation in Gt. Each plot highlights only one solution (black line), whereas other solutions are shown in grey.

different mass anomaly time-series over the whole of Greenland are in very good agreement with each other. The same applies to the linear trend estimates shown in Table 4.5.

Table 4.5 Greenland mass anomalies trends over the period 2003–2013 (in Gt/yr) estimated from different solutions and experimental setups

Different estimates	Trend
With data weighting (this study)	-286
Without data weighting (this study)	-276
JPL mascon	-289
CSR mascon	-262
GSFC mascon	-283
Wouters et al. (2008)	-264
Velicogna et al. (2014)	-280
Schrama et al. (2014)	-278

As before, we use the VCE-based estimation of random noise standard deviations and a validation against modelled SMB estimates to assess the quality of the various mascon solutions. The smallest noise standard deviation (16 Gt) is observed for the solution produced in this book with the optimal data weighting (Table 4.6). A comparable noise standard deviation (19 Gt) is estimated for the JPL solution, while the standard deviations for other solutions are much larger. When validated against independent SMB output, the solution produced in this book with the optimal data weighting again shows the best performance (see Table 4.6). From Tables 4.6, it can be seen that relatively low VCE-based standard deviations in the JPL solutions do not indicate better quality. This could be due to the fact that the application of spatio-temporal constraints in the production of these solutions could reduce random noise, but at the cost of biasing the estimates towards a priori information, which is reflected in the applied constraints. The bias becomes apparent when validated with independent data such as SMB model estimates. This justifies our decision not to apply any spatial or temporal constraints in producing our solutions in order to minimise bias. Rapid mass loss in an area of a limited size is a particularly challenging scenario for any mass anomaly estimation method. In particular, the impact of any bias caused by the applied constraints can be particularly large in this case. An in-depth discussion of this issue is beyond the scope of this manuscript. A further discussion of the biases introduced into mascons solutions by various spatio-temporal constraints will be the subject of a separate paper.

Table 4.6 VCE-based noise standard deviations (in Gt) of estimated mass anomalies (left column) and ice discharge-corrected RMS differences (in Gt) between GRACE-based mass anomaly estimates from different mascon solutions and SMB-based mass anomalies (right column). All the estimates refer to entire Greenland

Different estimates	VCE-based noise standard deviations	Ice discharge-corrected RMS differences
With data weighting (this study)	16	63
Without data weighting (this study)	33	76
JPL mascon	19	73
CSR mascon	29	70
GSFC mascon	45	76
Wouters et al. (2008)	36	79

4.5. Summary

In this book, we proposed an improved mascon approach compared to the previous studies of Forsberg and Reeh (2007) and Baur and Sneeuw (2011). Based on numerical experiments, we optimise a number of parameters, which are listed in Table 4.2. The proposed method allows the estimation of mass anomalies over Greenland in a statistically-optimal way, by propagating the full noise covariance matrices of the SHCs into full noise covariance matrices of the gravity disturbances at altitude, which are then used as data in the mass anomaly estimation scheme. We show that the data weighting significantly improves the accuracy of the estimated mass anomalies. The high condition number of the noise covariance matrix is successfully addressed using a truncated eigenvalue decomposition, which retains about 10% of the eigenvalues corresponding to a condition number of about 10^7 . We have also shown that the optimal size of a mascon is about $300 \text{ km} \times 300 \text{ km}$, which implies about 23 mascons for Greenland. This result is consistent with the spatial resolution of GRACE reported in the literature (Longuevergne et al., 2010; Ramillien et al., 2004; Beighley et al., 2011). Furthermore, we have proven that the spectral consistency of the mass anomaly model and the data is very important to obtain accurate estimates of the mass anomalies. If data weighting is applied, a spectral inconsistency makes the mass anomalies recovery non-robust and provides severely biased estimates. This is more pronounced when more eigenvalues of the noise covariance matrix are retained. The high-frequency components of the model are then over-weighted, resulting in gravity anomalies close to zero due to the lack of high-frequency signal in the data. The maximum degree in the low-pass filter used to maintain a spectral consistency must be consistent with the GRACE solutions utilized to generate the pseudo-observations. Specifically, in the simulation, we choose a maximum degree of 120, which is consistent with the DMT

solutions. However, in the real data processing, the CSR solutions are utilized. Then, the maximum degree is 96, in line with the CSR solutions.

It is worth to stress that the set of parameters shown in Table 4.2 is optimal if the main objective is to estimate mass anomalies over a one-year interval. This scenario represents a kind of intermediate choice between the two extremes of a monthly signal and an average signal over a multi-year time-interval (e.g., a long-term linear trend). In our latest studies, we have found that the optimal data processing scenario definitely depends on the temporal scale of interest. For example, if the main focus is on a long-term trend, the impact of random noise (north-south stripes) is minor, so that other types of noise (particularly, the parameterization error) become dominant. In this case, the way to improve the quality of the estimates is to reduce the size of individual mascons, and not to apply a data weighting based on the provided error covariance matrices of the GRACE monthly solutions. On the other hand, if the main research interest is the month-to-month mass anomaly variations, random noise by far exceeds noise of other types, including the parameterization errors. In this case, the best results are obtained when the size of the individual mascons is relatively large, whereas the data weighting based on the provided error covariance matrices is switched on. These and other results are discussed in detail in a separate manuscript.

We have also applied the proposed data processing scheme to real GRACE data and computed mass anomaly time-series for 5 drainage systems and all of Greenland. Using VCE, we found that when a proper data weighting is used, the accuracy of the estimated mass anomalies increases by a factor of 1.5 to 3.0, depending on the drainage system. A comparison of the GRACE-based mass anomalies with the modelled SMB mass anomalies shows that proper data weighting provides a better fit of GRACE-based and SMB-based mass anomalies, with improvements ranging from 24% to 47% depending on the drainage system. We take this as an indication that a proper data weighting provides much more accurate estimates of mass anomalies. However, the improvement is marginal for all of Greenland. This is likely due to the relatively minor role of random noise in mass anomaly estimation over very large areas.

5

Seasonal mass variations show timing and magnitude of meltwater storage in the Greenland Ice Sheet

5.1. Introduction

The phenomenon of meltwater storage in GrIS was analyzed by Ran et al. (2018c) using data from GRACE in combination with SMB and ice discharge estimates. The results are summarized in this chapter. GRACE is a powerful tool for monitoring mass variations over Greenland (including peripheral glaciers and tundra), on monthly to multi-year time scales. These variations result from the combination of three effects: i) mass accumulation due to surface mass balance (SMB), ii) mass loss due to ice discharge to the ocean, and iii) sub-glacial meltwater accumulation and run-off.

Recent GrIS mass loss has been quantified in several studies (e.g., Shepherd et al., 2012; Schrama et al., 2014; Velicogna et al., 2014). Furthermore, several authors have estimated the contribution of SMB and ice discharge to this mass loss individually (van den Broeke et al., 2009; Enderlin et al., 2014; Velicogna et al., 2014; van den Broeke et al., 2016). To quantify the contribution of SMB, regional climate models (RCMs) are typically used, such as the Regional Atmospheric Climate Model v. 2 (RACMO2) (Ettema et al., 2009), MAR (Fettweis et al., 2005) and Hirham (Christensen et al., 1996). The contribution of annual ice discharge rates is estimated by combining ice flow velocity data and ice thickness data at flux gates (Thomas et al., 2000). Importantly, ice velocities have increased on average during the last two decades (Moon et al., 2012), and therefore need to be monitored on a regular basis. The motivation for examining the multi-year mass variation trend and acceleration budgets in this chapter is twofold. First, we compare the estimates of the long-term mass variations with the values reported in the literature over the same time interval to validate the novel approach proposed in Chapter 4. Second, we attempt to verify the accuracy of long-term mass variations modeled by SMB using

GRACE data and ice discharge observations.

The analysis of GrIS mass variations at the intra-annual time scale is still in its infancy. This is largely because i) the accuracy and resolution of GRACE monthly solutions are relatively poor, as compared to long-term trend estimates, and ii) ice velocity data at this time scale are scarce (typically, only a few estimates per year, often spanning only a few years). The first attempt to combine GRACE data and SMB modeling in order to evaluate an ice dynamics model of the GrIS at the monthly time scale was made by Schlegel et al. (2016). The only study of multi-regional intra-annual variations of GrIS outlet glacier velocities was conducted by Moon et al. (2014), who analyzed 55 marine-terminating glaciers in northwest and southeast Greenland over the period 2009–2013.

5

The GrIS mass balance is also characterized by supra-, en-, and subglacial meltwater retention. An example is the abundance of supraglacial lakes, primarily in west Greenland, which store water during the melt season (Selmes et al., 2011). Subglacial hydrology is an area of active research (see e.g., Chandler et al., 2013; Slater et al., 2015). Until now, however, time-varying meltwater retention has been mostly studied at the local scale. For example, Rennermalm et al. (2013) quantified meltwater retention in a small watershed ($36\text{--}65 \text{ km}^2$) near Kangerlussuaq. They suggested that ~54% of the liquid water is retained in this watershed for one to six months. An exception to this is the study by Van Angelen et al. (2014). From fitting de-trended GRACE observations and SMB model output, they found that the mean period of meltwater retention at the whole-ice-sheet scale is ~18 days.

In this chapter, we systematically analyze the individual contributions to total inter- and intra-annual mass variations over Greenland at both regional and whole-ice-sheet scales. This includes isolating the signal associated with the seasonal accumulation and run-off of meltwater. For this purpose, we combine observations of total mass variations from GRACE with observations of ice discharge to the ocean (Enderlin et al., 2014; Moon et al., 2014) and modeled SMB estimates from RACMO2.3 (Noël et al., 2015). Due to the limited spatial resolution of GRACE data, the estimates obtained cover both the GrIS and the areas outside the GrIS, including the tundra and the peripheral glaciers disconnected from the GrIS.

The structure of this chapter is as follows. Sect. 5.2 describes the adopted parameterization. The data used in this chapter are introduced in Sect. 5.3. In Sect. 5.4, we present and discuss our results. Finally, we present our conclusions in Sect. 5.5.

5.2. Adopted parameterization

To study GrIS mass variations on the regional scale, we use a variant of the mascon approach presented in Chapter 4. We update the recommended parameterization of 23 mascons, by subdividing the territory of Greenland into 28 mascons. This is due to the fact that the mass losses of the GrIS are concentrated in the narrow coastal zone close to the ice sheet margin. To take this information into account, we introduce additional mascons of 100 km width along the ice mask border. The resulting parameterization is shown in Fig. 5.1.

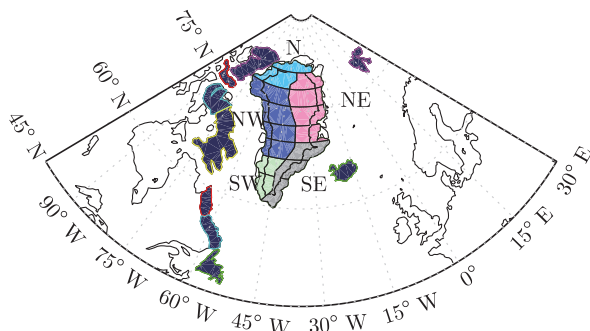


Figure 5.1 The 28-patch parameterization of Greenland used in this book for GRACE data processing. For the purpose of further analysis, these patches are merged into five drainage systems (N, NE, SE, SW, and NW), roughly defined as in van den Broeke et al. (2009). 55 glaciers used to calculate seasonal ice discharge are marked as red pentagrams.

In addition, and similar to Chapter 4, we include nine patches around Greenland to attenuate leakage of signals from outside Greenland. The data processing scheme recommended in Chapter 4 is used in the computations presented below, unless otherwise noted.

Finally, we aggregate the 28 mascons within Greenland into five drainage systems (cf. Fig. 5.1), similar to Luthcke et al. (2006a) and van den Broeke et al. (2009). We refer to these drainage as: i) North (N); ii) Northwest (NW); iii) Southeast (SE); iv) Southwest (SW); and v) Northeast (NE) (Fig. 5.1). We have shifted the boundary between the NW and SW drainage systems slightly southward compared to Luthcke et al. (2006a) and van den Broeke et al. (2009), to ensure that the SW drainage system is mostly restricted to land-terminating outlet glaciers. In addition, whole-ice-sheet anomalies are obtained by summing over all 28 Greenland mascons.

5.3. Data

In addition to the GRACE monthly solutions, we also use the SMB output from RACMO2.3 (Noël et al., 2015). It is worth noting that previous work on the sources of current GrIS mass loss used relative SMB and ice discharge anomalies with respect to an equilibrium state (1961–1990) (e.g., van den Broeke et al., 2009; Velicogna et al., 2014). Effectively, this means that the time-series of mass anomalies have been de-trended to ensure that they are close to zero during the reference equilibrium period. Here, we use time-series of absolute total SMB, and ice discharge mass anomalies, i.e., without referring to a hypothesized equilibrium state. This allows us to extract more information from the data. For example, absolute mass anomalies related to ice discharge cannot increase with time, which is a valuable constraint that facilitates the correct interpretation of the results. In addition, because GRACE senses mass anomalies not only within the GrIS, but also in ice caps and tundra areas, we use SMB estimates that includ non-GrIS areas of Greenland, too.

5

For more basic information on the GRACE data and the RACMO 2.3 output, we refer to Chapter 4. Moreover, we also use ice discharge observations on both multi-year and intra-annual scales. A brief explanation of how they were obtained is given below.

5.3.1. Ice discharge on multi-year scale

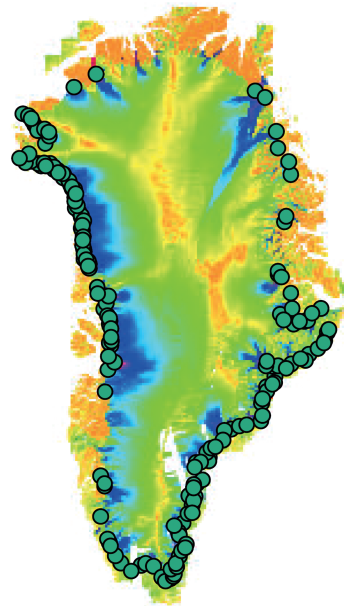
The long-term ice discharge of the GrIS during 2003–2012, which was derived for the flux gates within 5 km of the termini (Enderlin et al., 2014), is used to investigate the GrIS mass variations on a multi-year scale. In this book, 178 outlet glaciers are considered (cf. Fig. 5.2). For more details on this dataset, we refer to Enderlin et al. (2014).

5.3.2. Ice discharge on intra-annual scale

To investigate ice discharge on an intra-annual scale, we consider 55 glaciers (cf. Fig. 5.3) in the northwestern and southeastern parts of Greenland, which are believed to be the two largest contributors to ice discharge in Greenland. The data cover the time period 2009–2013. We use ice flow velocities derived from TerraSAR-X image measurements (Moon et al., 2014) and ice thicknesses from the IceBridge BedMachine Greenland version 2 data (Morlighem et al., 2015) (cf. Fig. 5.4). Ice discharge (D) for a given glacier is defined as the ice mass flux through the flux gate (f) close to the glacier terminus (within

~5 km):

$$D = \rho \int_f h(\mathbf{v} \cdot \mathbf{n}) df, \quad (5.1)$$



5

Figure 5.2 Outlet glaciers (178 in total) considered by Enderlin et al. (2014) to infer the long-term ice discharge of GrIS. The base-map is shown as the velocities during 2007–2010 by Moon et al. (2014).

where h is the ice thickness; \mathbf{n} is the unit vector directed outwards normally to the flux gate; \mathbf{v} is the ice flow velocity; and ρ is the ice density. It is worth mentioning that when selecting flux gates, one needs to pay attention to the variations of the terminus position by checking the images of the glaciers during the whole time interval, to make sure that the flux gate is in the upstream of the terminus. Furthermore, a flux gate should cover the entire outlet glacier up to the ice flow edges. To compute D , we discretize the flux gates into intervals of nearly 200 m in length. The distance of the last interval is adjusted to ensure that the ice flow edge is sampled. We then use the values (h, \mathbf{v} and \mathbf{n}) defined for the center of each interval, assuming that they are constant over the entire interval. Then Eq. 5.1 becomes

$$D = \rho \sum_{i=1}^N d^i h^i (\mathbf{v}^i \cdot \mathbf{n}), \quad (5.2)$$

where N is the total number of intervals of the flux gate and d^i is the length of the i -th interval.

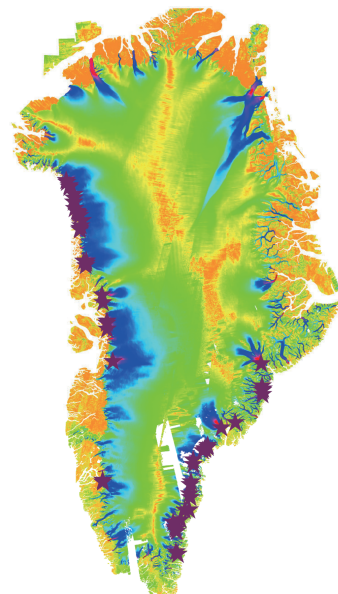


Figure 5.3 Similar to Fig. 5.2, but for the geographic distribution of 55 glaciers used to infer the ice discharge of GrIS on the intra-annual time scale.

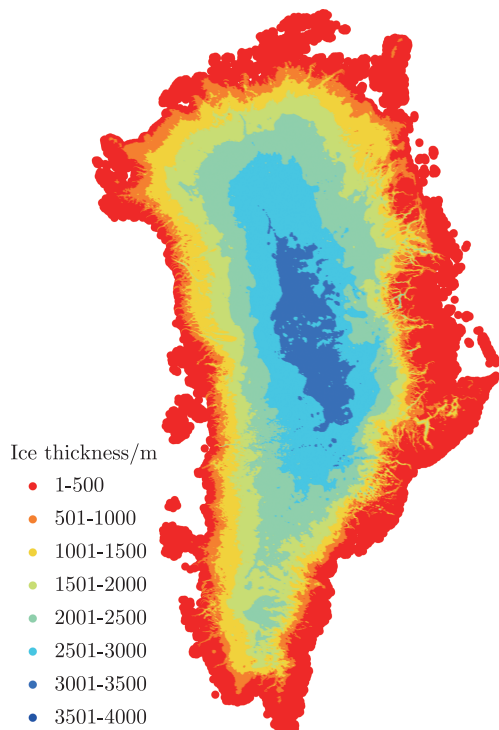


Figure 5.4 Ice thickness of Greenland from the IceBridge BedMachine Greenland version 2 data.

5.4. Results and Discussion

5.4.1. Multi-year mass trend and acceleration budgets

First, we examine multi-year mass trends and accelerations in terms of the total mass balance and the contributions thereto from SMB and ice discharge (cf. Fig. 5.5). We approximate each mass anomaly time-series (cf. Figs. 5.5–5.10) with the following analytical function:

$$f(t) = a_1 + a_2(t - t_0) + a_3 \frac{(t - t_0)^2}{2} + a_4 \sin \omega t + a_5 \cos \omega t + a_6 \sin 2\omega t + a_7 \cos 2\omega t, \quad (5.3)$$

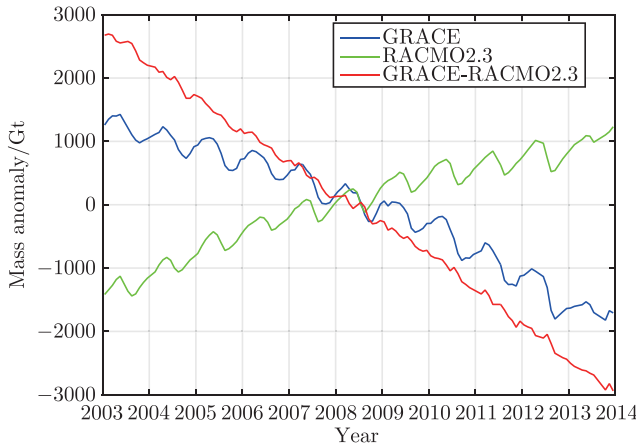


Figure 5.5 Time-series of mass anomalies over the period 2003–2013 for the entire GrIS: total mass anomalies from GRACE (blue), cumulative SMB anomalies from RACMO2.3 (green), and the difference between them, “Total-SMB” (red).

where a_1, \dots, a_7 are parameters to be estimated, t_0 is a reference epoch defined as the middle of the time interval considered (i.e., 2003–2013), and $\omega = 2\pi/T$ with $T = 1$ year. Our estimate of the total-mass linear trend, a_2 , which is based on the primary GRACE data time-series, is -286 ± 21 Gt/yr for 2003–2013. This value is consistent with those previously published: -280 ± 58 Gt/yr for January 2003 to December 2013 (Velicogna et al., 2014) and -278 ± 19 Gt/yr for the same period (Schrama et al., 2014). Our estimates of trend uncertainties are composed of signal leakage (including both signals leaking from outside Greenland and signals from inside Greenland leaking between the mascons), the error of the GIA model (we set it at 50% of the signal), the measurement errors of GRACE propagated from the full variance-covariance matrix of

monthly solutions, and the uncertainty associated with a particular choice of the oceanic mascon layout (Bonin and Chambers, 2013) (cf. Table 5.1). Unlike Velicogna and Wahr (2013), we do not consider errors from atmospheric and oceanic circulation corrections, due to their small contribution.

Table 5.1 Contribution of different error sources to the error in the total GrIS mass trend estimated from GRACE data (Gt/yr)

Contributor	Signal leakage	GIA correction	Ocean parameterization	GRACE data	Total error
Error	15	8	7	10	21

We also examine the contributions of SMB and ice discharge to the total mass trend over the reduced time interval 2003–2012, to be consistent with the ice discharge record, which ends in 2012 (Table 5.2). The multi-year average mass gain from SMB (RACMO2.3) over this period is 231 ± 122 Gt/yr. The standard error is calculated by assuming a 9% error in the accumulation and a 15% error in the meltwater runoff signals modeled by RACMO2.3. The time-series of cumulative mass anomalies related to ice discharge and other non-SMB processes is obtained as the difference between the total mass variations and the cumulative SMB-related ones; this difference is referred to as “Total-SMB” (“Total minus SMB”, cf. red curve in Fig. 5.5). The associated rate of linear mass loss over 2003–2012 is 508 ± 124 Gt/yr, which perfectly matches the ice discharge estimate of Enderlin et al. (2014), 520 ± 31 Gt/yr.

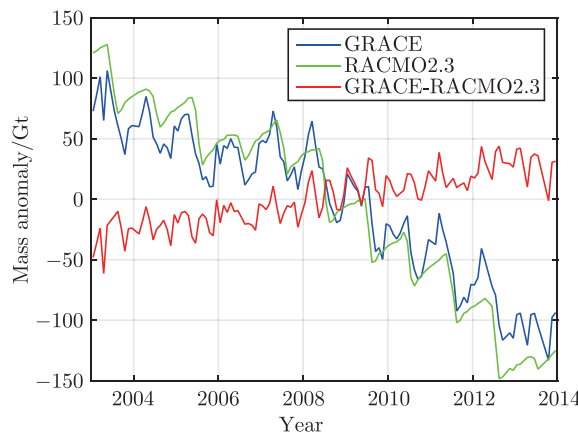


Figure 5.6 Same as Fig. 5.5, but for the N drainage system indicated in Fig. 5.1.

Next, we present the results of a similar analysis for the individual DSSs. The largest total mass losses are observed by GRACE in the NW and SE DSSs (cf. Figs. 5.6–5.10 and Table

5.2). These two DSs account for 76% of the total mass loss over Greenland. However, the inter-annual behavior of these DSs is different. SE loses mass with an approximately constant rate over the whole considered period. In contrast, NW is relatively stable over the period 2003–2005, but starts loosing mass thereafter. The remaining three DSs lose mass at much lower rates. Notably, two of these DSs (N and SW) show a similar behavior: they are relatively stable over the period 2003–2009, and start loosing mass in 2010. These findings are consistent with Velicogna et al. (2014). The SMB is negative in two DSs (N and SW) (cf. Table 5.2). However, with a large proportion of land-terminating glaciers, ice losses from ice discharge are an order of magnitude lower there than in the NW and SE DSs (cf. Figs. 5.6–5.10), resulting in only modest total mass loss despite the negative SMB.

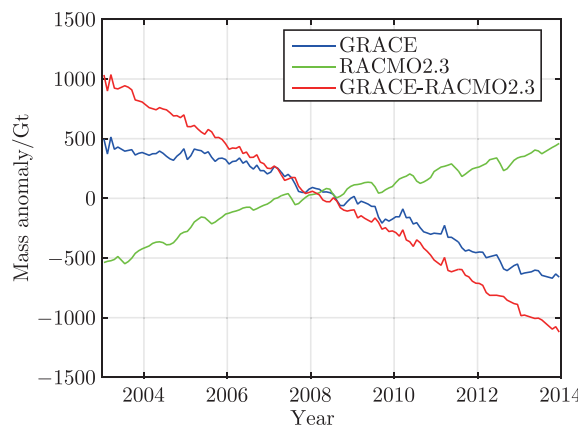


Figure 5.7 Same as Fig. 5.5, but for the NW drainage system.

The long-term trends of Total-SMB residuals in the DSs of NW, NE, and SW are consistent with the ice discharge estimates from Enderlin et al. (2014) within the error bar (Table 5.2). This suggests robustness of the RACMO2.3 long-term SMB trends there, under the assumption that the meltwater storage signal is mainly seasonal. In the SE and N, however, we find relatively large discrepancies between our Total-SMB estimates and ice discharge observations of Enderlin et al. (2014). Under the conditions of realistic GRACE error estimates and minimal multi-year meltwater storage, all these inconsistencies indicate a precipitation overestimation in the SE and an underestimation in the N in RACMO2.3. However, it is also important to keep in mind that discharge estimates are relatively inaccurate in the SE because of various sources of large uncertainties: ice velocities (due to a decorrelation of SAR images in the presence of fast ice flows), ice thicknesses, and corrections for SMB signals at the locations between the flux gates and the grounding line.

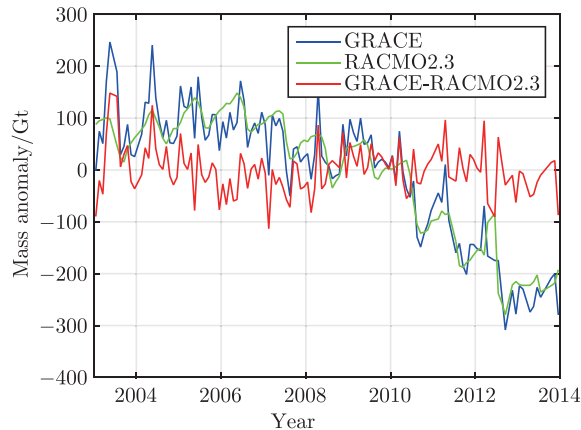


Figure 5.8 Same as Fig. 5.5, but for the SW drainage system.

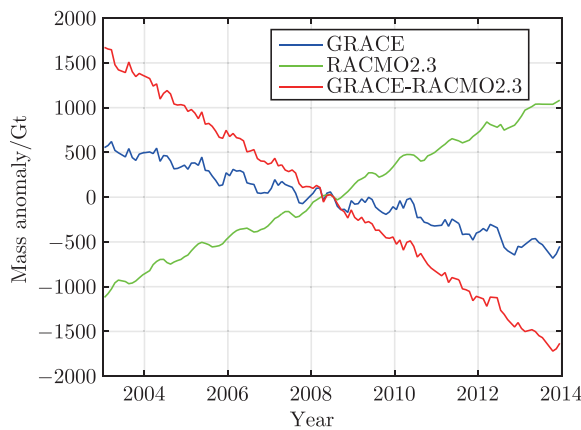


Figure 5.9 Same as Fig. 5.5, but for the SE drainage system.

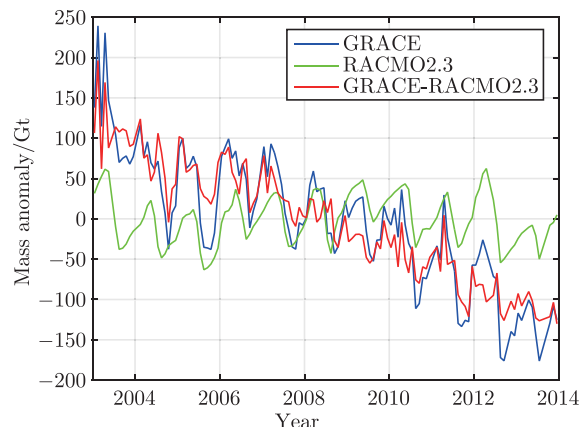


Figure 5.10 Same as Fig. 5.5, but for the NE drainage system.

Average accelerations of mass anomalies over the period 2003–2012 for all of Greenland are also estimated using Eq. 5.3 (parameter a_3). The SMB ($-29.7 \pm 2.7 \text{ Gt/yr}^2$) contributes with 95% to the total acceleration observed by GRACE ($-31.1 \pm 8.1 \text{ Gt/yr}^2$) (Table 5.3). This is close to the estimates of Velicogna et al. (2014), who estimated the contribution of the SMB to the total GrIS mass loss acceleration at 79%. The contribution of the residual term “Total-SMB” to the mass loss acceleration of entire Greenland is statistically insignificant. The analysis of individual drainage systems leads to similar conclusions (cf. Table 5.3).

Table 5.2 Linear mass change rates over the period 2003–2012 for individual drainage systems: Total, SMB-related, and “Total-SMB” (GRACE minus RACMO2.3), as well as ice discharge (Gt/yr). The sign of the “Total-SMB” estimates is changed to make them directly comparable with the ice discharge estimates

Contributor	N	NW	NE	SW	SE	GrIS
Area (10^{12} m^2)	0.26	0.69	0.60	0.21	0.40	2.16
Total (GRACE)	-16 ± 11	-107 ± 23	-20 ± 16	-40 ± 10	-105 ± 23	-277 ± 21
RACMO 2.3	-23 ± 11	84 ± 28	2 ± 20	-29 ± 27	197 ± 39	231 ± 122
-(Total-SMB)	-6 ± 16	190 ± 36	22 ± 26	1 ± 29	300 ± 45	508 ± 124
Ice discharge	21 ± 13	206 ± 14	41 ± 10	18 ± 7	234 ± 20	520 ± 31

Table 5.3 Acceleration of mass change over the period 2003–2012 for individual drainage systems: total, SMB-related, and “Total-SMB” (GRACE minus RACMO2.3), as well as ice discharge (Gt/yr 2). The sign of the “Total-SMB” estimates is changed to make them directly comparable with the ice discharge estimates

Contributor	N	NW	NE	SW	SE	GrIS
Total (GRACE)	-2.9 ± 1.5	-15.6 ± 3.1	-1.1 ± 2.9	-10.9 ± 4.2	-0.8 ± 5.2	-31.1 ± 8.1
RACMO 2.3	-2.9 ± 0.4	-13.0 ± 1.1	-0.4 ± 0.2	-12.8 ± 0.9	-0.7 ± 0.4	-29.7 ± 2.7
-(Total-SMB)	0 ± 1.6	2.6 ± 3.3	0.7 ± 2.9	-1.9 ± 4.3	0.1 ± 5.2	1.4 ± 8.5
Ice discharge	0.5 ± 0.5	2.1 ± 0.7	0.2 ± 0.5	-0.1 ± 0.4	-0.1 ± 1.1	2.5 ± 1.5

5.4.2. Seasonal mass variations

We analyze the mean annual cycles of total (GRACE) and cumulative SMB (RACMO2.3) mass anomalies over the period 2003–2013 (Fig. 5.11). To derive them, we divide the entire period into eleven overlapping 13-month time intervals, each starting in December of the previous year and ending in December of the current year. Then, the mean mass anomaly for each calendar month is estimated by linear regression, together with one bias parameter per time interval to account for long-term variability. This scheme is less sensitive to gaps in the data time-series than the plain averaging of mass anomalies per calendar month. The uncertainties of the mean mass anomalies

of GRACE are propagated from the error of each monthly GRACE estimate. The uncertainties of the cumulative SMB mean mass anomalies are computed by assuming 9% and 15% errors in the modeled mean mass anomalies due to precipitation and runoff, respectively. The uncertainties of the Total-SMB mass anomalies are the root-sum-square of the two noises in the GRACE and cumulative SMB estimates.

The mean annual cycles of total and cumulative SMB mass anomalies over Greenland show smooth month-to-month variations (Fig. 5.11). Importantly, the estimates of both types refer to the mean values for the months considered. The total mass from GRACE reaches its maximum in March and then steadily decreases until September. The most rapid mass loss is observed in July–August (~200 Gt). In contrast, the cumulative SMB decreases over a much shorter period—only from May to August.

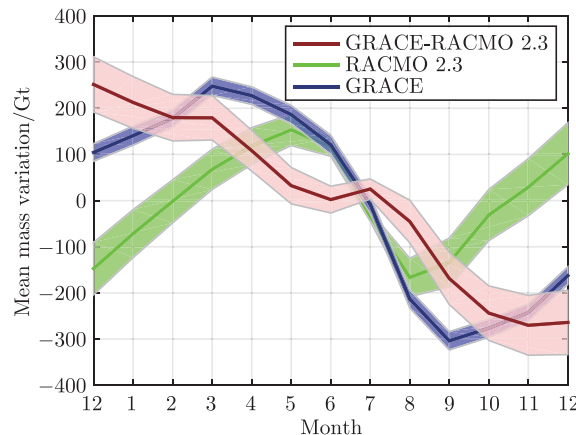


Figure 5.11 2003–2012 Greenland mean annual cycle of cumulative total mass anomalies from GRACE (darkblue), cumulative SMB anomalies from RACMO 2.3 (green) and their difference (red) for the period 2003–2012. The latter is used as a proxy for the cumulative sum of seasonal ice discharge variations and meltwater retention, subject to small GRACE error and SMB model bias. The shaded strips show the 2σ error bars. X-labels indicate the month of the year (Month 1 denotes January, month 12 is December).

We use the Total-SMB difference (see the brown line in Fig. 5.11) to evaluate the SMB modeling and to estimate non-SMB contributions to seasonal mass variations. Under the assumption of minor GRACE errors and SMB model biases, the Total-SMB represents the cumulative sum of ice discharge and meltwater storage. The Total-SMB shows three periods of nearly null variations (nearly flat segments in Fig. 5.11): February–March, May–July, and November–December. If we assume that the main contributor to the Total-SMB is ice discharge, these nearly flat cumulative variations would indicate that

the ice discharge is negligible or negative, which is unphysical. From the obtained error bars and a comparison of the Total-SMB from several different GRACE solutions (cf. Figs. B.1-B.5), we infer that the quasi-null Total-SMB variations during February–March and November–December are likely caused by noise in the estimates (see Appendix B). Therefore, they are not discussed below. On the other hand, the summer flat feature of May–July persists, no matter how the processing parameters are defined and which GRACE estimates are used. Therefore, we suggest that this feature is not triggered by noise in the estimates and must be attributed to a physical signal. Most likely, this signal is caused by meltwater retention.

According to RACMO2.3, most of the meltwater is produced between May and September, with a peak in July (cf. Fig. 5.12). On average, about 800 Gt of meltwater is produced in Greenland during the melt season, of which ~250 Gt is estimated to refreeze within the snowpack, and the rest is subject to runoff. However, RACMO2.3 does not take into account the time it takes for meltwater to run off. In late spring and early summer, this time is particularly long due to the inefficiency of the sub-glacial channel network (Rennermalm et al., 2013) and the replenishing of firn aquifers (mainly in the SE and NW) (Forster et al., 2014; Miège et al., 2016).

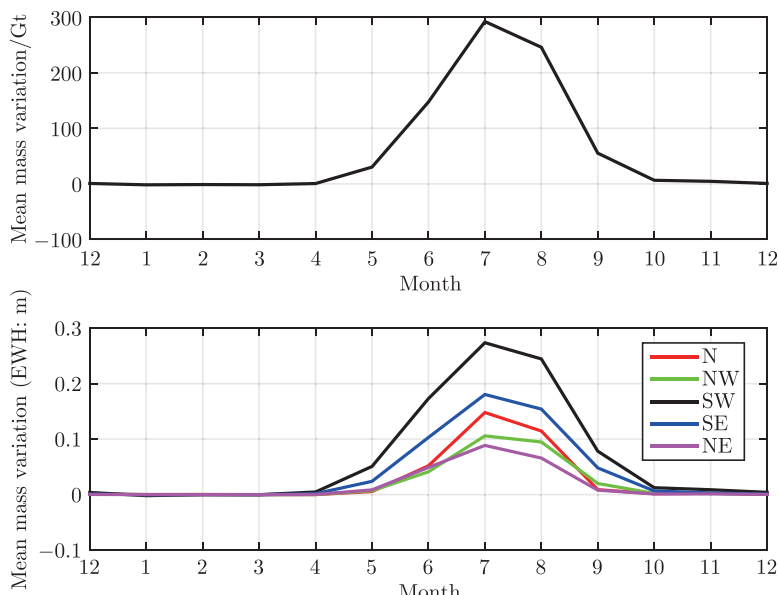


Figure 5.12 Mean monthly meltwater production (Gt) for all of Greenland (top) and individual drainage systems (in meters of Equivalent Water Height, bottom) simulated by RACMO 2.3.

In order to estimate the instantaneous amount of meltwater subject to runoff, we first fit the 11-year-mean Total-SMB residuals in two periods, before and after the flat feature (April-May and September–November), with a linear function. This function can be interpreted as an empirical estimate of the mean combined effect of ice discharge and the difference between the modeled and actual meltwater refreezing. Then, we force the mass budget to close at the beginning and the end of the melt season by subtracting the obtained linear function from the Total-SMB residuals (Fig. 5.13(a)). In this way, we find that meltwater is retained in Greenland between May and October, with a maximum of 100 ± 20 Gt in July.

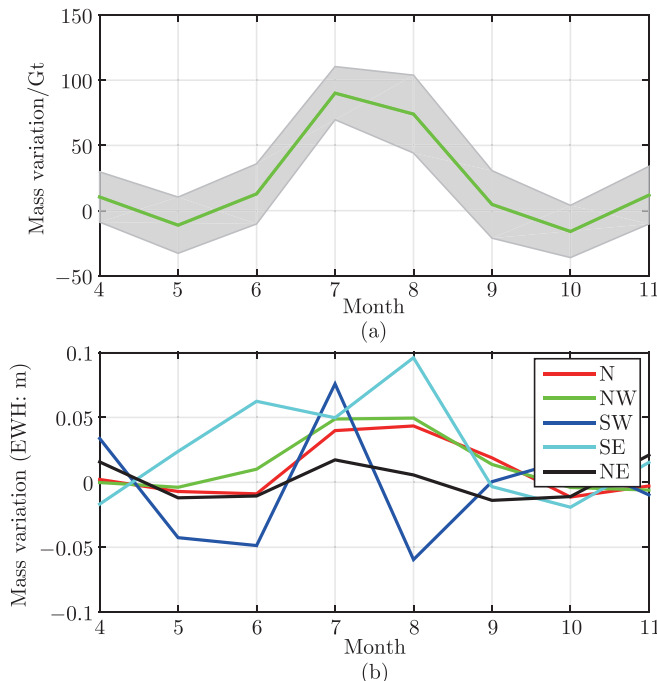


Figure 5.13 Estimates of seasonal meltwater storage, obtained as the monthly deviations from the April–May and September–November linear fit of “Total-SMB” (brown line in Fig. 5.11): for the whole GrIS (in Gt, top) and for individual drainage systems (in meters of Equivalent Water Height, bottom). Labels along the horizontal axis represent months between April (4) and November (11). The shaded strip in the top plot shows the 2σ error bar (the mean standard deviation is 23 Gt). The mean standard deviations of the estimates related for each drainage systems are: 0.02 m (N), 0.02 m (NW), 0.06 m (SW), 0.03 m (SE), and 0.01 m (NE); they are not shown in the plot for the sake of its readability.

One may argue that seasonal variations in non-SMB mass anomalies (our “Total-SMB”) may be caused not only by delayed meltwater runoff, but also by the variability in ice

discharge. An effort to quantify the contribution of the latter is made here. To this end, we use an independent dataset of sub-annually resolved glacier discharge for 55 glaciers, located mainly in the NW and SE DSSs. The sum of the estimates obtained for all 55 glaciers is shown in Fig. 5.14. One can see that at the whole-ice-sheet scale, the increase in ice discharge during the melt season is minor in all years (~10% or less). In the absence of complete coverage of the GrIS with observations of glacier velocities at the intra-annual time scale, we scale up the sum of the ice discharge estimates by a factor of ~2 to reach an agreement with the discharge over the entire GrIS in terms of the long-term linear trend (Enderlin et al., 2014). Similar to Fig. 5.13(a), we present the ice discharge related mean mass anomaly per calendar month in terms of the deviation from the linear function fitting the values in April–May and September–November (cf. Fig. 5.15). One can see that the effect of ice discharge is only a few Gt, i.e. its contribution to the total signal is negligible. This indicates that delayed runoff is the major contributor to the signal isolated in Fig. 5.13(a).

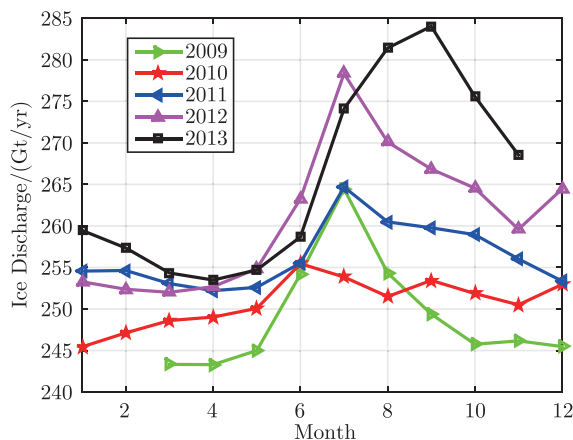


Figure 5.14 Monthly multi-regional ice discharge from 55 major marine-terminating glaciers of the NW and SE drainage systems. The unit is Gt/yr.

Next, we examine individual drainage systems (cf. Figs. 5.16–5.20). As was the case for Greenland as a whole, the Total-SMB flat features of February–March and November–December are not consistent across different GRACE processing methods, while the May–July feature is. This implies that seasonal meltwater retention also manifests itself at the scale of individual drainage systems. Regionally, the SE and NW show the largest meltwater accumulation per unit area (Fig. 5.13(b)). This is consistent with the fact that the rate of meltwater production is high in these sectors (see the bottom panel of Fig. 5.12), as is the retention potential due to high accumulation rates (Miège et al., 2016).

Given the later onset of the melt season, the NW and N regions store meltwater for a shorter period than the SE. In the NE region, the signal related to meltwater retention is less pronounced, which can be explained by the dry climate of this region, meaning that less pore space is available in the firn layer to store liquid water. For the SW region, we refrain from drawing any conclusions due to a relatively high level of noise in the estimates obtained. It is likely caused by a relatively small area of the region. In terms of the total mass, the largest meltwater accumulation takes place in the NW and SE regions: the contribution of each region can reach in July–August about 40 Gt (see Fig. 5.21). As for the increase in ice discharge during the melt season, we find that it is relatively minor for both NW and SE DSSs (less than 20% and 10%, respectively; see Figs. 5.22–5.23). Thus, the contribution of ice discharge to the signal reported in Fig. 5.21 is minor for both NW and SE DSSs: no more than 2.0 and 0.3 Gt, respectively (cf. Figs. 5.24–5.25). Interestingly, a much larger increase in ice discharge during the melt season is found for the single major contributor to ice discharge, the Jakobshavn glacier: up to 60% in 2012 (Fig. 5.26).

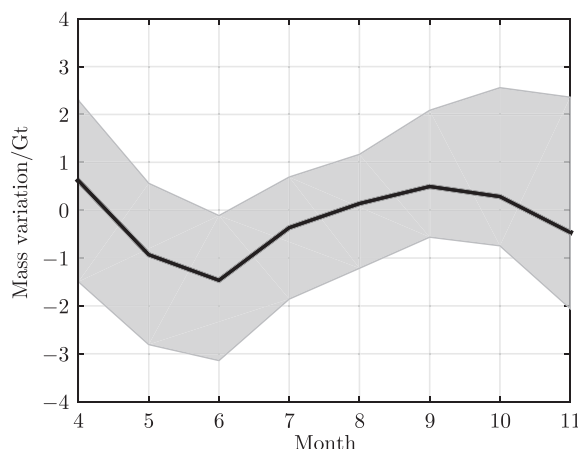


Figure 5.15 Similar to Fig. 5.13, but the cumulative mean ice discharge related mass anomalies over 2009–2013, based on seasonal estimates of ice discharge from 55 major marine-terminating glaciers and upscaled to represent all of Greenland.

Finally, we note that the Total-SMB residuals can also be used to diagnose SMB model bias in the winter months. Due to negligible surface melt during this time of the year, an unphysical increase in the cumulative Total-SMB would indicate insufficient snow accumulation. Our results suggest this for the N and NE regions (Figs. 5.16 and 5.20).

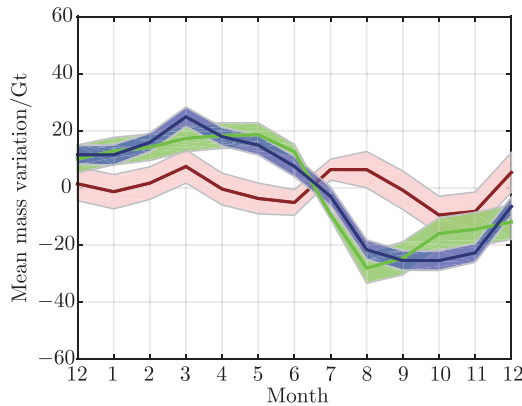


Figure 5.16 Monthly cumulative total (blue), surface (green) and residual “Total-SMB” (red) mass variations (see legend of Fig. 5.11), for drainage systems: N.

5

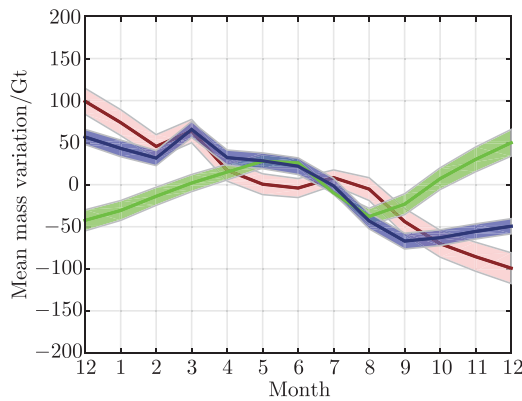


Figure 5.17 Same as Fig. 5.16, but for drainage system: NW.

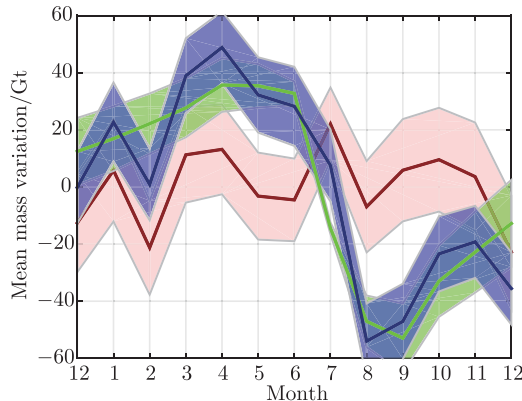


Figure 5.18 Same as Fig. 5.16, but for drainage system: SW.

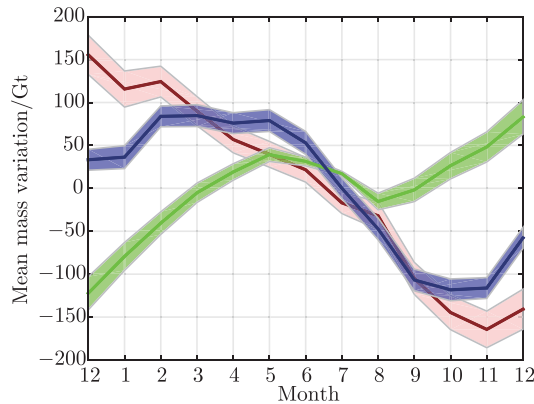


Figure 5.19 Same as Fig. 5.16, but for drainage system: SE.

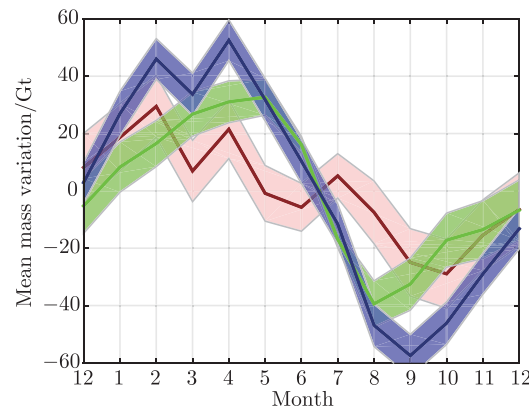


Figure 5.20 Same as Fig. 5.16, but for drainage system: NE.

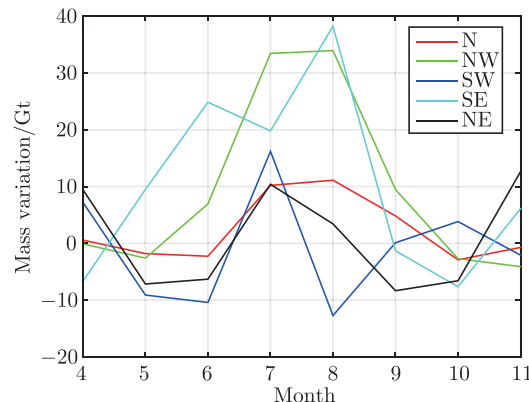


Figure 5.21 Same as Fig. 5.13, bottom panel, but in terms of mass variation (Gt).

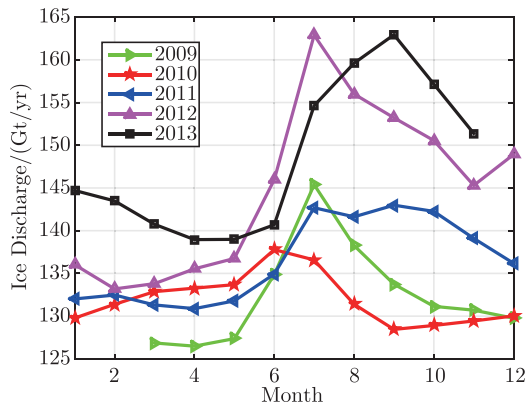


Figure 5.22 Similar to Fig. 5.14, but for the NW drainage system.

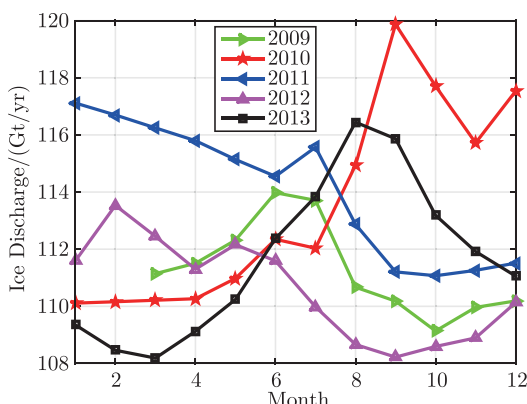


Figure 5.23 Similar to Fig. 5.14, but for the SE drainage system.

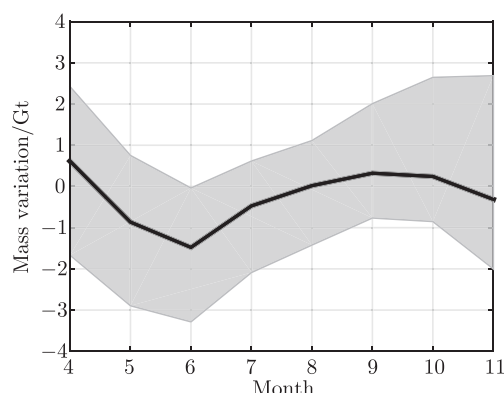


Figure 5.24 Similar to Fig. 5.15, but the glaciers in NW.

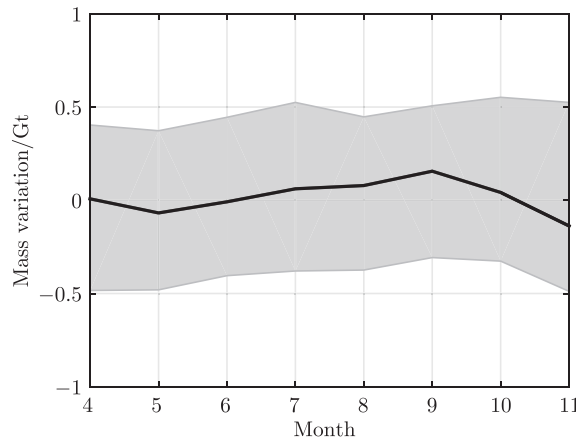


Figure 5.25 Similar to Fig. 5.15, but for the glaciers in SE.

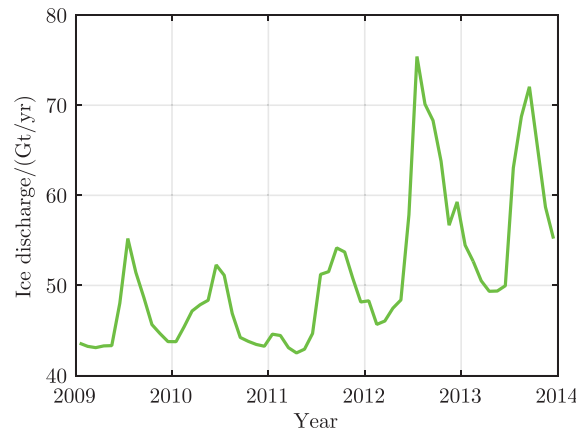


Figure 5.26 Monthly variations of ice discharge from Jakobshavn glacier over the period 2009–2013 (Gt/yr).

5.5. Summary

GRACE CRS RL05 monthly solutions, processed with a variant of the mascon approach, have been applied to systematically analyze the mass budget of the GrIS on various temporal and spatial scales. The obtained estimate of the mean rate of mass loss is 277 ± 21 Gt/yr for the period 2003–2012. The rate of SMB accumulation modeled by RACMO2.3 is 231 ± 122 Gt/yr. The difference between these trends is -508 ± 124 Gt/yr, which is consistent with the 2003–2012 ice discharge observations by Enderlin et al. (2014): 520 ± 31 Gt/yr. Moreover, we observe relatively large discrepancies between the estimates for the SE and N DSs. These discrepancies imply that the adopted climate model likely

overestimates precipitation in the SE DS and underestimates it in the N DS.

Our estimates of the accelerations in SMB-related ($-29.7 \pm 2.7 \text{ Gt/yr}^2$), ice discharge-related ($2.5 \pm 1.5 \text{ Gt/yr}^2$), and total ($-31.1 \pm 8.1 \text{ Gt/yr}^2$) mass anomalies are consistent: the residual does not exceed 1 Gt/yr^2 , which is well within the error bar. This is consistent with Velicogna et al. (2014), who also found that most of the mass loss acceleration can be explained by the contribution of SMB. Furthermore, our results indicate that most of the total mass acceleration observed by GRACE is due to the SW and NW DSs, which is in agreement with Sasgen et al. (2010) and Velicogna et al. (2014).

We found a remarkable seasonal cycle in the difference between non-detrended monthly total and cumulative SMB mass anomalies (“Total-SMB”), which likely reflects significant meltwater retention during the summer months. The peak of cumulative storage is $100 \pm 20 \text{ Gt}$ at the end of July, when monthly totals are used. To estimate the potential contribution of ice discharge to the observed signals, we used the estimates of ice discharge over 55 outlet glaciers obtained with the flux gate method. We showed that this contribution remains at the level of only a few Gt, i.e. plays a negligible role. We also analyzed this process per drainage system. We demonstrated that the processes of meltwater accumulation and runoff are particularly weak in the northeastern part of Greenland.

This study also suggests that the Total-SMB residuals can be used to verify SMB estimates from climate models by applying the simple constraint that this residual cannot be negative in winter months, when it predominantly reflects ice discharge. In this way, we found that the adopted climate model likely underestimates the precipitation in the N and NE DSs in winter months. This precipitation deficiency in RACMO2.3 was independently confirmed by a comparison with ice discharge in this region by Mouginot et al. (2015).

At the same time, a comparison of the seasonal variations in the “Total-SMB” estimates derived from GRACE data in different ways revealed noticeable discrepancies, particularly in winter months. This indicates that further work is needed to ensure the robustness of GRACE-based estimates.

6

Analysis and mitigation of biases in Greenland Ice Sheet mass balance trend estimates from GRACE mascon products

6.1. Introduction

The Gravity Recovery and Climate Experiment (GRACE) satellite mission, launched in 2002, provided estimates of mass anomalies at the global and regional scales through June 2017 (see e.g., Tapley et al., 2004, 2019). These estimates have become one of the most valuable data sources being used to understand mass transport in the Earth system. Several research areas benefit from this information, including hydrology (see e.g., Wahr et al., 1998; Rodell et al., 2004; Schmidt et al., 2006; Syed et al., 2008; Ramillien et al., 2008; Landerer and Swenson, 2012; Scanlon et al., 2016), cryosphere studies (see e.g., Velicogna and Wahr, 2006; Chen et al., 2006; Van den Broeke et al., 2009; Wouters et al., 2008; Shepherd et al., 2012; Luthcke et al., 2013; Siemes et al., 2013; Schrama et al., 2014; Velicogna et al., 2014, 2020; Ran et al., 2018a), and physics of the solid Earth (see e.g., Han et al., 2006; Chen et al., 2007; Panet et al., 2007; Heki and Matsuo, 2010; Sun et al., 2009; Wang et al., 2012).

The GRACE-based mascon solutions offered by the Jet Propulsion Laboratory (JPL RL06 v01) (Watkins et al., 2015), the Goddard Space Flight Center (GSFC v2.4) (see e.g., Rowlands et al., 2005; Luthcke et al., 2013), and the Center for Space Research (CSR RL06 v01) at the University of Texas at Austin (Save et al., 2016), are widely used. Compared to spherical harmonic solutions, they provide less signal leakage and a higher spatial resolution (Scanlon et al., 2016). The JPL mascon solutions used $3^\circ \times 3^\circ$ mascons, whereas the CSR and GSFC mascon solutions used equal-area mascons with a size of $1^\circ \times 1^\circ$ at the equator. Spatial and temporal constraints were used to compute the mascon solutions. For example, GSFC used an exponential function describing correlations in time and space between mascon pairs (Luthcke et al., 2013), JPL used temporal and spatial constraints, which were extracted from geophysical and hydrological models

(Watkins et al., 2015), and CSR used a temporally and spatially variable zero-order Tikhonov regularization, which implies no correlations in the space and time domains (Save et al., 2016). From a mathematical point of view, all constraints can be considered as special variants of the Tikhonov regularization (see e.g., Tikhonov, 1963a,b).

Overall, the mascon products from CSR, GSFC, and JPL show a good performance in observing the mass balance rates over the entire GrIS (Ran et al., 2018a). However, there are significant differences at the drainage system scale. For example, Fig. 6.1 shows the mass anomaly time-series for five different drainage systems of the GrIS. To avoid splitting individual mascons, each drainage system includes an integer number of JPL mascons, because they have the largest size (i.e., $3^\circ \times 3^\circ$), as compared with other mascon products ($1^\circ \times 1^\circ$ for CSR and GSFC). Fig. 6.1 shows large temporal and spatial discrepancies between the mascon solutions of the three analysis centers. For example, the discrepancies between the mass anomalies accumulated from 2003 to 2014 range from 100 to 200 Gt, depending on the drainage system. In the southwestern drainage system, the estimated mass balance rate for the years 2003–2006 is 7, 9, and -28 Gt/yr for CSR, JPL, and GSFC products, respectively.

6

In this chapter, we systematically investigate the discrepancies between different mascon products over the GrIS, following Ran et al. (2021). We analyze the causes of these discrepancies by reproducing the different behavior of mass anomaly time-series using the variant of the mascon approach by (see e.g., Ran et al., 2018a,b). Furthermore, we demonstrate that the quality of mascon-based estimates can be increased by appropriately modifying the applied spatial constraints. The main assumption behind the improved spatial constraints used in this book is that there are no correlations between mascons belonging to different drainage systems. This assumption is driven by the fact that there is a negligible mass exchange between neighboring drainage systems, which implies that the behavior of mass anomalies in neighboring drainage systems may be very different. The assumption of no correlations between mascons belonging to different drainage systems may reduce signal leakage. A similar idea was already considered in (Sabaka et al., 2010) and (Luthcke et al., 2013), where Greenland was divided into two regions separated by the 2000 m elevation line. They assumed the absence of correlations between mass variations in the two regions. However, these constraints did not facilitate a reduction of signal leakage between neighboring drainage systems.

This chapter is organized as follows. In Sect. 6.2, we present the methodology, including the mascon approach adopted and the improved spatial constraints. The data used in

this book are presented in Sect. 6.3. In Sect. 6.4, the discrepancies between the CSR, JPL, and GSFC mascon products and the results obtained with the improved spatial constraints are quantified and analyzed. The discussion and conclusions are left to Sect. 6.5 and 6.6, respectively.

6.2. Methods

To analyze the mass anomaly time series from the CSR, GSFC, and JPL mascon products, we compare them to the mass anomalies based on the variant of the mascon approach proposed in (see e.g., Ran et al., 2018a,b,c). This approach is summarized in Sect. 6.2.1. Furthermore, we consider the mass anomaly estimates obtained with improved spatial constraints in Sect. 6.2.2.

6.2.1. Variant of the mascon approach adopted to estimate mass anomalies

The mascon approach of (Ran et al., 2018a) is an extension of the techniques proposed by (Forsberg and Reeh, 2007), and (Baur and Sneeuw, 2011). Like many other post-processing schemes developed so far (see e.g., Wouters et al., 2008; Sasgen et al., 2010; Schrama and Wouters, 2011; Jacob et al., 2012; Bonin and Chambers, 2013), it uses GRACE Level-2 spherical harmonic solutions as a starting point instead of GRACE Level-1B data, as used in the mascon solutions from GSFC (Luthcke et al., 2013), CSR (Save et al., 2016), and JPL (Watkins et al., 2015). The computations start by synthesizing “pseudo-observations”—gravity disturbances at an average satellite altitude—from the monthly set of spherical harmonic coefficients (SHCs). The unknown parameters (surface density variations in kg/m^2 per mascon) are then estimated using weighted least-squares techniques. The solution is stabilized using first-order Tikhonov regularization. Finally, the estimated surface densities are converted into mass anomalies in units of Gt for visualization purposes (e.g., Fig. 6.1). Note that, in contrast to (Forsberg and Reeh, 2007), and (Baur and Sneeuw, 2011), the full noise covariance matrices of the monthly SHCs are propagated into the pseudo-observations using the law of covariance propagation, and used as the inverse weight matrix in the weighted least-squares approach. Moreover, the columns of the design matrix are low-pass filtered to make them spectrally consistent with the spatial resolution of the monthly spherical harmonic models.

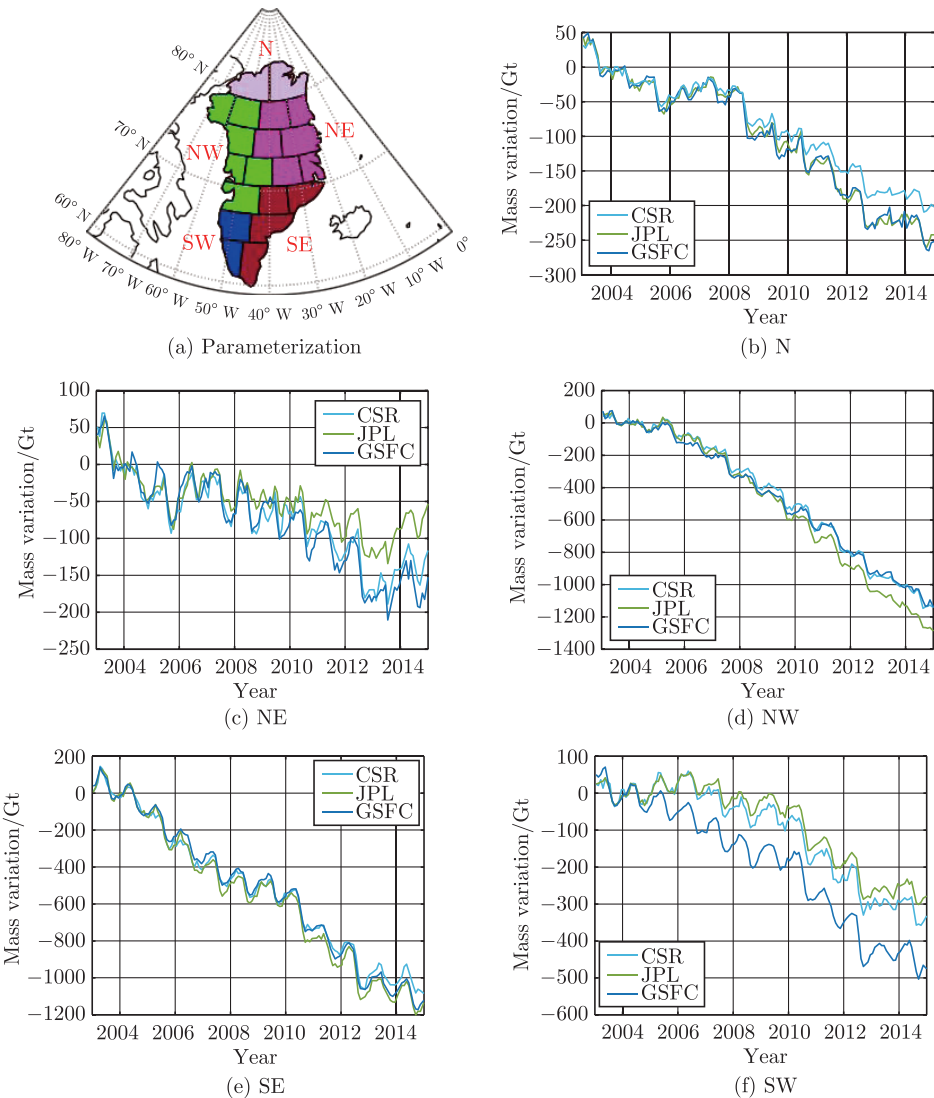


Figure 6.1 (a): The geometry of the drainage systems, aggregated from the JPL mascons. (b)-(f): Mass anomaly time-series for five GrIS drainage systems from CSR, JPL, and GSFC mascon-solutions.

6.2.2. Adopted spatial constraints

To suppress the amplification of data noise when computing the mascon surface densities, the Tikhonov regularization (see e.g., Tikhonov, 1963a,b) is used. The regularized

least-squares solution is then given as

$$\hat{\mathbf{x}} = \arg \min_{\mathbf{x}} [(\mathbf{d} - \mathbf{Ax})^T \mathbf{C}_d^{-1} (\mathbf{d} - \mathbf{Ax}) + \alpha \Phi(\mathbf{x})] \quad (6.1)$$

where $\Phi(\mathbf{x})$ is the Tikhonov regularization functional and α is the regularization parameter. The solution of Eq. (6.1) can be written as

$$\hat{\mathbf{x}} = (\mathbf{A}^T \mathbf{C}_d^{-1} \mathbf{A} + \alpha \mathbf{R}')^{-1} \mathbf{A}^T \mathbf{C}_d^{-1} \mathbf{d} \quad (6.2)$$

where \mathbf{A} is the design matrix, \mathbf{d} is the vector of pseudo observations, \mathbf{C}_d is the noise covariance matrix of \mathbf{d} , and \mathbf{R}' is the regularization matrix associated with the minimization functional $\Phi(\mathbf{x})$. There are different choices of $\Phi(\mathbf{x})$ (see Text C.1). For example, the zero-order Tikhonov regularization minimizes the L2-norm of the surface density function, whereas the first-order Tikhonov regularization minimizes the L2-norm of this gradient of this function. For the present application, we prefer to use the first-order Tikhonov regularization because zero-order Tikhonov regularization can greatly damp long-term trends and other strong signals (Ran et al., 2018a).

The implementation of the first-order Tikhonov spatial constraints depends on the panelization of the GrIS with mascons and is similar to that of (Ran et al., 2018a) and (Watkins et al., 2015). The area of the GrIS is covered by non-overlapping mascons, which are defined in two steps. First, the GrIS is divided into latitudinal bands. Second, each latitudinal band is subdivided into mascons along meridians to obtain mascons of similar areas. As shown in Fig. 6.1(a), the mascons do not form an equal-angular grid. This makes the implementation of the ordinary first-order Tikhonov regularization more intricate. To explain the implementation, we consider seven mascons labeled h, i, j, k, l, m , and n (see Fig. 6.2(a)) and denote the corresponding surface mass densities as $x_h, x_i, x_j, x_k, x_h, x_i, x_k, x_l$, and x_n . To minimize the north-south component of the horizontal gradient, the mascons with indices h, i, k, m , and n , must be formally divided into sub-mascons (cf. Fig. 6.2(b)). The sub-mascons share the same surface density with the parent mascon, and serve only to implement the spatial constraint associated with the first-order Tikhonov regularization. For example, $x_k = x_{k^1} = x_{k^2} = x_{k^3} = x_{k^4}$. Therefore, the minimization condition involving mascon k shown in Fig. 6.2(a) can be written, in accordance with Eq. C.4, as:

$$\begin{aligned} \Phi_1(x) &= \sum_k [\underbrace{f_{h^2 k^3} (x_{h^2} - x_{k^3})^2 + f_{i^1 k^4} (x_{i^1} - x_{k^4})^2 + f_{k^1 m^2} (x_{k^1} - x_{m^2})^2}_{\text{North-south direction}} \\ &\quad + \underbrace{f_{k^2 n^1} (x_{k^2} - x_{n^1})^2 + f_{j k} (x_j - x_k)^2 + f_{k l} (x_k - x_l)^2}_{\text{North-south direction}}] \\ &\quad + \underbrace{f_{k^1 m^2} (x_{k^1} - x_{m^2})^2}_{\text{East-west direction}} \\ &= \sum_k \sum_{k'} R_{kk'} x_k x_{k'} = \mathbf{x}^T \mathbf{R} \mathbf{x} \end{aligned} \quad (6.3)$$

$\frac{area_j + area_k}{\frac{2}{d_{jk}^2}}$, where d_{jk} is the distance between the centers of mascons j and k ; where $area_j$ and $area_k$ are the areas of mascon j and k , respectively. The non-zero elements of the first-order Tikhonov regularization matrix associated with the k -th mascon are given in Table 6.1. Note that all the non-zero off-diagonal elements correspond to the neighbors of the k -th mascons (i.e., the mascons that share a common side with the k -th mascon).

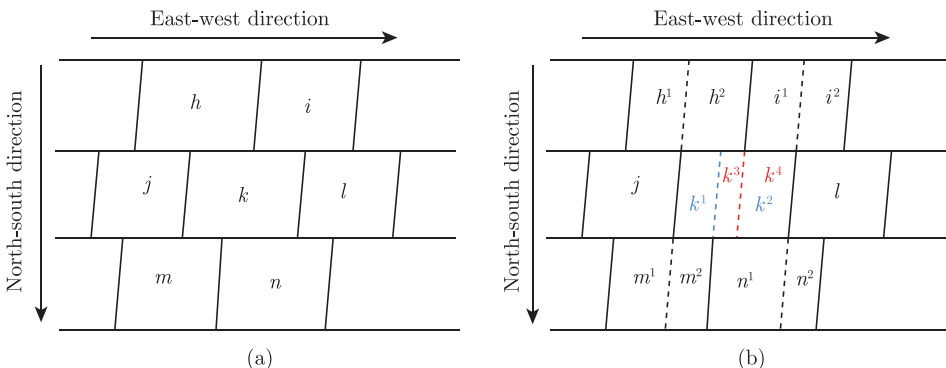


Figure 6.2 (a) Schematic mascon distribution in the inner part of Greenland, and (b) division of mascons into sub-mascons to compute the elements of the first-order Tikhonov regularization matrix. h, i, j, l, m , and n are the indexes of the mascons that are neighbors of mascon k . Based on the boundaries of neighboring mascons, mascon k is virtually divided into k^1 , and k^2 , or k^3 and k^4 . Similar divisions are also applied to the neighboring mascons h, i, m and n .

Table 6.1 First-order Tikhonov regularization matrix elements associated with the k -th mascon and its neighbors (cf. Fig. 6.2)

patch ID		h	i	j	k	l	m	n	...
...
h	...				$-f_{h^2 k^3}$...
i	...				$-f_{i^1 k^4}$...
j	...				$-f_{j k}$...
k	...	$-f_{h^2 k^3}$	$-f_{i^1 k^4}$	$-f_{j k}$	$f_{h^2 k^3} + f_{i^1 k^4} + f_{k^1 m^2}$ $+ f_{k^2 n^1} + f_{j k} + f_{k l}$	$-f_{k l}$	$-f_{k^1 m^2}$	$-f_{k^2 n^1}$...
l	...				$-f_{k l}$...
m	...				$-f_{k^1 m^2}$...
n	...				$-f_{k^2 n^1}$...
...

The general expression for the elements R_{ki} can be written as follows:

$$R_{ki} = \begin{cases} -f_{k'i'} & \text{if } k \neq i, k \text{ has a common side with } i \\ \sum_j f_{k'i'} & \text{if } k=i \\ 0 & \text{otherwise} \end{cases} \quad (6.4)$$

where i' is the part of the i -th mascon that shares the border with mascon k , whereas k' is the part of mascon k which shares the border with mascon i . Summation index j runs over the neighbors of the k -th mascon (again, the “prime” symbol indicates the mascon parts in a given pair that have a common border). It should be emphasized that the sub-mascons are introduced only “virtually” (i.e., each mass anomaly is estimated as a single number for the whole mascon; mass anomalies in kg/m² are the same for all the sub-mascons within a given mascon).

So far, we considered the “ordinary” first-order Tikhonov regularization, which covers all pairs of neighboring mascons. As far as the improved spatial constraint is concerned, the main assumption behind it is that there is no correlation between mascons belonging to different drainage systems. This is implemented as an update of the regularization matrix \mathbf{R} of Eq. C.4. This update considers pairs of mascons as neighbors only if they belong to the same drainage system. Thus, correlations between pairs of mascons belonging to different drainage systems are set equal to zero, which reduces signal leakage between the corresponding mascons.

6.3. Data

6.3.1. GRACE

As input, we use the CSR Release 6 (RL06) GRACE SHC solutions, which are complete to degree 96 and provided with full noise covariance matrices. The time interval considered in this book covers the years from 2003 to 2014. Since no sets of SHCs are provided for 15 months, the dataset consists of 141 monthly solutions. The monthly $C_{2,0}$ coefficients are replaced by SLR-based ones (Loomis et al., 2020). The missing degree-one coefficients are taken from (Sun et al., 2016b). Therefore, noise correlations between the degree-1 coefficients and the $C_{2,0}$ coefficients on the one hand and all other coefficients on the other hand are assumed to be zero. The glacial isostatic adjustment is corrected for using the model from (Peltier et al., 2014), which was also used to compute the mascon solutions of CSR RL06, JPL RL06, and GSFC v2.4.

6.3.2. RACMO2.3

To validate GRACE-based estimates of mass variations, we use RACMO2.3, a regional atmospheric climate model developed by the Royal Netherlands Meteorological Institute (KNMI) and the Institute for Marine and Atmospheric Research (IMAU) at Utrecht University (Noël et al., 2015). More specifically, we use Surface Mass Balance (SMB) estimates over 11-by-11 km blocks with daily temporal resolution. The daily SMB estimates are time-integrated to yield cumulative SMB mass anomalies, and averaging yields mean monthly mass anomalies.

6.4. Results

6.4.1. Understanding the discrepancies between the CSR, JPL and GSFC mascon products

Figs. 6.3 and C.2 show the GrIS mass variations per drainage system from the CSR, JPL, and GSFC mascon solutions. Though differences are relatively small at the beginning of the period, they increase monotonically as a function of time, reaching several hundred of Gt at the end of the period. To understand the source of these discrepancies, we compute different sets of mascon-type estimates (referred as “TUD-SUSTech” in this book) using the mascon approach of (Ran et al., 2018a) in combination with the ordinary first-order Tikhonov regularization of Eq. 4. The differences between the TUD-SUSTech solutions on the one hand, and the CSR, JPL, and GSFC solutions on the other hand, depend on the choice of the regularization parameter of the TUD-SUSTech solution (cf. Figs. 6.3 and C.2). In general, we find that by changing the regularization parameter of the TuD-SUSTech mascon solutions, we can mimic the mascon solutions from CSR, JPL, and GSFC reasonably well. This is done per drainage system.

Fig. 6.4 shows, for each drainage system, the RMS difference between the JPL, CSR, and GSFC solutions and the TUD-SUSTech solutions as a function of the regularization parameter for the latter solution. The smallest RMS difference is about 20 Gt. Depending on the solution and the drainage system, the minimum RMS difference is obtained for different regularization parameters.

In the SW drainage system (see Figs. 6.3 and 6.4), the regularization parameters which provide the closest fit to the solutions of the analysis center solutions are 3×10^{-26} (JPL),

1×10^{-25} (CSR), and 1×10^{-24} (GSFC). The TUD-SUSTech solution without regularization shows a clear mass gain signal over the period 2004–2006, and provides the smallest mass loss trend over the entire period. The mass gain over the period 2004–2006 becomes smaller with increasing regularization parameter and turns into a mass loss signal when the regularization parameter is large enough. We explain this behavior by signal leakage from the neighboring NW and SE drainage systems, which show large mass losses.

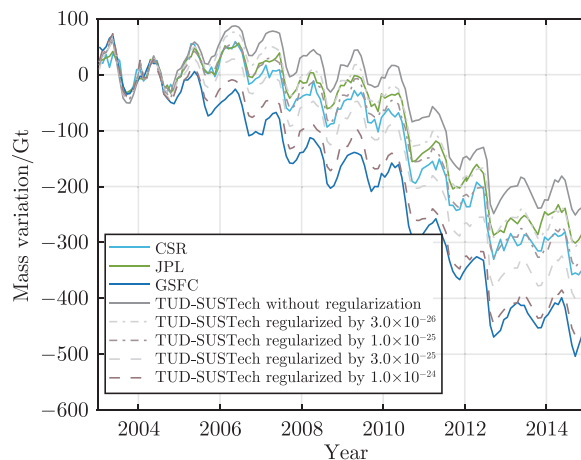


Figure 6.3 Mass anomaly time-series for the SW drainage system based on the mascon products from CSR, JPL and GSFC, as well as TUD-SUSTech mascon solutions produced with different regularization parameters (from 0 to 10^{-24}). For other drainage systems, please see Fig. C.2.

For the NW drainage system (see Figs. 6.4 and C.2), a regularization parameter of 3×10^{-26} gives the smallest RMS difference to the JPL solutions: of about 20 Gt. A similar fit to the CSR solutions is obtained with a significantly larger regularization parameter of 3×10^{-25} . The latter value of the regularization parameter also provides the best fit to the GSFC solutions, although the RMS difference is 30 Gt, i.e., about 50% larger. For the SE drainage system (see Figs. 6.4 and C.2), the best fit of the TUD-SUSTech solutions to the analysis centers' solutions is obtained for a regularization parameter of 1×10^{-25} (JPL) and 3×10^{-25} (CSR and GSFC), respectively.

In the NE drainage system (see Figs. 6.4 and C.2), the dependence of the estimated mass variations on the regularization parameter shows a more complicated behavior. As the regularization parameter increases, the mass loss trend first becomes smaller, but increases starting from a regularization parameter of 3×10^{-26} . Minimum RMS differences are obtained by choosing regularization parameters of 3×10^{-25} (JPL, CSR) and 1×10^{-24} (GSFC).

In the N drainage system (see Figs. 6.4 and C.2), no regularization applied to the TUD-SUSTech solution provides the best fit to the JPL and GSFC solutions, whereas a minor regularization of 3×10^{-26} is required to obtain the best possible fit to the CSR solutions.

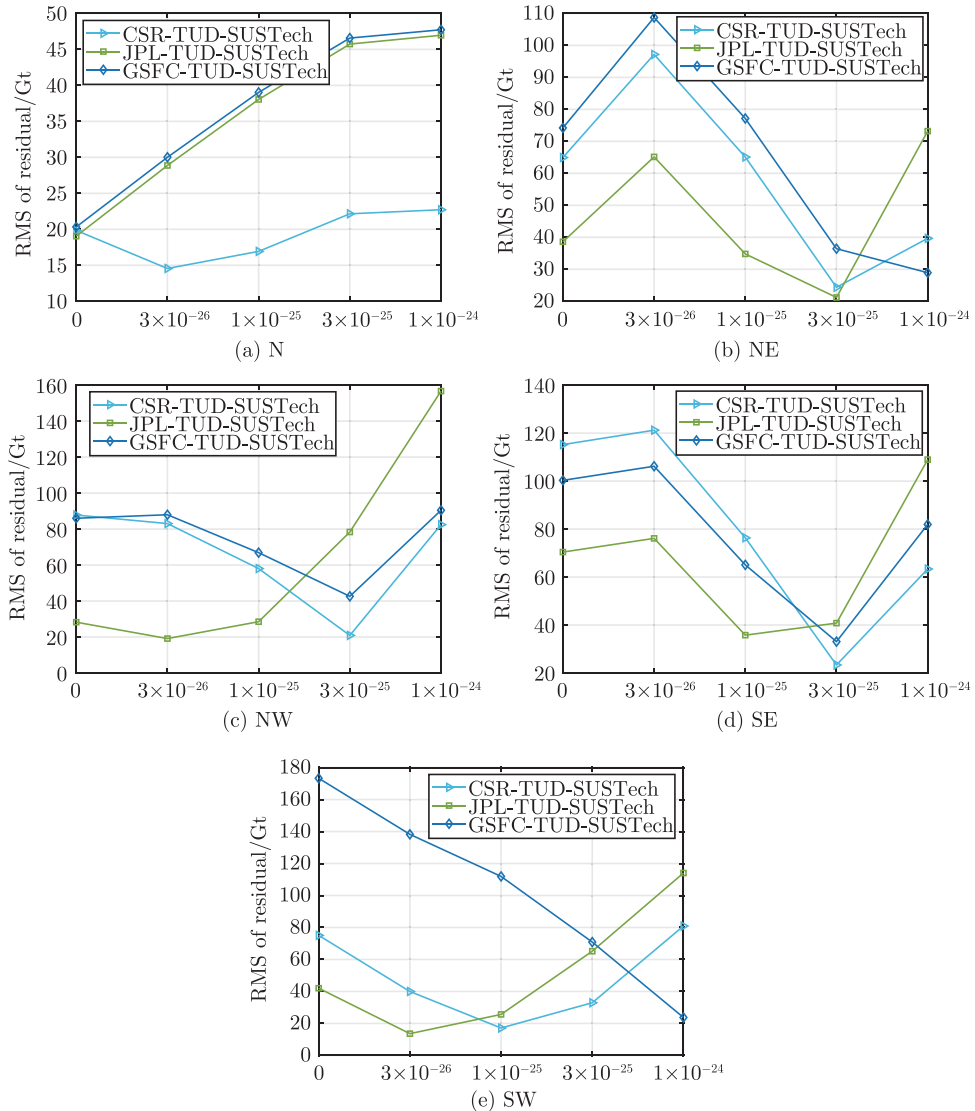


Figure 6.4 RMS differences between the official (CSR, JPL and GSFC) monthly solutions and the TUD-SUSTech monthly solutions as functions of the regularization parameter of the TuD-SUSTech solutions.

Overall, the analysis shows that the regularization has a significant impact on the estimated mass anomalies. The fit of the TUD-SUSTech solutions to the solutions from CSR, JPL, and GSFC can be optimized by choosing an appropriate regularization parameter when computing the TUD-SUSTech solutions (see Figs. 6.3 and 6.4). To obtain the smallest RMS difference to the JPL solutions, the least regularization is needed in most cases, whereas a somehow larger amount of regularization is needed to obtain the smallest RMS fit to the CSR and GSFC solutions.

6.4.2. Numerical study to analyze regularization-driven biases in mascon-type estimates

The results of Sect. 6.4.1 indicate that the applied regularization is one of the contributors to the observed discrepancies between the CSR, JPL, and GSFC mascon solutions. To further investigate the impact of the regularization, we have performed two numerical experiments.

In the first experiment, mass anomaly time series were calculated from a combination of ICESat and RACMO 2.3 data using the approach of (see e.g., Ran et al., 2018a,b). The 20-by-20 km ICESat-based trends were taken from (Felikson et al., 2017) and upscaled by a factor of 2.3 to match the trend magnitudes from the 2004–2014 GRACE data. The 11-by-11 km RACMO 2.3 SMB data, available with a temporal resolution of 1 day, were resampled to the 20-by-20 km ICESat cells, integrated in time, and time-averaged to provide monthly SMB-related mass anomaly time-series. Then, these time-series were de-trended, added to the ICESat trends and spatially integrated to provide monthly mass anomalies per mascon. The mascon definition of JPL was used (cf. Fig. 6.1(a)). The resulting monthly mass anomaly time series per mascon serve as the true signal. From this signal, pseudo-observations were generated and inverted into monthly mass anomalies using the TUD-SUSTech mascon approach. To investigate the bias caused by the regularization, two scenarios were considered that differ in the choice of the regularization parameter. One scenario uses a regularization parameter of 10^{-25} . This value appeared to be the optimal one according to the L-curve method when inverting monthly GRACE level-2 data into mass anomalies. The second one was set equal to 10^{-24} ; this regularization parameter sometimes appeared to be the one which provided the smallest difference between the TUD-SUSTech solutions and the solutions of the GRACE analysis centers (cf. Sect. 6.4.1).

We investigated the bias in trends caused by signal leakage from a particular drainage

system into another. Several runs were completed for this purpose. In each run, the mass anomalies over all drainage systems except the one under consideration were assumed to be zero. In real data processing, estimating the bias triggered by a regularization is problematic. Therefore, to facilitate a comparison with the results of real data processing, we focus below on the differences in bias between the two choices of regularization parameters (referred to in this book as the relative bias). The obtained results are shown in Fig. 6.5 and Tables C1–C6.

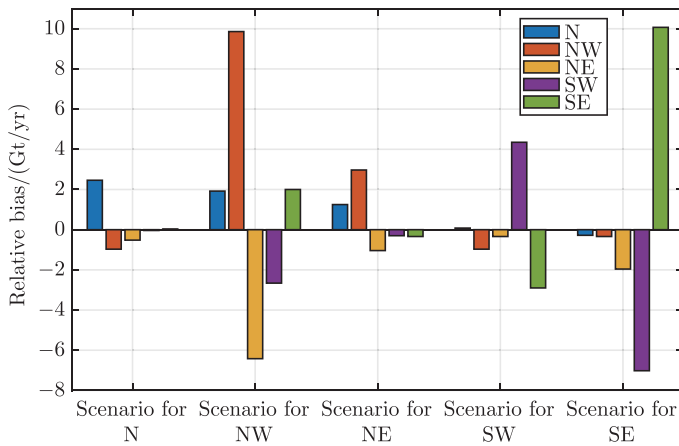


Figure 6.5 Analysis of relative biases due to signal leakage from one drainage system to the others due to regularization. Note that for every scenario considered, the mass change signal is confined to the drainage system, whereas no mass change is assumed in all other drainage systems. The relative bias is the difference between the solutions computed with regularization parameters of 10^{-25} and 10^{-24} , respectively.

Table C1 shows the result for the NW drainage system, which has the largest (negative) trend of -148 Gt/yr. It turns out that the bias is negligible (about 1%) for a regularization parameter of 10^{-25} , but increases to about 8% when a regularization parameter of 10^{-24} is chosen. The signal from the NW drainage system mostly leaks into the neighboring NE drainage system, while the leakage to the other drainage systems is a smaller by factor of 2–3. This relative bias is maximum in the NW drainage system itself (-9.9 Gt/yr) followed by the NE drainage system (6.4 Gt/yr). The relative biases in the other drainage systems are much smaller.

The results for the other drainage systems are shown in Fig. 6.5 and Tables C2–C5. In summary, the signal from the SW drainage system leaks mainly to the SE, whereas there is a negligible leakage to NW, N, and NE. The signal from the SE drainage system mostly leaks to the SW; relative biases in NE and N are small. Signal from NE leaks mostly to

NW. Leakage from N is small and mostly goes to NW. Thus, the signal mostly leaks into the eastern/western neighbor of the current drainage system. This is consistent with the well-known fact that the spatial resolution of GRACE in the east-west direction is worse than that in the north-south direction.

The relative biases computed in the simulation experiment can be easily compared to the relative biases in real data solutions. To do this, we computed the relative bias per drainage system caused by signal leakage from all other drainage systems. We did this by summing up the relative biases shown in Tables C1–C5 (cf. the fourth row in Table 6.2). The relative biases obtained in the real data processing are shown in the third row of Table 6.2. The latter were calculated directly as the difference between the solutions with regularization parameters 10^{-25} and 10^{-24} , respectively. We find a reasonable agreement between the relative biases observed in the simulations and in the real data processing. For most drainage systems, the relative bias observed in the simulations can explain 50% to 70% of the relative bias in the real data case. Furthermore, the signs of the relative biases are consistent for all drainage systems. The remaining discrepancies between the simulations and the real data case are likely caused by the combined effect of noise in the real data (manifested as north-south stripes), parameterization (i.e., model) errors, and leakage of signal from outside Greenland.

Table 6.2 The trend estimates and relative biases observed in the real data processing and in the numerical simulations based on noise-free data. The units are Gt/yr

text	N	NW	NE	SW	SE
Trend recovered with $\alpha = 10^{-25}$ (real data)	-11.24	-119.99	-3.28	-29.36	-101.99
Trend recovered with $\alpha = 10^{-24}$ (real data)	-10.94	-97.86	-17.49	-40.08	-84.81
Relative bias (real data)	0.29	22.13	-14.21	-10.72	17.18
Total relative bias (simulations)	5.43	10.55	-10.29	-5.67	8.86

To support the previous statement, we performed a second numerical experiment, in which the pseudo-observations in the ICESat/RACMO simulation were contaminated with realistic errors from various sources: parameterization errors, random noise, errors in the Atmosphere and Ocean De-aliasing model, and leakage of signals from outside Greenland. For details on how these errors were calculated, we refer to (see e.g., Ran et al., 2018a,b).

As shown in Table 6.3, the relative biases in the scenario when noisy data are considered

match the relative biases in the real data case even better than before, except for the N drainage system. In the NW, SW, and SE drainage systems, the relative bias observed in the simulations now explains 60% to 80% of the relative bias in the real data case. In the NE, the difference in relative biases between the simulation and real data is only 6%. The large difference in the N may be caused by signal leakage from the Canadian Arctic in the simulations.

Table 6.3 The trends estimates and relative biases obtained for regularization parameters 10^{-25} and 10^{-24} in the simulation where noisy data are considered. Note that an ordinary first-order Tikhonov regularization is applied in this book. The units are Gt/yr

	N	NW	NE	SW	SE
Trend recovered with $\alpha = 10^{-25}$ (simulation)	-20.30	-155.20	35.66	-15.76	-118.01
Trend recovered with $\alpha = 10^{-24}$ (simulation)	-11.48	-141.50	20.56	-23.66	-104.50
Relative bias (simulation)	8.83	13.69	-15.09	-7.90	13.52

6.4.3. Improved spatial constraints

Performance analysis based on simulated data

The analysis of the section showed that there is a strong signal leakage between neighboring drainage systems. In reality, there is little correlation between mass variations in different drainage systems. This fact was used in the improved first-order Tikhonov regularization approach (see Sect. 6.2.2). It was expected to significantly reduce signal leakage between different drainage systems.

To analyze the performance of the data inversion scheme after incorporating the improved first-order Tikhonov regularization, another numerical study is performed. Apart from the improved spatial constraints, the scenarios analyzed correspond to the noiseless synthetic data case of Sect. 6.4.3.1. Our goal is to compare the spatial patterns of the biases caused by the ordinary and the improved first-order Tikhonov regularization, when the same regularization parameters are used in both cases. We recall that the term “ordinary” regularization refers to the one that assumes the presence of correlations between neighboring mascons belonging to different drainage systems, while the term “improved” regularization refers to the case where these correlations are absent.

The “true” trend signal for the NW drainage system is shown in Fig. 6.6(a), whereas

the estimates obtained with the ordinary and improved spatial constraints and two different regularization parameters (i.e., 10^{-24} and 10^{-25}) are shown in Figs. 6.6(b)–(e). In addition, the differences between the estimates and the true trends are shown in Fig. 6.7. We see that the biases when using ordinary spatial constraints are significantly larger than those when using the improved spatial constraints, especially when the regularization parameter increases from 10^{-25} to 10^{-24} . When the regularization parameter is set equal to 10^{-25} , the RMS of the residuals between the estimated and the true signal per DS decreases by a factor of 15% (namely, from 1.3 to 1.1 Gt/yr) after switching from the ordinary spatial constraints to the improved ones. The reduction becomes even greater when the regularization parameter is increased to 10^{-24} (namely, from 6.4 to 2.8 Gt/yr, i.e., by 56%).

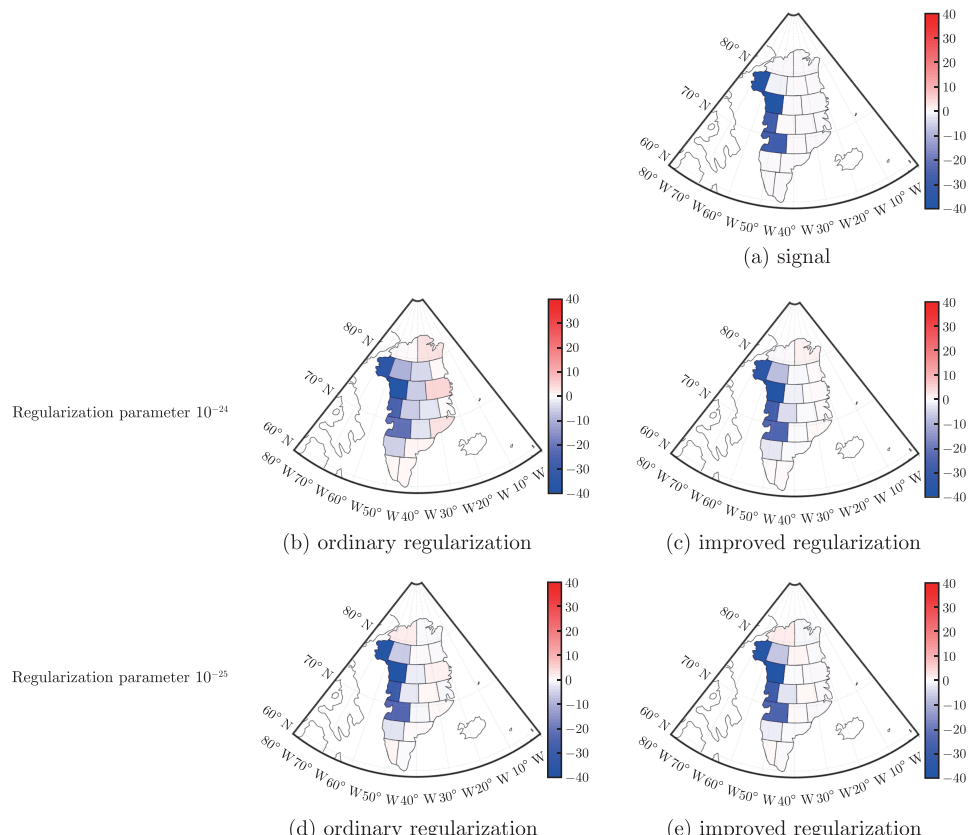


Figure 6.6 True (panel a) versus estimated trends (panels b–e) for ordinary and improved first-order Tikhonov regularization with two regularization parameters.

The results for the other drainage systems are similar (Table 6.4). In each case, the

true signal is constrained to only one drainage system, as indicated by the name of the corresponding column. The bias reduction caused by the improved spatial constraints is shown in percentages. The bias reduction remains at the level of 11%–25% in most cases, but can reach 56% when the regularization parameter of 10^{-24} is considered. Note that in the SE, the bias reduction is negligible when the regularization parameter is set to 10^{-25} . This is because the trend estimate obtained with the ordinary regularization (99.03 Gt/yr, see Table 6.4) is good enough compared to the true value (99 Gt/yr), thus limiting the room for further improvements. Besides, the NE shows less accurate trend estimates in the case of the improved spatial constraint under the regularization parameter of 10^{-24} . This is likely caused by an increased mutual compensation of the mass gain signal in the inner NE and the mass loss signal in the coastal NE (see Fig. C.3). The reason why the other drainage systems do not show such compensation is a homogenous mass loss signal in all the mascons within these drainage systems.

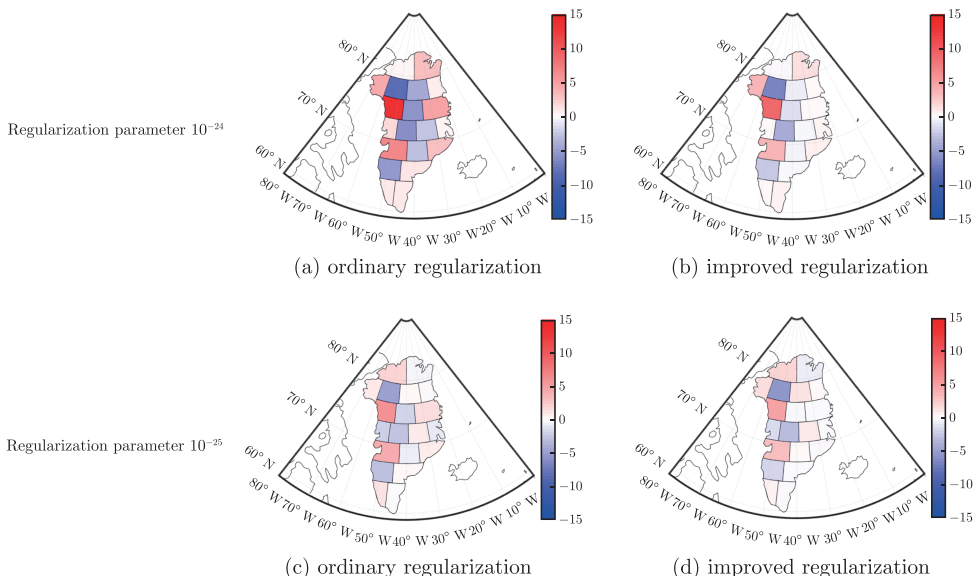


Figure 6.7 Trend signal of spectral leakage from the NW drainage system for ordinary and first-order Tikhonov regularization with two regularization parameters. The units are Gt/yr.

Performance analysis based on real data

This section examines the performance of the improved spatial constraints is investigated in the context of the real GRACE data. In Figs. 6.8 and C.4, which are similar to Figs. 6.3 and C.2 addressed above, the estimates of mass variations per drainage system derived from different mascon products are again shown. This time, the improved Tikhonov regularization has been applied to the TUD-SUSTech mascon

solutions. Note that the set of regularization parameters considered is the same as in the analysis based on the ordinary spatial constraints (cf. Fig. 6.3). The optimal regularization parameter found with the L-curve method is 10^{-25} (see Fig. C.5).

Table 6.4 RMS differences between the estimated and true trends-per-mascon, reflecting the biases caused by the ordinary and improved spatial regularization. The RMS differences are computed per drainage system. In each case, the true signal is limited to only one drainage system, as indicated by the name of the corresponding column. The first and second rows show the RMS biases after the ordinary spatial regularization for the two regularization parameters under consideration. The third and fourth rows present similar information in the case of the improved spatial regularization. The fifth and sixth rows refer to the reduction of these RMS differences when the improved regularization is compared with the ordinary one (a negative number corresponds to an increase in the RMS difference). The unit is Gt/yr.

		N	NW	NE	SW	SE
Ordinary (regularization)	RMS for $\alpha = 10^{-25}$	0.4	1.3	1.9	0.9	2.3
	RMS for $\alpha = 10^{-24}$	1.5	6.4	3.3	3.1	6.6
Improved (regularization)	RMS for $\alpha = 10^{-25}$	0.3	1.1	1.7	0.8	2.3
	RMS for $\alpha = 10^{-24}$	1.2	2.8	4.2	2.4	3.7
Bias (reduction)	for $\alpha = 10^{-25}$	25%	15%	11%	11%	0%
	for $\alpha = 10^{-24}$	20%	56%	-27%	23%	44%

Comparing Fig. 6.8 with Fig. 6.3, we see that the improved spatial constraints make the estimated mass variations more robust to the choice of the regularization parameter

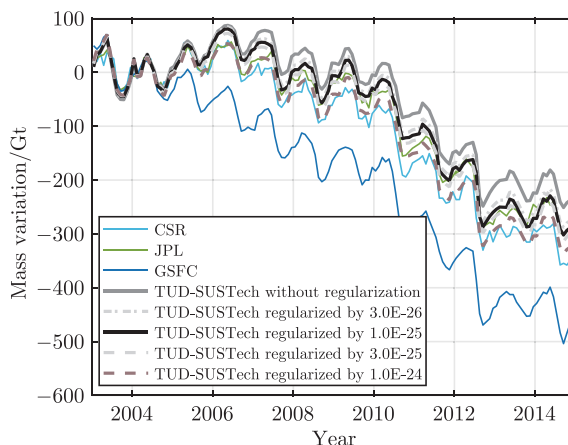


Figure 6.8 Mass anomaly time-series for SW from different mascon solutions. It is similar to Fig. 6.3, but after applying the improved first-order Tikhonov regularization, which helps reducing signal leakage from a drainage system to its neighbors.

compared to ordinary regularization; that is, the relative biases become much smaller. This is a direct consequence of the reduced signal leakage when using the improved first-order Tikhonov regularization. For example, in the NW drainage system, the cumulative mass variations from 2003 to 2014 obtained with the smallest (0) and largest (10^{-24}) regularization parameters differ by only about 100 Gt. In contrast, the difference using the ordinary spatial constraints was about 230 Gt. Reductions in the relative biases were also found for the other drainage systems.

The trend estimates for 2003–2014 from the CSR, JPL, and GSFC time-series, as well as from the TUD-SUSTech time-series (computed with both ordinary and improved spatial constraints) are shown in Table 6.5. The reduced signal leakage of the improved spatial constraints increases the mass loss rates in the SE and NW drainage systems by 8 Gt/yr and 4 Gt/yr, respectively, compared to the ordinary spatial constraints. It is also worth noting that the trend estimate for the NE strongly depends on the regularization parameter. In general, the long-term trend estimates for the DSs with the largest mass losses (i.e., NW and SE) are larger in the case of the improved spatial constraints, compared to those obtained with the ordinary constraints. On the other hand, the former show similar or smaller trend estimates in the other drainage systems, where mass losses are relatively small (i.e., N, SW, and NE). We explain this by the fact that the improved spatial constraints mitigate signal leakage from the drainage systems with the largest mass losses to the drainage systems with small mass losses.

Table 6.5 Estimated trends over 2003–2014 in Gt/yr from different mascon products. TUD-SUSTech solutions are produced with both ordinary and improved spatial constraints under the optimal regularization factor (i.e., 10^{-25}) determined by the L-curve method

	CSR	JPL	GSFC	TUD-SUSTech	
				Improved regularization	Ordinary regularization
N	-19	-23	-23	-17	-16
NW	-102	-114	-103	-120	-116
NE	-15	-10	-16	1	-5
SW	-32	-27	-44	-27	-31
SE	-95	-103	-105	-118	-110
GrIS	-268	-276	-291	-280	-277

Validation

After applying the improved spatial constraints to real GRACE data, we validated the obtained estimates with independent data, which is the subject of this section. In general, the lack of knowledge of the true signals makes it difficult to validate GRACE-based monthly estimates. However, it is known that the most reliable way to derive the

linear rates of mass variations is to combine many years of GRACE Level 1B data, as this significantly improves the spatial resolution and signal recovery and reduces signal leakage (Loomis et al., 2019b). Therefore, to validate the trend estimates, we use the GOCO-06S model, which was created by combining about 15 years (i.e., April 2002–August 2016) of GRACE data and data from 19 other satellites, including GOCE and SWARM (Kvas et al., 2021). Note that the GOCO-06S trend estimates were derived from GRACE and SLR data only. The other satellite data sets only contributed to the estimation of the static part of the solution. In addition, the GOCO solution was regularized to a high degree.

In this book, the SW drainage basin is chosen for validation. This is partly because there is a rapid mass loss signal in its neighbors, SE and NW. Mass loss estimates in the SW are sensitive to an appropriate choice of regularization, as they are substantially distorted by signal leakage from its neighbors (see the discussion in Sect. 4.2). We compute the long-term trend in the SW by considering the GOCO-06S SHCs up to different degrees: 60, 96, 120, and 200. A 120-km buffer is introduced to capture the signal leakage into the ocean. The overall GOCO-06S based trend in the SW decreases from -36 Gt/yr to -32 Gt/yr as the maximum spherical harmonic degree considered increases from 60 to 200 (see Table 6.6 and Fig. C.6). The estimated trend decreases with increasing spatial resolution due to a reduction in signal leakage from the neighboring drainage systems. Note also that the time intervals of GOCO-06S (April 2002 – August 2016) and of the mascon products (January 2003 – July 2016) are slightly different. Therefore, we made an additional test by adjusting the considered time interval of CSR and JPL mascon products to make it exactly the same as the time interval of GOCO-06S. It is found that the inconsistency caused by the differences in time-intervals (January 2003 – July 2016 versus April 2002 – August 2016) is negligible, i.e., at the level of 1 Gt/yr. By comparing different trend estimates, we find that the SW trend from GOCO-06S, CSR, JPL, and TUD-SUSTech are all similar, i.e., about -30 Gt/yr , while the GSFC trend estimate is much larger: -43 Gt/yr .

Table 6.6 Comparison of mass trend estimates of the SW drainage system from different mascon solutions (CSR, JPL, GSFC, and TUD-SUSTech) with those based on GOCO-06S model and the estimates from Input-Output Method. The unit is Gt/yr

CSR	JPL	GSFC	TUD-SUSTech		GOCO-06S				IOM
			(Improved regularization)	(Ordinary regularization)	60	96	120	200	
			-32	-27	-43	-27	-31	-36	-34

The mass balance of the SW drainage system can also be estimated by the Input and

Output Method (IOM) as SMB minus Ice Discharge (ID). In SW, the contribution of the latter is relatively small, which implies that errors in ID estimates (e.g., due to unaccounted temporal variations in ice flow velocities) are also small. This was another reason to select the SW drainage system as a test area. In our study, we combine the SMB trend estimate from the RACMO2.3p2 model, which offers a 1-km spatial resolution on a daily temporal scale (Noël et al., 2021), and the ice discharge estimate from (King et al., 2020). The SMB trend in SW over January 2003–July 2016 is -20 Gt/yr , while the ice discharge over the same time interval is 12 Gt/yr . The latter estimate is consistent with that of (Mankoff et al., 2020), and (Bevis et al., 2019), although the latter considered a slightly different geometry of SW. Then, based on the Input and Output method, the total mass balance in SW is -32 Gt/yr (see Table 6.6). This estimate is consistent with those based on CSR, JPL, TUD-SUSTech, and GOCO-06S.

6.5. Discussion

6.5.1. Global mass conservation

The mascon approach used by GSFC, CSR, and JPL, which deals with the GRACE Level-1B data, ensures a global mass conservation by estimating of a global set of mascons with the corresponding constraint equation that the sum of all mascons is equal to zero. The variants of the mascon approach using Level-2 data implicitly satisfy a global mass conservation, by assuming that the temporal variations of the C00 coefficient are equal to 0. As far as the computed mass anomalies are concerned, they are regional solutions by definition. A mass conservation in a regional solution is neither guaranteed nor required. For example, a solution that ensures a mass conservation in a region that includes only Greenland and surrounding areas would be completely unphysical. It would be fair to explicitly apply the mass conservation condition only when the mass anomalies are estimated globally from Level-2 data.

6.5.2. “Improved” regularization vs regularizations applied to other mascon solutions

The CSR mascon products are estimated by a temporally and spatially variable zero-order Tikhonov regularization. It means that no correlation between mascons is considered in the CSR mascon products. In this book, we cut off the correlations for

mascons in different drainage systems, but consider the correlations between mascons within the same drainage system. In doing so, our regularization method lies between the approach of CSR on the one hand and the JPL and GSFC approaches on the other.

6.5.3. Added value of the “improved” regularization

Our study shows an added value of the improved Tikhonov regularization, which assumes no signal correlations between pairs of mascons belonging to different drainage basins. Using a series of simulations, we show that the improved regularization mitigates signal leakage between drainage systems by 11%–56%. Then, in the real data analysis, it is also found that for the ordinary Tikhonov regularization, the estimates are quite sensitive to the choice of regularization parameters (see Fig. 6.3), while they become more robust when the improved regularization is applied (see Fig. 6.8). For example, for the improved Tikhonov regularization, the difference between trends over 2003–2016 obtained with the smallest regularization factor in Fig. 6.8 (i.e., 3.0×10^{-26}) and the largest regularization factor (i.e., 1.0×10^{-24}) is about 7 Gt/yr; for the ordinary Tikhonov regularization, the same difference is about 18 Gt/yr.

6

Our results are somewhat inconsistent with previous findings related to mass anomalies of hydrological origin for small river basins (Croteau et al., 2014). We explain this inconsistency by a relatively high level of random noise in the case of small river basins. Then, a positive effect of a reduced signal leakage is counteracted by an amplification of random noise, which takes place when the available data are insufficiently sensitive to the mass anomalies to be estimated. In other words, when cutting the signal correlations between mascons in different drainage systems, one has to watch a balance between reducing signal leakage and increasing random noise.

6.6. Summary

In this book, the CSR RL06, JPL RL06 and GSFC v2.4 mascon products are examined in the context of the ice mass balance of individual drainage basins of the Greenland Ice Sheet. The analysis reveals significant discrepancies between the mass variations accumulated from 2003 to 2014 are found, reaching values of up to 200 Gt depending on the drainage system. To better understand these discrepancies, a set of alternative mascon-type estimates is derived using the mascon approach of (Ran et al., 2018a). These estimates are constrained with a first-order Tikhonov-type regularization to

suppress noise. It is found that the mass anomalies at the drainage system scale based on CSR RL06, JPL RL06 and GSFC v2.4 mascon products can be well reproduced by the alternative mascon solutions when an appropriate regularization parameter is chosen. Thereby, the discrepancies between the CSR RL06, JPL RL06 and GSFC mascon products may be explained by differences in the spatial constraints applied by the analysis centers. The optimal fit to the JPL solutions requires the least amount of regularization.

A numerical study has been performed to investigate the regularization-driven biases (i.e., signal leakage) in trend estimates for GrIS drainage systems. We compare the simulated biases with those observed in our mascon solutions based on real GRACE data. Since the true signal in the context of real data is not known, we propose to evaluate “relative biases”, i.e., the differences between the estimates obtained with two different regularization parameters. By comparing the relative biases obtained in the simulations and in the real data processing, we find that they match each other reasonably well: the former explain in most cases 50%–70% of the latter ones.

6

To mitigate the bias caused by the regularization, improved spatial constraints have been implemented. The main assumption behind the improved spatial constraints is that there is no correlation between mascons in different drainage systems. Thus, the mass anomaly estimates obtained with the improved spatial constraints benefit from less signal leakage. Using simulated and real data, we show that the improved spatial constraints mitigate the signal leakage between drainage systems: the reduction is typically at the level of 11%–25%, but can reach 56% when considering a relatively large regularization parameter.

In addition, trend estimates in the SW drainage system derived from different mascon products are validated using the GOCO-06S model and the IOM (i.e., as SMB-ID). We found (cf. Table 6.6) that our estimates match well with the values from both alternative data sets.

Remarkably, the long-term trend estimates in the DSs with the largest mass losses (i.e., NW and SE) are larger in the case of the improved spatial constraints compared to those obtained with the ordinary spatial constraints. On the other hand, the former show smaller trend estimates in the areas of small mass loss (i.e., N, SW, and NE). This is further evidence that the improved spatial constraints mitigate signal leakage from the DSs with large mass loss outwards and thereby reducing distortions of signals in the small mass loss areas.

It is worth adding that the latest GSFC RL06 product does not apply temporal constraints and the regularization matrices are determined from the pre-fit range-acceleration residuals (Loomis et al., 2019a). The JPL and CSR processing centers have recently released new variants of the mascon products as well. We will further analyze all of these products in a follow-up study.

7

Optimal mascon geometry in estimating mass anomalies within Greenland from GRACE

7.1. Introduction

Mass variations in Greenland attract the attention of the scientific community because of their great potential to exacerbate future sea level rise. The Gravity Recovery and Climate Experiment (GRACE) satellite mission is one of the most valuable sources of information on these mass variations (Shepherd et al., 2012; Jacob et al., 2012; Khan et al., 2015; Stocker et al., 2013; Velicogna and Wahr, 2006; Velicogna, 2009; Velicogna et al., 2014; Schrama et al., 2014; Chen et al., 2006).

In this chapter, we analyze the estimation of mass variations in Greenland from GRACE data using the mascon approach, following Ran et al. (2018b). This is now a commonly-used way to transform GRACE data into mass anomalies (Forsberg and Reeh, 2007; Baur and Sneeuw, 2011; Schrama and Wouters, 2011; Schrama et al., 2014). In this approach, the target area is divided into laterally-homogeneous patches, which are called “mascons”. The accuracy of the estimates obtained in this way is sensitive to the parameterization of the target area, i.e., to the choice of the number and the geometry of the mascons (Bonin and Chambers, 2013). Different parameterizations of the Greenland area have been used so far in the literature. For example, Luthcke et al. (2006a) identified 6 drainage systems and divided each of them into two mascons, one for the area below the 2000 m elevation line and the other one for the area above the 2000 m elevation line. This rather coarse parameterization is not able to fully exploit the spatial resolution of GRACE. Therefore, finer parameterizations using mascons of a regular shape (e.g., equal-angle mascons, equal-area mascons or spherical caps) have been proposed (Rowlands et al., 2005; Luthcke et al., 2013; Schrama et al., 2014; Baur and Sneeuw, 2011; Watkins et al., 2015).

Up to now, it has been common to choose the size of the mascons independently of the temporal scale under consideration. However, such an approach may be suboptimal. The primary goal of this study is to investigate the optimal choice of the mascon size depending on the type of the estimates. We consider four types associated with different temporal scales:

- long-term linear trends (long-term temporal scale);
- inter-annual mass anomalies (intermediate scale);
- mean mass anomalies per calendar month (can also be considered as an intermediate scale, but based on an alternative way of averaging original information);
- monthly mass anomalies (short-term scale).

The variant of the mascon approach presented in Ran et al. (2018a) is used in this study to compute the statistically-optimal estimates of mass anomalies. Furthermore, we use the procedure proposed by Ran et al. (2018a) to divide Greenland into nearly equal-area mascons of a desired size, taking into account the coast geometry. In order to better understand the link between the accuracy of the obtained estimates and the chosen parameterization, we start from a numerical study, where individual error sources are quantified. This allows us to make a proper interpretation of the results obtained from real GRACE data in the second stage and supports our recommendations regarding the optimal choice of parameterization.

7

It is important to note that only ~81% of Greenland's territory is covered by the Greenland Ice Sheet (GrIS). The rest is covered by tundra and isolated glaciers. In view of the limited spatial resolution of GRACE, the latter also contribute to GRACE-based estimates (unless the mass variations outside the GrIS are corrected for using hydrological models). Therefore, in this study we refer to Greenland mass anomalies rather than to GrIS mass anomalies.

The rest of this chapter is organized as follows. In Sect. 7.2 , we briefly introduce the different parameterizations used in this study. In Sect. 7.3, we analyze a numerical study based on simulated signal and data. In Sect. 7.4, we analyze real GRACE data. Finally, in Sect. 7.5, we provide a summary and the conclusions.

7.2. Methodology and parameterization

7.2.1. Adopted mascon approach

The adopted variant of the mascon approach (Ran et al., 2018a) stems from the methodology proposed by Forsberg and Reeh (2007) and Baur and Sneeuw (2011). First, we

use the differences between monthly spherical harmonic coefficients (SHCs) and their long-term mean values to synthesize gravity disturbances at satellite altitude. The data area covers the whole of Greenland extended by an 800-km wide buffer zone. Numerical studies in Ran et al. (2018a) have shown that such a buffer zone is the best choice. Second, we compute a design matrix (\mathbf{A}) that links the gravity disturbances (\mathbf{d}) at satellite altitude to the mass anomalies of the mascons (mascon parameters \mathbf{x}). Importantly, each column of the design matrix is computed by taking into account that the data and the mascon model must be spectrally consistent (Ran et al., 2018a). More specifically, each column of the design matrix can be treated as a set of gravity disturbances caused by the corresponding mascon of unit surface density. The computation is done in three steps. First, the gravity disturbances are computed on an equiangular global grid. Second, a set of spherical harmonic coefficients (SHCs) is computed using the spherical harmonic analysis. Third, the produced SHCs are used to compute spectrally-limited gravity disturbances at the predefined data points.

Finally, the mascon parameters are estimated using the weighted least-squares technique (Eq. 7.1). The weight matrices (\mathbf{C}_d^{-1}) are taken as a pseudo-inverse of the noise covariance matrices of the gravity disturbances. The latter are computed from the full noise covariance matrices of the SHCs using the law of covariance propagation. The data weighting using these matrices can significantly reduce random noise (Ran et al., 2018a). In addition, similar to Bonin and Chambers (2013) and Schrama and Wouters (2011), we apply the zero-order Tikhonov regularization to stabilize the normal matrix and reduce noise in the estimates:

$$\mathbf{x} = (\mathbf{A}^T \mathbf{C}_d^{-1} \mathbf{A} + \alpha \mathbf{R})^{-1} \mathbf{A}^T \mathbf{C}_d^{-1} \mathbf{d}, \quad (7.1)$$

where the regularization matrix \mathbf{R} is the unit one and α is the regularization factor, which is determined by the L-curve method (Hansen, 1992).

However, random noise may not be the dominant source of error (at least, at some of the temporal scales considered in this study). Therefore, we also use the ordinary least-squares techniques to estimate the mascon parameters.

7.2.2. Parameterization of Greenland

The parameterizations considered in this study are designed according to the procedure of Ran et al. (2018a), and comprise almost equal-area mascons of a prescribed size. In this way, the whole Greenland is divided into 23 mascons (each with an area of $\sim 90,000 \text{ km}^2$), 36 mascons ($\sim 62,500 \text{ km}^2$), or 54 mascons ($\sim 40,000 \text{ km}^2$) (cf. Fig. 7.1(d)–

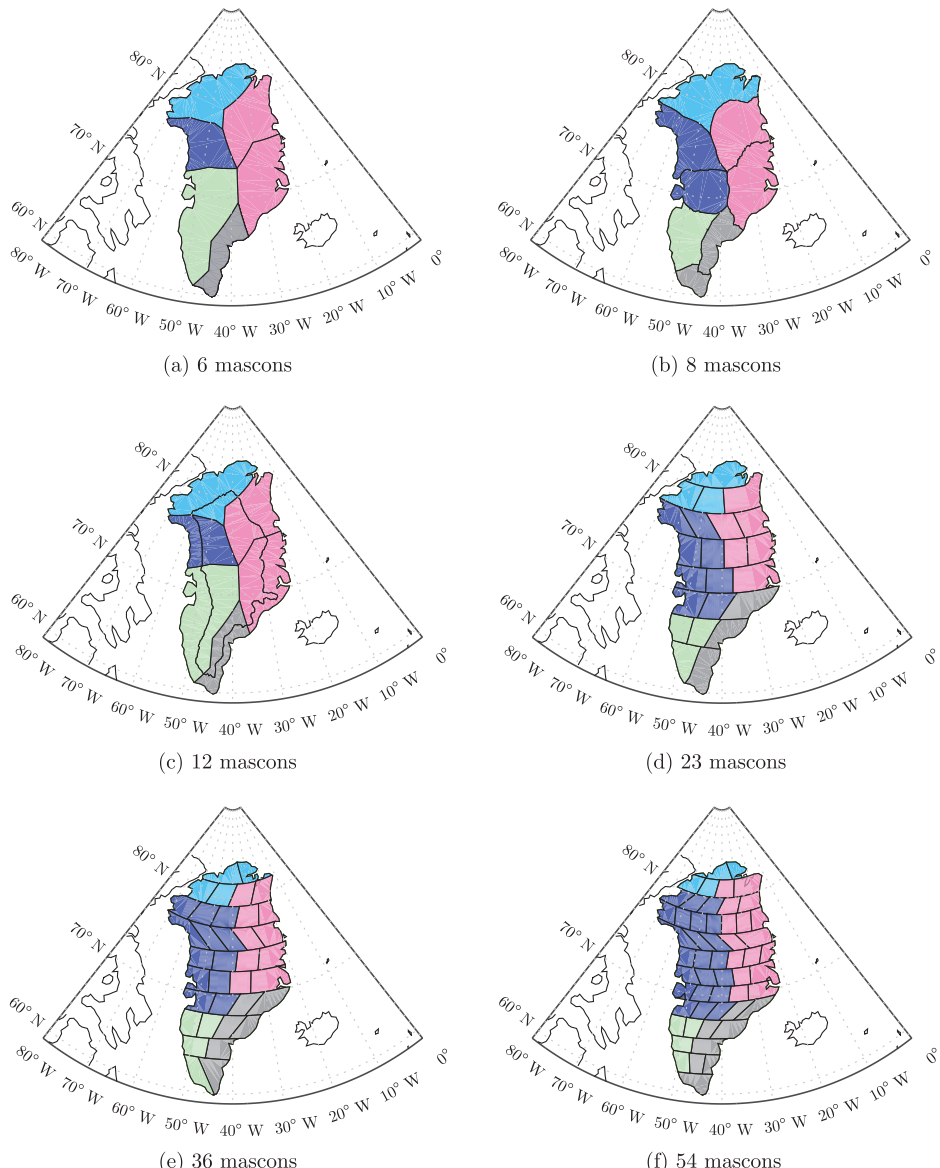


Figure 7.1 The parameterizations of Greenland considered in this study. Greenland is divided into five regions, which are aggregated from mascons. The regions roughly follow the geometry of the five drainage systems, which are outlined in different colors, i.e., North (N) in light blue, Northeast (NE) in red, Southeast (SE) in gray, Southwest (SW) in green, and Northwest (NW) in blue.

(f)). In addition, we consider three other parameterizations frequently used in the literature: with 6 mascons (Luthcke et al., 2006a), 8 mascons (Zwally et al., 2012), and 12 mascons (Luthcke et al., 2006a) (Fig. 7.1(a)–(c)). Note that the divisions into 6 and 8 mascons follow the geometry of major drainage systems. The Greenland mascons are supplemented by 9 mascons outside Greenland to reduce the inward signal leakage from regions around Greenland (Yi et al., 2016; Ran et al., 2018a).

7.3. Numerical study

To understand the impact of the parameterization on the accuracy of the estimated mass variations at different temporal scales, and to understand how this error compares to other sources of error, a series of numerical experiments are conducted with synthetic data. The experimental set-up and the results are presented in Sects. 7.3.1 and 7.3.2, respectively.

7.3.1. Experimental set-up

The basic set-up includes the definition of the true signal and the definition of the individual error sources to be considered in the simulations.

"True" signal

The "true" signal is composed of a long-term linear trend and other temporal variations. The long-term trend is based on ICESat laser altimetry estimates for the period 2003–2009. Their spatial resolution is $20\text{ km} \times 20\text{ km}$ (Felikson et al., 2017). Assuming a density of 917 kg/m^3 for the material responsible for elevation changes (Wahr et al., 2000), the elevation change rates are converted to mass change rates in terms of equivalent water heights (EWH) (Fig. 7.2). The linear trend over the tundra area is set equal to zero. The integration of the obtained trends over the whole of Greenland results in a value of -110 Gt/yr , which is much lower than the value based on GRACE data for the period 2003–2013, about -286 Gt/yr (Ran et al., 2018a). To make the ICESat-based estimates more realistic, we upscale all of them with a single scale factor of 2.6. A similar upscaling procedure was previously applied by Bonin and Chambers (2013).

The other simulated mass variations are based on Surface Mass Balance (SMB) time series from the RACMO 2.3 model (Noël et al., 2015). The spatial resolution is about $11\text{ km} \times 11\text{ km}$, while the temporal sampling is 1 day. The output from RACMO 2.3 during the 2003–2013 time interval was integrated over time to produce daily mass

anomalies. Monthly mass anomalies were then computed, resampled them to the $20\text{ km} \times 20\text{ km}$ patches in order to make them consistent with the ICESat data, and de-trended. The resulting time-series describe predominantly seasonal mass variations (their annual amplitudes are shown in Fig. 7.2). Then, we combined the de-trended signal with the trend from ICESat to obtain the “true” signal. Note that the “true” signal over the tundra area lacks long-term trends and is therefore dominated by seasonal variations.

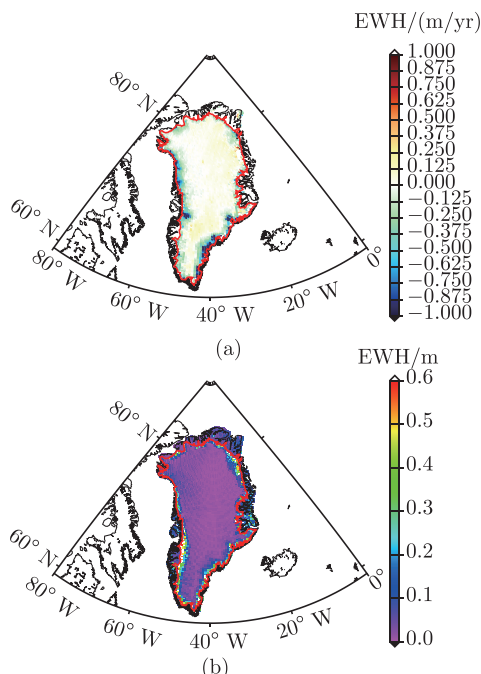


Figure 7.2 (a) GrIS mass change rate per $20\text{ km} \times 20\text{ km}$ patch from ICESat data over the period 2003–2009 (EWH: m/yr). The thick red curve is the ice mask indicating the ice sheet boundary. (b) Amplitude of annual mass variations over the whole of Greenland for the period 2003–2013 extracted from RACMO2.3 (EWH: m).

The “true” mass anomalies defined at the $20\text{ km} \times 20\text{ km}$ blocks were used to compute gravity disturbances on an equal-angle global grid at satellite altitude. The gravity disturbances were expanded in spherical harmonics complete to a certain maximum degree (namely, degree 96) using spherical harmonic analysis. Finally, the truncated spherical harmonic model was used to generate spectrally-limited gravity disturbances representing the error-free data. The spectral content of the simulated data is similar to that of the real GRACE data. Furthermore, the procedure used to compute the simulated data is basically the same as that used to compute the design matrix (Sect. 2.1). This

ensures that the spectral consistency between the data and the mascon model. In the absence of the spectral consistency, the estimated mass anomalies may suffer from large errors, especially when the optimal data weighting is applied Ran et al. (2018a).

Simulated noise

Different types of errors are added to the “true” signal: signal leakage, AOD noise, and random noise. In addition, parameterization errors, sometimes referred to as “model errors” (Xu, 2010; Stedinger and Tasker, 1986), are automatically included due to the much higher spatial resolution of the “true” signal compared to the size of the mascons.

Signal leakage. In this study, signal leakage refers to the signal from mass anomalies outside Greenland (e.g., the glaciers of the Canadian Arctic Archipelago, northern Canada, Iceland, Svalbard, etc., see Fig. 7.3), that may confound estimates of mass anomalies in Greenland (i.e., inward signal leakage is meant). To include leakage errors, we generated mass variations in the surrounding land areas using GRACE monthly land water mass grids from GRACE Tellus (Swenson, 2012). Consistent with the time interval of the “true” signal, we considered 123 monthly solutions over the period 2003–2013 (9 months were excluded from the data processing due to lack of data). The simulated trends and annual amplitudes extracted from the monthly GRACE Tellus solutions over the mascons located outside Greenland are shown in Fig. 7.3.

AOD noise. Uncertainties in the background models used to produce the monthly GRACE solutions may cause inaccuracies in the mass variation estimates. One such background model is the Atmosphere and Ocean De-aliasing model release 05 (AOD) (Dobslaw et al., 2013). Here, we defined AOD errors as 10% of the monthly mean signal (Thompson et al., 2004; Ditmar et al., 2012).

Random noise. The random noise in the monthly GRACE solutions was generated from the noise covariance matrices of the monthly GRACE solutions provided by CSR. It contains north-south stripes that vary by latitude and from month to month, as do the noise stripes in the real GRACE data. We have produced several different realizations of random noise, one realization per month. Ideally, this should be done per month using the corresponding noise covariance matrix. However, such an approach is very time consuming, especially when using a weighted least-squares estimator. Therefore, we chose the noise covariance matrix of June 2008 as a representative, and generated noise realizations for each month based on this noise covariance matrix.

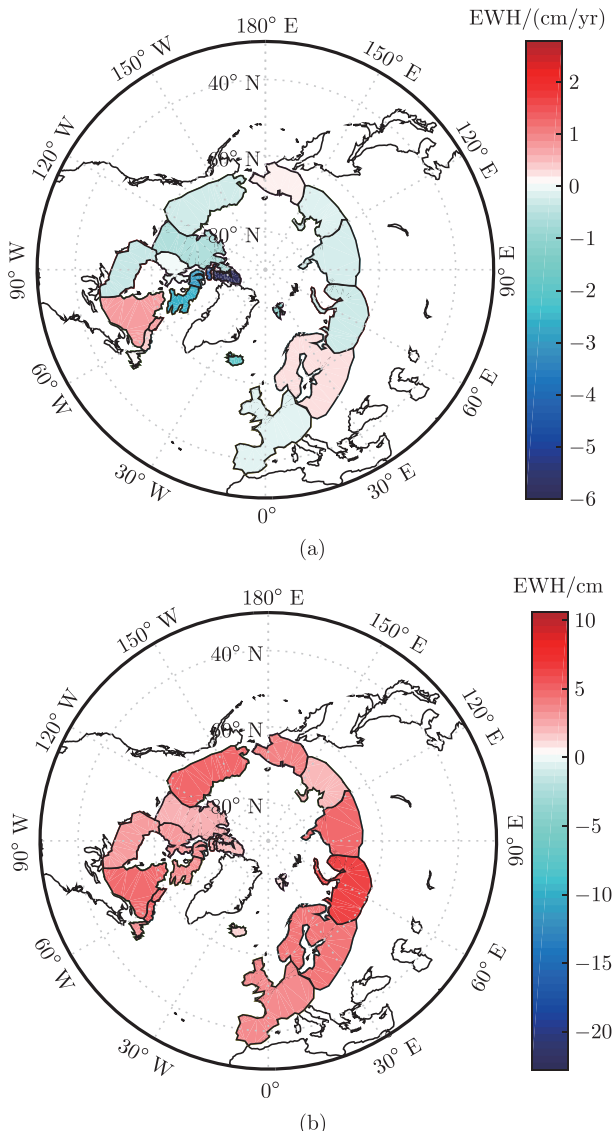


Figure 7.3 (a) Rate of linear mass changes for mascons outside Greenland (EWH: cm/yr). (b) The annual amplitude of mass change for those mascons outside (EWH: cm). The mascons outside Greenland are introduced to simulate the inward signal leakage.

Parameterization error. The actual mass anomaly distribution is a continuous function, while the mascon approach assumes a uniform mass distribution within each mascon. This inconsistency can introduce parameterization errors (also called “model errors”). In other words, the parameterization error represents the disturbances caused by

replacing the actual mass anomaly distribution with a single mean value per mascon. The parameterization error (PE) of a mascon in terms of surface density could be mathematically defined as

$$PE(\phi, \lambda) = \rho(\phi, \lambda) - \bar{\rho} \quad (7.2)$$

where $\rho(\phi, \lambda)$ is the density of mass anomaly at grid point (ϕ, λ) inside the mascon, while $\bar{\rho}$ is the mean density. Eq. 7.2 provides the input to compute the parameterization error in terms of gravity disturbances, consistent with other errors. In our study, the incorporation of parameterization errors takes place in a natural way, since the “true” signal is defined over $20 \text{ km} \times 20 \text{ km}$ patches, which are much smaller than the size of the mascons. In the simulations without parameterization errors, we define the “true” signal per mascon as the sum of the mass anomalies at all $20 \text{ km} \times 20 \text{ km}$ patches within the given mascon, which is homogeneously distributed over the mascon. Note that the parameterization errors are different in different months, since the simulated signal varies from month to month.

7.3.2. Results

In our study, we address i) long-term linear mass variation rates, ii) interannual mass anomalies, iii) mean mass anomalies per calendar month, and iv) monthly mass anomalies. We examine the impact of the parameterization on these estimates and select the best parameterization in each case. We conduct the analysis at the drainage system level. For this purpose, we divide Greenland into five regions that roughly follow the geometry of the drainage systems defined in Van den Broeke et al. (2009). The geometries of the regions aggregated from the mascons are shown in Fig. 7.1. Note that it is not possible to make the geometries of the five drainage systems (as shown in Fig. 7.1 with different colors) to be exactly the same for different parameterizations. However, the impact of the differences between the resulting geometries is small because we compare the estimates for each drainage system with the “true” value based on the same geometry. The estimates and RMS errors in this study are reported in units of Gt. Switching to equivalent water heights in units of metres has no impact on the main conclusions of this study.

As it is explained in Sect. 2.1, all the computations are performed using two estimators: i) a weighted least-squares estimator and ii) the ordinary least-squares estimator. The corresponding solutions are referred to as solutions with and without data weighting, respectively. When using the weighted least-squares estimator, we compute the weight matrix based on the June 2008 data noise covariance matrix.

In our analysis, we address not only the propagated noise, but also the bias introduced by the zero-order Tikhonov regularization. To quantify this bias, we invert the error-free data and take the difference between the obtained estimates and the true signal. When analyzing the contribution of a single error source to the total error budget, one subtract the bias to avoid its “double-counting”. The bias in the estimates usually increases rapidly with the regularization factor. Please see Sect. 3.2.1 for further discussion.

The optimal regularization parameter is defined separately for each parameterization and each type of estimates (i.e., each time scale). To do this, we invert the simulated data with all the error sources switched on and try different regularization parameters. The parameter that results in the smallest difference between the recovered estimates and the true signal is defined as the optimal one. Then, it is applied also in the scenarios where individual error sources are considered. This ensures the consistency of the obtained results and allows for their use in the analysis of the total error budget.

Recovery of long-term linear trends

After summing up the recovered mass anomalies over all mascons within each drainage system, we extracted the linear trend ($t^{\text{recovered}}$) of mass change in Gt/yr, co-estimated with bias, annual, and semi-annual terms. The true linear trend (t^{true}) at the drainage system scale was estimated from the true mass anomaly time-series. As quality measure, we use the RMS difference between the estimated and true linear trends. This RMS difference is referred to as the “total RMS error” when all error sources are included, and computed as

$$\text{RMS}_t = \sqrt{\frac{\sum_{n=1}^5 (t_n^{\text{recovered}} - t_n^{\text{true}})^2}{5}}. \quad (7.3)$$

where n represents the n -th drainage system. If only a single noise source is considered, the corresponding RMS difference is referred to as RMS AOD error, RMS leakage error, RMS parameterization error, and RMS random error, respectively.

The total RMS error as a function of the total number of mascons is shown in Fig. 7.4. The smallest total RMS error (~6 Gt/yr) is obtained when the number of mascons ranges from 23 to 54, with little difference within this range, no matter whether data weighting is switched on or not. As far as individual error sources are concerned, Fig. 7.4 shows that the RMS parameterization error is dominant when data weighting is used. If the data weighting is absent and number of mascons ≥ 23 , the bias is comparable to or even larger than the parameterization error. This is caused by the fact that the normal matrix for a large number of mascons is ill-posed (especially in the absence of data weighting,

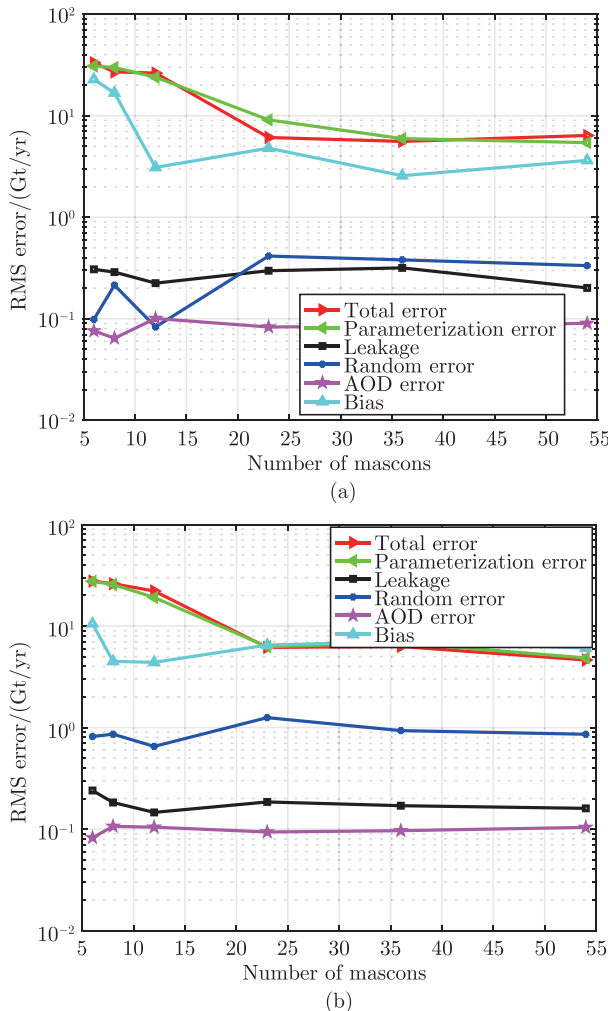


Figure 7.4 Total RMS error and RMS error of individual error sources of linear trends at drainage system scale in units of Gt/yr. Weighted least-squares estimator (a) versus ordinary least-squares estimator (b), as a function of the number of mascons.

which reduces the condition number of the normal matrix; see Fig. 7.5). Thus, a strong regularization is needed to suppress the propagated noise.

The RMS random error in the estimated trends is quite small: ~ 0.5 Gt/yr and ~ 1 Gt/yr with and without data weighting, respectively. This is about an order of magnitude smaller than the RMS parameterization error. The RMS leakage error and the RMS AOD error are either comparable to the RMS random error or even smaller.

Based on the results shown in Fig. 7.4, we conclude that data weighting is not necessary if one is interested in the long-term linear trend at the drainage system scale. The ordinary least-squares estimator provides comparable results. This is not surprising, since the data weighting is designed to suppress random noise, while the dominant contributor to the error budget is parameterization error. The optimal number of mascon for trend estimates is in the range of 23 to 54.

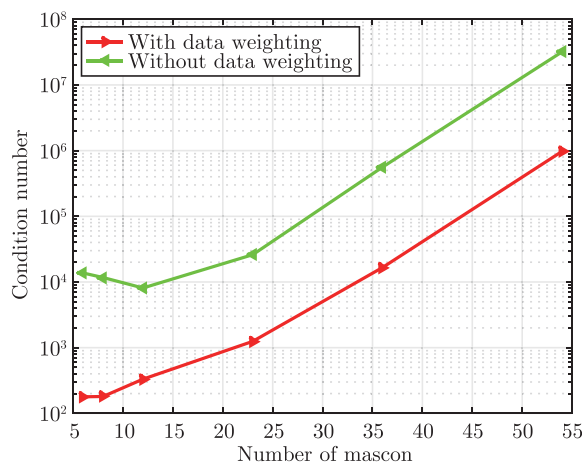


Figure 7.5 Condition numbers of the normal matrices when using the ordinary least-squares estimator (green) and the weighted least-squares estimator (red), as functions of the number of mascons. Note that no regularization is used when computing the condition numbers.

7

In Fig. 7.6, we have partitioned the error budget of trend estimates per mascon into individual error sources, when parameterizing Greenland with 23 mascons and switching on data weighting. In addition, the recovered and true trends per mascon are shown. The figure shows that in general the mascon approach is capable to recover the spatial pattern of mass anomalies in Greenland.

Next, we analyze the linear trend estimates integrated over all of Greenland. As an example, we take the parameterization with 23 mascons, which is one of the best parameterizations to estimate the trends at the drainage system scale, as discussed above. The impact of the regularization parameter on the trend estimates obtained both with and without data weighting is presented in Fig. 7.7. We find that in the case of data weighting, the regularization biases the trend estimates by about 1 Gt/yr when the regularization parameters are small, and by \sim 6 Gt/yr when the regularization parameters are chosen to yield the best trend estimates at the drainage system scale. In

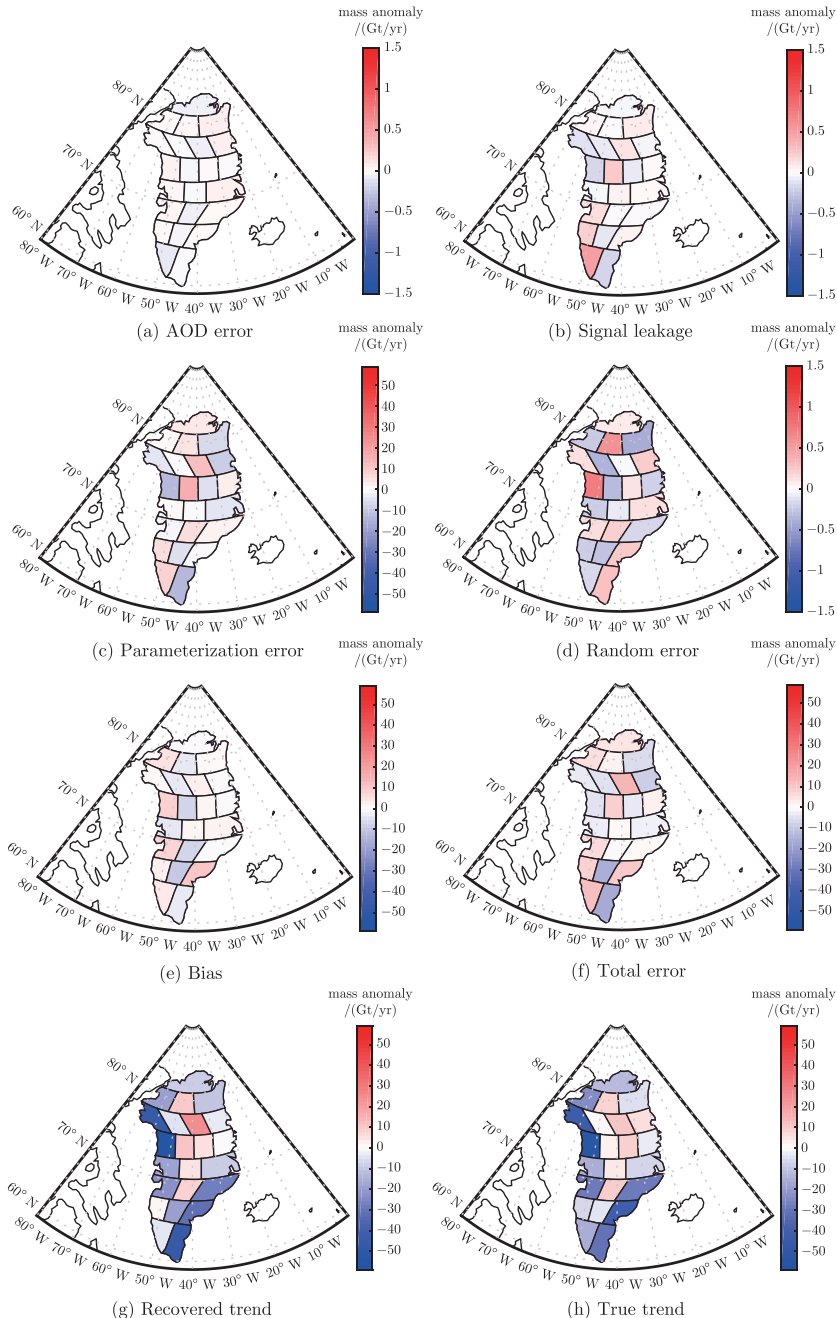


Figure 7.6 Contributors to the error in linear trend estimates: AOD error (a), signal leakage (b), parameterization error (c), random error (d), bias (e), and total error (f). For completeness, we also show the recovered trend (g) and true trend (h). The units are Gt/yr. Please note that two different color bars are used according to the amplitude of the noise or signal levels.

addition, it is found that the bias increases rapidly with the regularization parameter, regardless of whether data weighting is applied or not. Therefore, considering the larger total error of the regularized case (~ 6 Gt/yr) compared to the unregularized case (~ 1 Gt/yr), we suggest not to apply regularization when estimating the trend for all of Greenland.

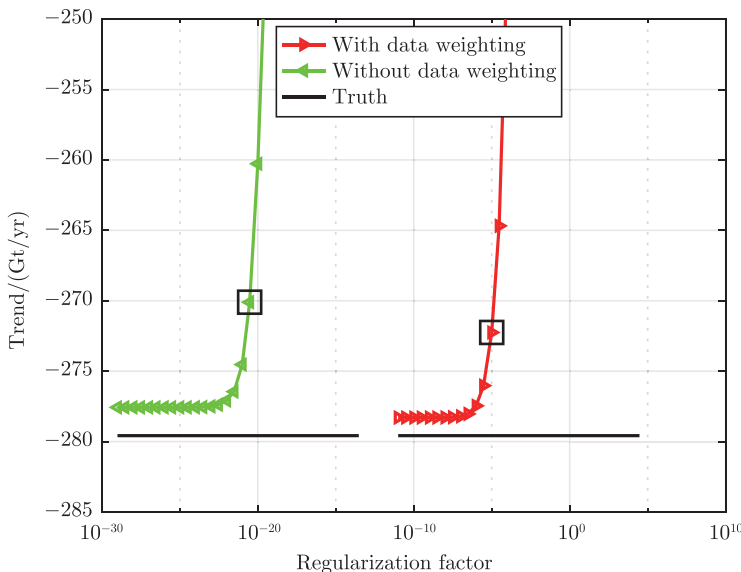


Figure 7.7 The impact of the regularization parameter on trend estimates integrated over all of Greenland, with and without data weighting. The true trend is shown in black, while the estimates obtained with the “optimal” regularization parameters are highlighted as black squares. The “optimal” regularization parameters are defined from the analysis of trend estimates at the drainage system scale.

The results obtained with different parameterizations without a regularization are shown in Fig. 7.8. To begin with, we notice that the total RMS error decreases as the number of mascons increases. The minimum is attained for a large number of mascons (i.e., larger than 23) no matter whether data weighting is used (-0.8 Gt/yr) or not (2.0 Gt/yr). When using a small number of mascons, the total RMS error can be very large, especially when no data weighting is applied. For example, when using just 6 mascons, the total RMS error is ~ 6 Gt/yr with data weighting and ~ 40 Gt/yr without data weighting, respectively. The parameterization error is the dominant contributor to these large errors, while all the other errors are negligible.

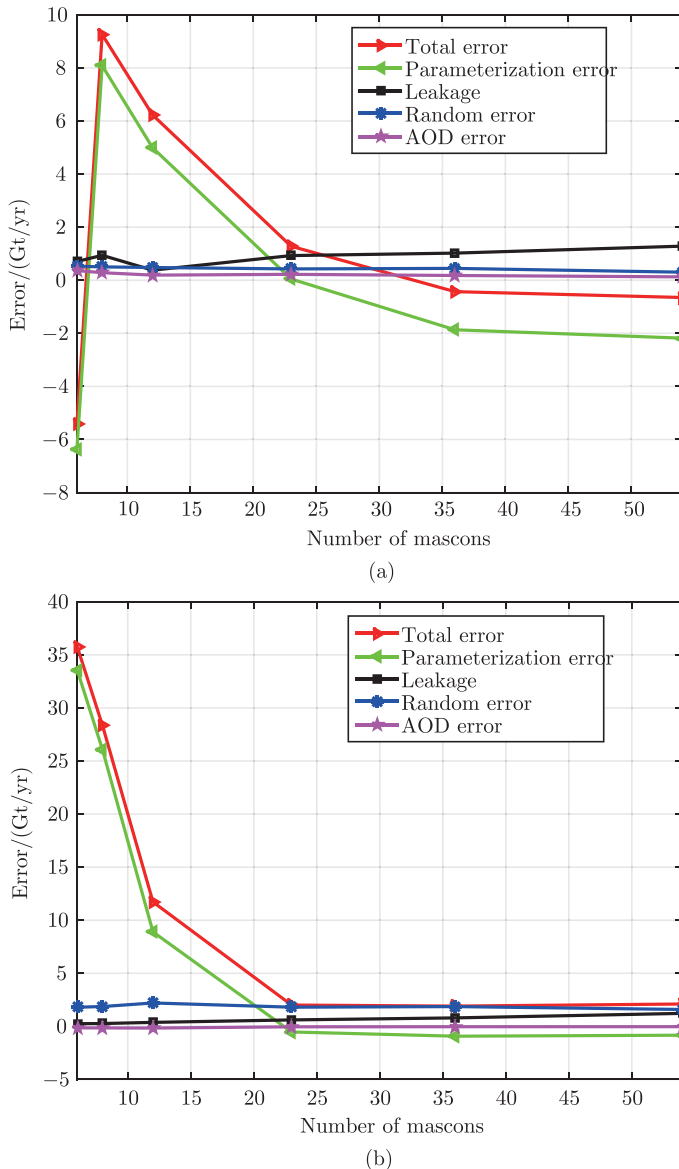


Figure 7.8 Errors in the linear trend (in Gt/yr) over all of Greenland obtained with the weighted least-squares estimator (a) and the ordinary least-squares estimator (b), respectively, as a function of the number of mascons.

We conclude that when estimating a linear trend for all of Greenland, one needs to take care that enough mascons (e.g., not less than 23) are used to reduce the parameterization error. The choice of a sufficiently large number of mascons is particularly important

when the ordinary least-squares estimator is used. The highest quality is obtained when the weighted least-squares estimator is used in combination with a sufficiently large number of mascons.

Recovery of inter-annual mass anomalies

The inter-annual mass variations are another quantity of interest in Greenland mass balance studies. In this section, we investigate the sensitivity of the estimated inter-annual mass variations to the chosen parameterization at the drainage system scale.

We start by removing the long-term trend from the time series obtained for each mascon. After that, we compute the inter-annual mass variations, together with the mean mass anomalies per calendar month, which will be studied in the next section. For this purpose, we use the functional model

$$m^{i,j} = \overline{\hat{m}}^i + \hat{b}^j, \quad (7.4)$$

where $\{m^{i,j} : i = 1 \dots 12, j = 1 \dots J\}$ is the mass anomaly of month i and year j , with J being the number of years. \hat{b}^j is the mean anomaly of year j , which accounts for the inter-annual variability. $\overline{\hat{m}}^i$ is the mean mass anomalies of calendar month i . We add the constraint

$$\sum_{i=1}^{12} \overline{\hat{m}}^i = 0 \quad (7.5)$$

to guarantee the uniqueness of the solution. The $12 + J$ parameters per mascon are estimated using ordinary least-squares. The corresponding interannual variations for each drainage system are calculated by summing over all the mascons within the drainage system.

The RMS error of inter-annual mass variations per drainage system, IA , was computed as the RMS difference between the estimated and the “true” inter-annual mass variations of all years, i.e.,

$$IA = \sqrt{\frac{\sum_{j=1}^J (b_j^{\text{recovered}} - b_j^{\text{true}})^2}{J}}. \quad (7.6)$$

Then, the RMS error of the inter-annual mass variations was computed as follows:

$$\text{RMS} = \sqrt{\frac{\sum_{k=1}^5 IA_k^2}{5}}. \quad (7.7)$$

This RMS error was used to quantify the total RMS error and the RMS error per error source for the estimates obtained both with and without data weighting. The results obtained for different parameterizations are shown in Fig. 7.9. The smallest total RMS error (~ 4 Gt) is obtained for 23 mascons with data weighting, which is slightly smaller than the smallest error (~ 5 Gt) without data weighting. Note that a comparable quality is also found for a larger number of mascons (36-54 mascons). Regarding the individual error sources, the parameterization error is dominant only when the number

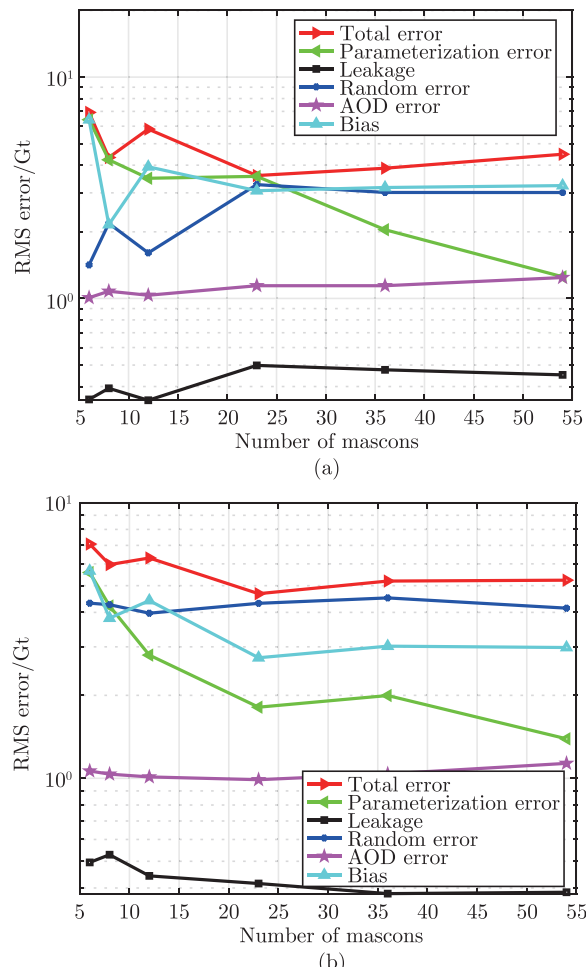


Figure 7.9 Total RMS error and RMS error of individual error sources of inter-annual mass variations at the drainage system scale as a function of the number of mascons, in units of Gt. Weighted least-squares estimator (a) versus ordinary least-squares estimator (b).

of mascons is small (6–12 in the case of data weighting and 6 in the case of no data weighting). In contrast, the random error, in general, increases with the number of mascons, and becomes the dominant error sources when the number of mascons is ≥ 36 (with data weighting) or ≥ 12 (without data weighting). Note that the random error does not increase significantly with the number of mascons, which is caused by the spatial regularization. When the spatial regularization is switched off, the random error in the estimates increases significantly (not shown here). The bias stays at the levels comparable either with the random error or the parameterization error (whichever is larger). The leakage and AOD error are negligible: at the level of 0.4 Gt and 1 Gt, respectively.

Fig. 7.10 shows the “true” and estimated inter-annual mass variations for each drainage system and for all of Greenland in the 23-mascon case, when data weighting is applied. The plot suggests that the recovered inter-annual mass variations are in a good agreement with the true ones. For completeness, the RMS errors of the estimates obtained with and without data weighting, the RMS of the true inter-annual mass anomalies, and Signal-to-Noise Ratios (SNRs) are shown in Table 7.1. The largest SNR (6.0) is obtained in the case of 23 mascons in combination with data weighting. Note that a comparable SNR is also observed for 36–54 mascons.

7

From the analysis above, we conclude that parameterizing Greenland with 23–54 mascons in combination with data weighting provides the best inter-annual mass variation estimates.

Recovery of mass anomalies per calendar month

Mean mass anomalies per calendar month are useful for studying the seasonal cycle of mass variations and the associated processes (Ran, 2017). Here, we examine the impact of the parameterization on the accuracy of estimated mean mass anomalies per calendar month at the drainage system scale. Note that, consistent with Ran (2017), we do not remove the long-term variability from the estimated and the true time-series.

As it is already mentioned in Sect. 3.2.2, the mean mass anomalies per calendar month are extracted from the mass anomaly time-series as the least-squares solution of the system of linear equations given by Eqs. 7.4 and 7.5. Note that the least-squares analysis is superior to the simply averaging of the mass anomalies per calendar month over many years. This is due to the long-term variability that needs to be properly accounted for, especially in the presence of data gaps. For example, the absence of January data for

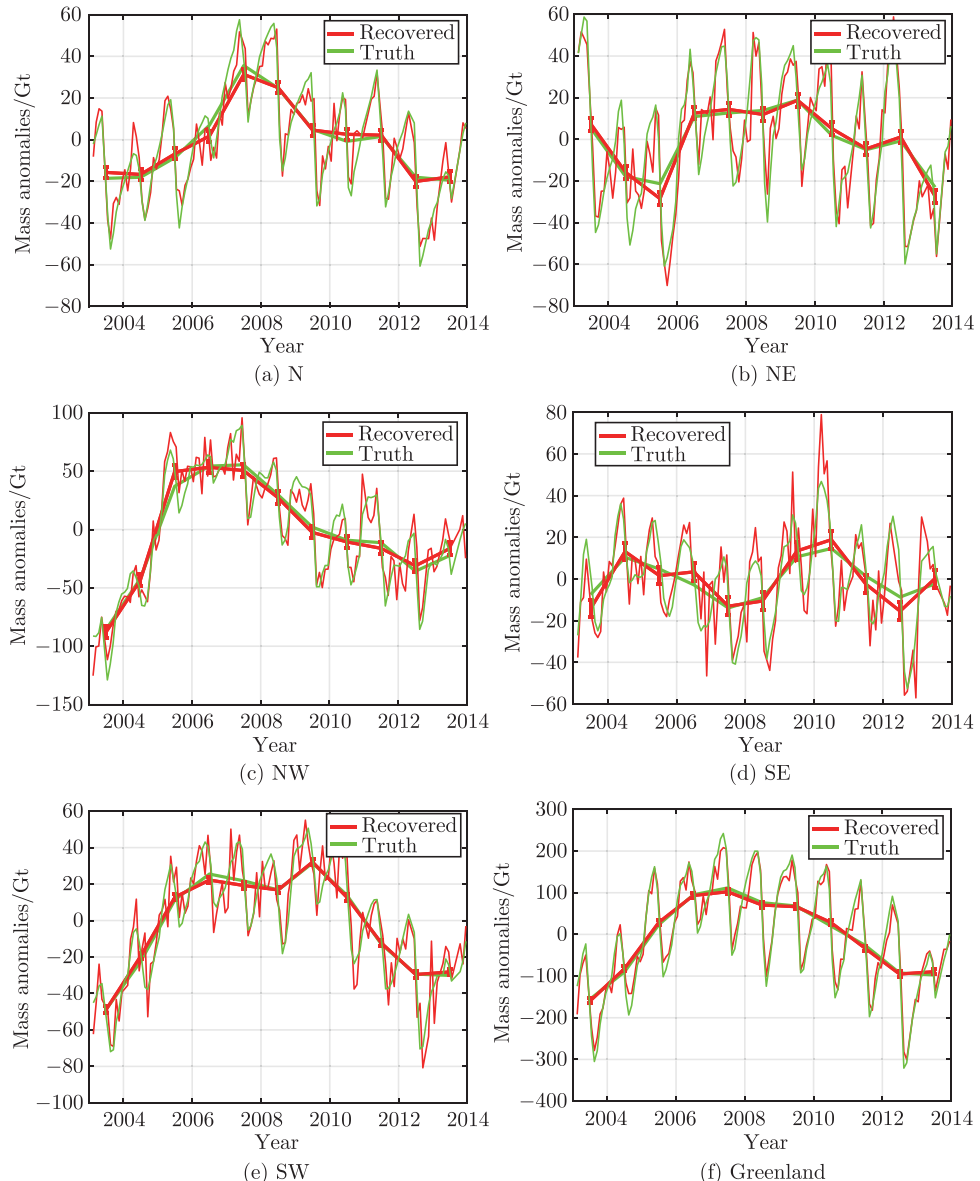


Figure 7.10 The regularized estimates of inter-annual mass variations and the “true” ones obtained in the numerical study for each drainage system and for all of Greenland in the 23-mascon case. Data weighting is applied. The estimated and the “true” de-trended time-series are shown as dash lines for reference. The RMS difference between the “true” and the estimated values is shown as an error bar.

Table 7.1 The statistics of inter-annual mass variations estimated from synthetic data. The units are Gt

		Number of mascons					
	Data weighting	6	8	12	23	36	54
RMS errors	Yes	6.9	4.3	5.7	3.6	3.9	4.5
RMS errors	No	7.1	6.0	6.3	4.7	5.2	5.2
RMS of the true mass anomalies	—	25.7	21.5	23.1	21.4	21.5	22.3
SNR	Yes	3.7	5.0	4.0	6.0	5.6	5.0
SNR	No	3.6	3.6	3.7	4.6	4.1	4.3

several years in a row can lead to a significant offset in the January average value with respect to other months. The use of a least-squares method solves this problem.

The RMS error per drainage system, τ_k , was computed as the RMS difference between the estimated and the “true” mean mass anomalies for all 12 months, i.e.,

$$\tau_k = \sqrt{\frac{\sum_{n=1}^{12} (\bar{m}_{k,n}^{\text{recovered}} - \bar{m}_{k,n}^{\text{true}})^2}{12}}, \quad (7.8)$$

where $\bar{m}_{k,n}^{\text{recovered}}$ and $\bar{m}_{k,n}^{\text{true}}$ are the estimated and true mean mass anomalies of the k-th drainage system at month n, respectively. As an example, Fig. 7.11 shows the mean true mass anomalies per calendar month of the Northern (N) drainage system when using a parameterization of 8 mascons.

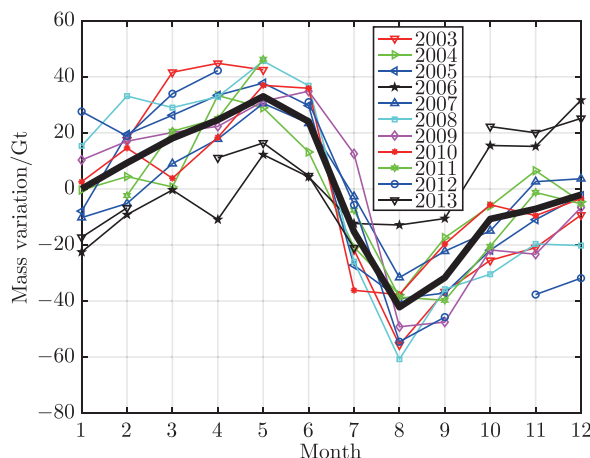


Figure 7.11 Mean true mass anomalies per calendar month in the numerical study, for the Northern (N) drainage system, \bar{m}^i (thick black curve). The thin curves represent monthly mass anomalies of individual years. The territory of Greenland was partitioned into 8 mascons.

Then, the RMS error of the mean mass anomalies per calendar month was computed as:

$$\text{RMS}_{\bar{m}} = \sqrt{\frac{\sum_{k=1}^5 \tau_k^2}{5}}. \quad (7.9)$$

The RMS error of the mean mass anomalies per calendar month, computed as total RMS error and as RMS error per error source is shown for different parameterizations in Fig. 7.12. Obviously, the use of data weighting results in a smaller total RMS error, as compared to the ordinary least-squares adjustment (i.e., ~ 6 Gt versus ~ 8 Gt for 23 mascons).

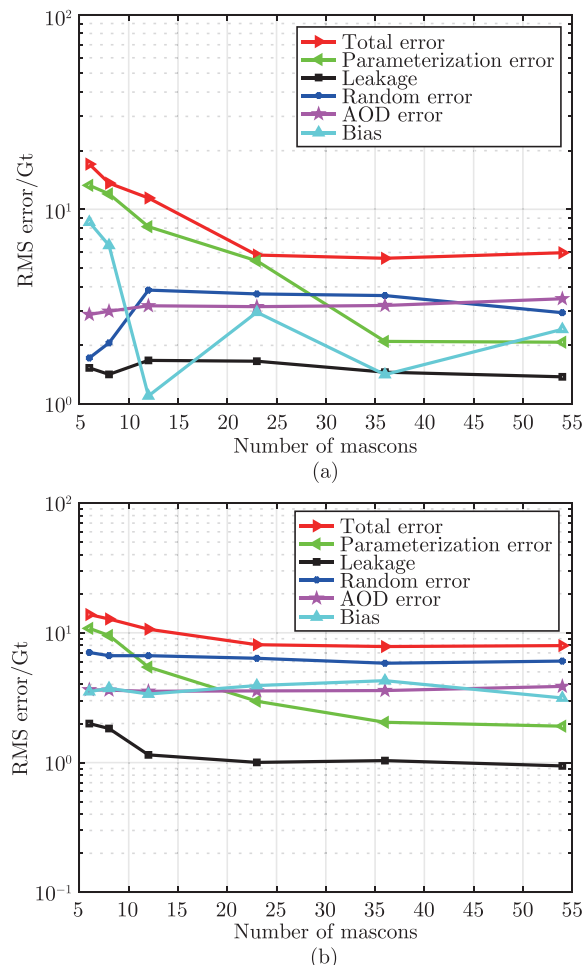


Figure 7.12 RMS error in mean mass anomalies per calendar month (in units of Gt) estimated with (a) and without (b) data weighting at the drainage system scale, as a function of the number of mascons.

mascons). In addition, statistical information (the RMS error and signal, as well as SNRs) is shown in Table 7.2. The highest SNRs (~ 6) are observed in the presence of data weighting, when the number of mascons is in the range of 23–54.

Table 7.2 The statistics of mean mass anomalies per calendar month estimated from synthetic data. The units are Gt

		Number of mascons					
		6	8	12	23	36	54
RMS errors	Yes	17.1	13.6	11.4	5.8	5.6	6.0
RMS errors	No	13.8	12.8	10.7	8.1	7.8	8.0
RMS of the true mass anomalies	—	31.0	31.9	31.0	33.1	33.1	34.6
SNR	Yes	1.8	2.3	2.7	5.7	5.9	5.8
SNR	No	2.2	2.5	2.9	4.1	4.2	4.3

As far as the RMS error per error source is concerned, we find that, regardless of whether data weighting is used or not, the parameterization error decreases as the number of mascons increases, while the other errors show a minor sensitivity to the number of mascons. For a small number of mascons, the parameterization error is the dominant error source, while for finer parameterizations, the random error becomes dominant. The intersection points of the two error types are between 23–36 mascons and between 8–12 mascons for the weighted and ordinary least-squares estimators, respectively.

7

From the above discussion, we conclude that the best mean mass anomalies per calendar month are obtained when Greenland is parameterized with 23–54 mascon and data weighting is switched on.

Recovery of monthly mass anomalies

In this section, we analyze the impact of the parameterization on the accuracy of the monthly mass anomaly estimates at the drainage system scale. We define the monthly mass anomalies as “the residual signal remaining after removing the trend and interannual variability”. We de-trend and remove the inter-annual variability from both the estimated and the true time series of monthly mass anomalies. The total RMS error and the RMS errors per error source are computed as the RMS difference between the two residual time series, i.e.,

$$\text{RMS} = \sqrt{\frac{\sum_{n=1}^N (m_n^{\text{recovered}} - m_n^{\text{true}})^2}{N}} \quad (7.10)$$

where m_n is the mass anomaly of month n and N is the number of months.

Fig. 7.13 shows the results. In the presence of data weighting, the total RMS error reaches a minimum of ~9 Gt when 23–54 mascons are used. Increasing the number of mascons does not increase the total RMS error, which is explained by the use of the

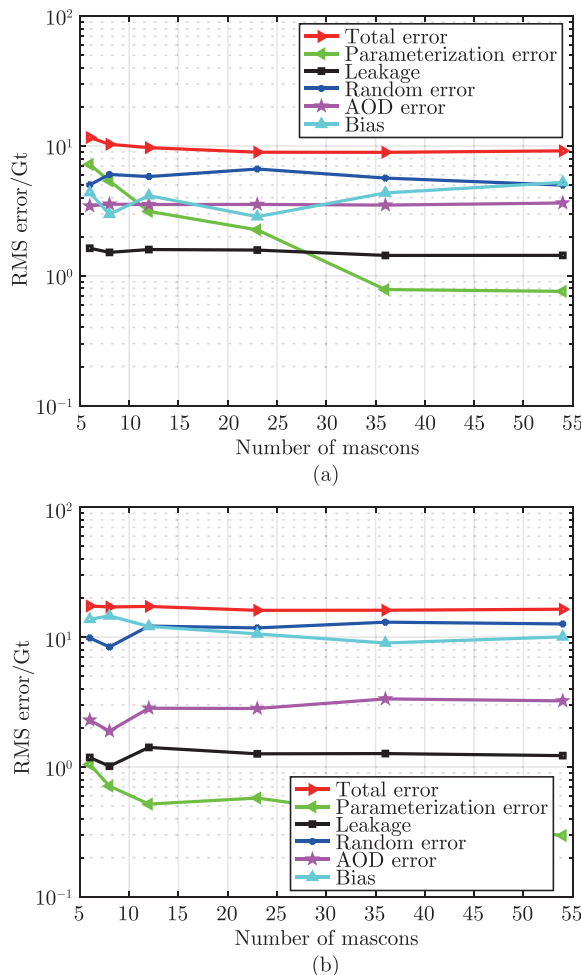


Figure 7.13 Total RMS error and RMS error per error source of monthly mass anomalies at the drainage system scale in units of Gt. Weighted least-squares estimator (a) versus ordinary least-squares estimator (b) as functions of the number of mascons.

spatial regularization. Without data weighting, the total RMS error stays at a stable level of ~ 17 Gt and is not sensitive to the number of mascons at all. In general, the total RMS error is $\sim 50\%$ smaller when data weighting is applied.

Table 7.3 shows that the SNR varies in a small range for the estimates obtained both with and without data weighting, reaching the maximum of 2.8 for the 23–54 mascons in the presence of data weighting. Fig. 7.14 shows the time-series estimated with data weighting in the 23-mascon case. Note that the $1-\sigma$ error bar is also shown. The results indicate that the monthly mass anomalies are in good agreement with the true signal at the drainage system scale, and even better when all of Greenland is considered.

Looking at the individual error sources, we see that the random error dominates the error budget in most cases. An exception is the estimates obtained in the 6-mascon case with data weighting, where the parameterization error plays the largest role. However, this error decreases rapidly as the number of mascons increases. The AOD error and the leakage error are negligible.

Table 7.3 The statistics of monthly mass anomalies estimated from synthetic data. The units are Gt

		Number of mascons					
		6	8	12	23	36	54
RMS errors	Yes	11.6	10.3	9.7	9.0	8.9	9.2
RMS errors	No	17.4	17.1	17.2	16.1	16.1	16.4
RMS of the true mass anomalies	—	23.1	24.0	25.7	24.6	25.1	25.8
SNR	Yes	2.0	2.3	2.6	2.8	2.8	2.8
SNR	No	1.3	1.4	1.5	1.5	1.6	1.6

7.4. Analysis based on real GRACE data

In this section, we investigate the impact of the parameterization on Greenland mass anomaly estimates based on real GRACE data. We use the RL05 GRACE monthly gravity field solutions from the Center for Space Research (CSR) at the University of Texas as input. Each solution is provided as a set of spherical harmonic coefficients, complete to degree 96, and comes with a full noise covariance matrix. The time interval considered is January 2003 – December 2013. Since data for 9 months were missing, the set consists of 123 months. Due to strong noise in the C_{20} coefficients, we replace them with available estimates based on satellite laser ranging (Cheng et al., 2013). The degree-one

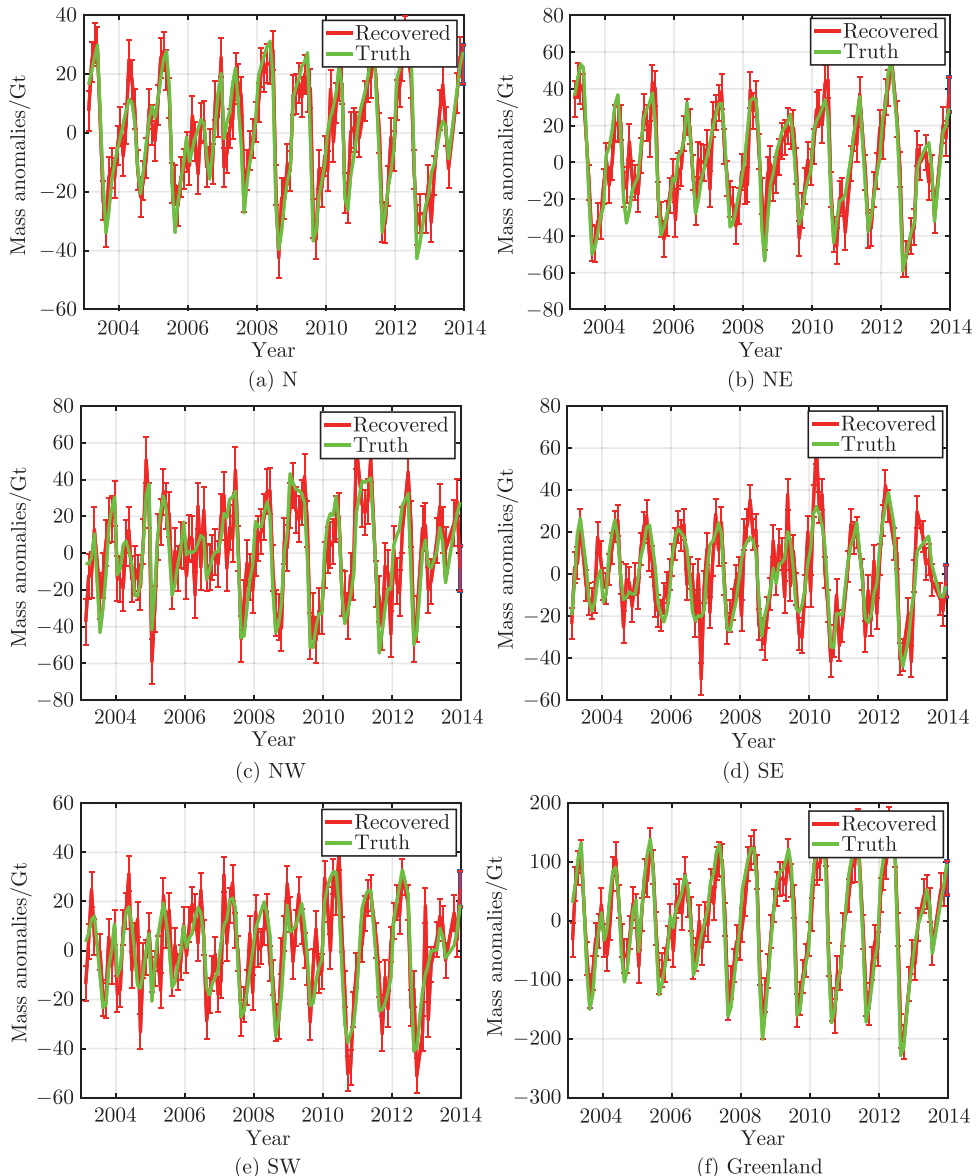


Figure 7.14 The regularized monthly mass anomaly time-series shown with $1-\sigma$ error bar and the “true” ones in the numerical study for each drainage system and for all of Greenland in the 23-mascon case. Data weighting is applied. Note that the trend and inter-annual variabilities are removed.

coefficients, which are missing in the GRACE products, are taken from Swenson et al. (2008). In addition, the GRACE solutions are corrected for Glacial Isostatic Adjustment

(GIA) using the model from A et al. (2013). For each parameterization, a time-series of mass anomalies per mascon is obtained with the optimal regularization factor, which is determined using the L-curve method (Hansen, 1992). These time-series are used as input for the further analysis.

7.4.1. Analysis of long-term linear trends

First, we study the impact of the parameterization on the long-term linear trend estimates at the drainage system scale. From the numerical study, we know that the trend estimates obtained using 23 mascons reach the highest level of quality. Therefore, this parameterization is used in our further analysis. First, we sum up the mass anomalies per mascon over each drainage system, and extract the linear trend, co-estimated with a bias, annual and semi-annual terms. The trend estimates obtained are presented in Table 7.4. The uncertainties are taken over from the numerical study. Next, we compare our trend estimates with similar estimates from the CSR mascon product (Save et al., 2016), which uses the same geometry of drainage systems. Note that the CSR mascon product is generated by incorporating spatial constraints in the form of a first-order Tikhonov regularization, while we use a much simpler zero-order Tikhonov regularization. Table 7.4 shows that our trend estimates for all drainage systems are in reasonably good agreement with the CSR estimates. The largest discrepancies (up to 15 Gt/yr) are observed for the N drainage system. We explain this by the use of a 120-km wide buffer zone in the preparation of the CSR mascon product (Save et al., 2016). This likely causes a signal leakage from nearby glaciers in Canada.

Table 7.4 The trend estimates based on real GRACE data in the case of 23 mascons at the drainage system scale. The uncertainties of estimates with and without data weighting are based on the numerical study. For comparison, the trends from CSR mascon product are also shown. The units are Gt/yr

Method	N	NW	NE	SW	SE
With data weighting	-9±11	-94±1	-18±3	-32±5	-83±6
Without data weighting	-10±11	-99±4	-24±6	-35±3	-95±1
CSR	-24	-92	-24	-32	-90

We then analyze the long-term trend estimates integrated over the whole of Greenland. We do not apply any regularization in this case to minimize the biases in the obtained estimates. The results are shown in Fig. 7.15. The estimates obtained both with and

without data weighting converge to a value of about -281 Gt/yr as the number of mascons increases. Interestingly, the sensitivity of the estimated trend to the chosen parameterization is much stronger when no data weighting is used; the estimate changes from -243 Gt/yr for 6 mascons to -281 Gt/yr for 54 mascons (15% difference). When data weighting is applied, the difference between the 6- and 54-mascon solutions is only 12 Gt/yr, or 4%. This result is consistent with the numerical study in Sect. 7.3.2 (cf. Fig. 7.8), demonstrating that data weighting indeed makes the trend estimates less sensitive to the dominant parameterization errors when the whole of Greenland is considered.

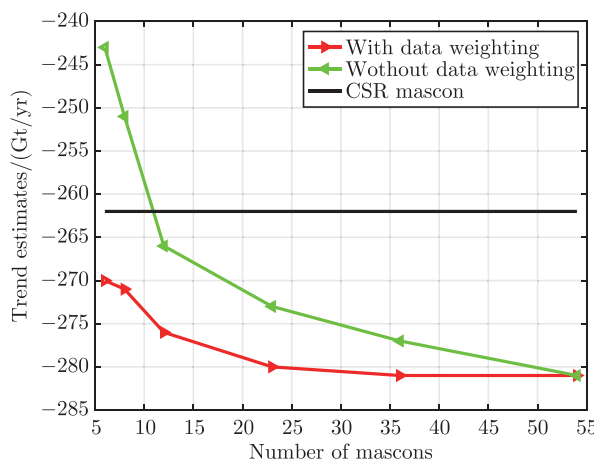


Figure 7.15 Mass anomaly trends over the period 2003–2013 in units of Gt/yr estimated with and without data weighting from real GRACE data and integrated over entire Greenland, as functions of the number of mascons.

In line with the synthetic study, we consider the trend estimate obtained with the largest number of mascons in the presence of data weighting as the most realistic and accurate one. This estimate, i.e., -281 ± 2 Gt/yr, is close to the estimates published in literature for the same period (i.e., 2003–2013): -280 ± 58 Gt/yr in (Velicogna et al., 2014) and -278 ± 19 Gt/yr in (Schrama et al., 2014). In addition, it is likely that the trend estimated by CSR mascon contains a bias (see Fig. 7.15). Note that the uncertainty of our trend estimate for the whole ice sheet is obtained as the root-sum-square of the individual error sources in the numerical study. However, there are also other errors that were not considered in the numerical study but may play a role in the context of real data processing (Ran et al., 2018b). These include uncertainties associated with the parameterization of the ocean regions around Greenland (i.e., the leakage of small ocean signals around Greenland), and the GIA. Taking all these uncertainties into account, we estimate the total error of

the trend estimate to be 11 Gt/yr.

7.4.2. Analysis of the estimates at the intermediate and short time scales

In addition, we investigate the impact of the parameterization on the other quantities of interest, i.e., inter-annual mass variations, mean mass anomalies per calendar month, and monthly mass anomalies. For this purpose, we compare the estimates from real GRACE data with the output of the RACMO2.3 model (Noël et al., 2015). In doing so, we assume that the ice discharge manifests itself in GRACE data as only a long-term trend, so that the remaining mass anomalies observed by GRACE are dominated by the SMB (Van den Broeke et al., 2009). Therefore, we de-trend the mass anomaly time-series from both GRACE and RACMO2.3 to make them comparable.

First, we examine the inter-annual mass variations. The corresponding RMS differences between GRACE and RACMO-based estimates are shown in Fig. 7.16 as a function of the number of mascons. To better understand the noise level, the RMS of the estimates are also shown for a comparison. The RMS differences decrease from 6 to 23 mascons, followed by a slight increase from 23 to 54 mascons. The best agreement with RACMO is obtained in the 23-mascon case when the data weighting is applied. All these findings are consistent with those based on the numerical study, indicating a realistic setup of the latter.

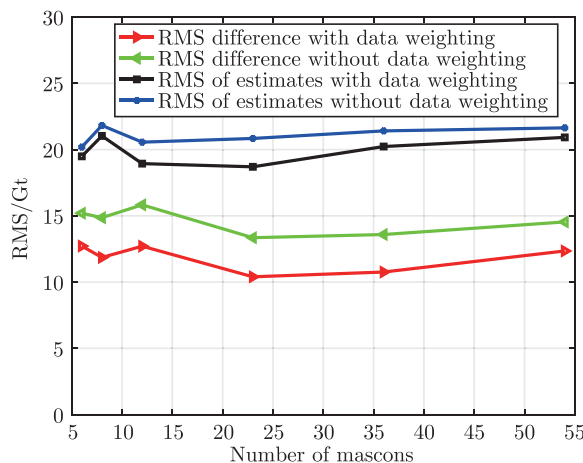


Figure 7.16 RMS differences (in units of Gt) between inter-annual mass variations from real GRACE data and from the RACMO2.3 output, as functions of the number of mascons. The RMS inter-annual mass variations themselves are also shown as a reference.

Next, the mean mass anomalies per calendar month are investigated. The RMS differences between the GRACE- and RACMO-based estimates are shown in Fig. 7.17. The RMS differences for 23–54 mascons are comparable, while they increase slightly as the number of mascon decreases from 23 to 6, no matter whether data weighting is applied or not. The data weighting scheme significantly reduces the RMS differences (by ~18%). All this is also in agreement with the numerical study.

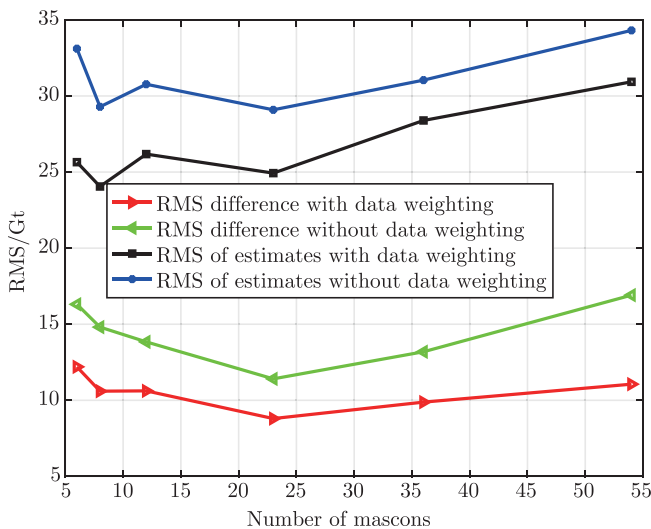


Figure 7.17 RMS difference (in units of Gt) between mean mass anomaly estimates per calendar month from real GRACE data and from the RACMO2.3 output, as functions of the number of mascons. The RMS mass anomalies themselves are also presented as a reference.

Furthermore, the monthly mass anomaly estimates are analyzed. Fig. 7.18 shows the RMS differences between the GRACE- and RACMO-based time-series at the drainage system scale. In absolute terms, the RMS differences without data weighting are about 15% larger than those obtained with data weighting. When using data weighting, the smallest RMS difference is observed with 36 mascons, while the smallest one is found with the 23 mascons without data weighting. However, the discrepancies of the RMS differences over various parameterizations are small, no matter whether data weighting is applied or not.

Finally, after removing the trends and accelerations, we compare our estimated time-series with the CSR mascon product (Save et al., 2016) and validate with independent data: SMB output from RACMO2.3. As discussed above, in general, the mass anomalies estimated with 23 mascons and data weighting are of the highest quality. Therefore, only

these mass anomalies are considered (see Fig. 7.19) in the comparison. The error bars in Fig. 7.19 are computed as root sum squared errors of two types: mean mass per calendar month and monthly mass anomalies, based on the numerical study. Note that the errors in the trend estimates are not included, because the time-series are de-trended. Next, the statistical analysis of the differences between the CSR mascon product and the RACMO-base estimates is performed. The RMS differences of inter-annual mass variations, mean mass anomalies per calendar month, and monthly mass anomalies are at a level comparable to that of our estimates, provided that the data weighting is applied (see Table 7.5).

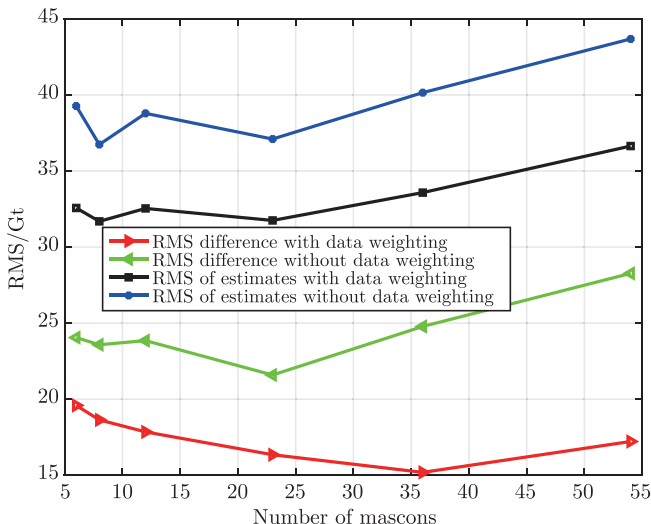


Figure 7.18 RMS difference (in units of Gt) between monthly mass anomalies from real GRACE data and from the RACMO2.3 output, as functions of the number of mascons. The RMS monthly mass anomalies themselves are also shown as a reference.

Table 7.5 The RMS differences between a GRACE solution and the RACMO2.3 output in terms of inter-annual mass variations mean mass anomalies per calendar month and monthly mass anomalies. The units are Gt

GRACE solution	RMS difference of inter-annual mass anomalies	RMS differences of mean mass per calendar month	RMS differences of monthly mass anomalies
This study (with data weighting)	9	10	16
This study (without data weighting)	11	13	22
CSR	9	11	15

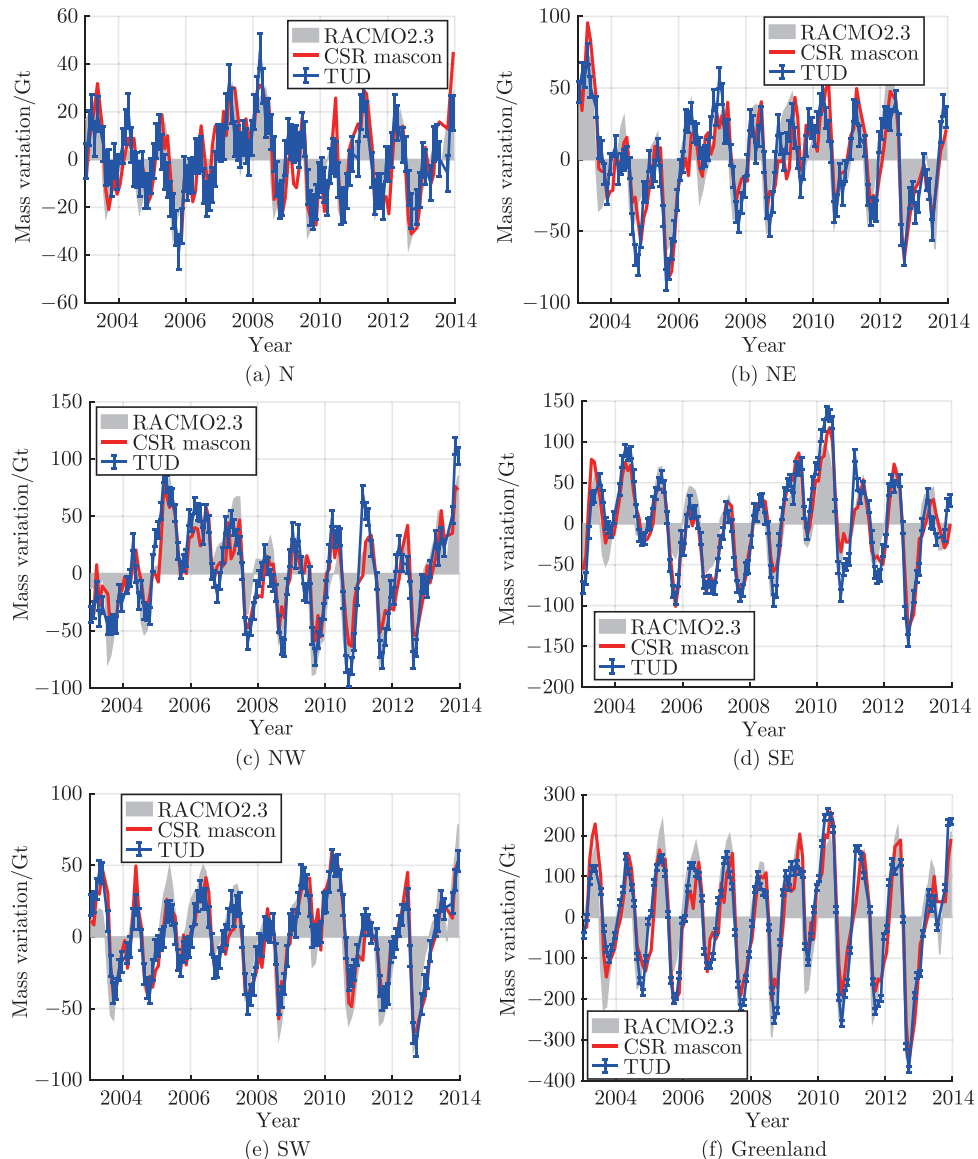


Figure 7.19 Mass anomaly time-series for each drainage system and for Greenland as a whole, estimated with data weighting in the case of 23 mascons. Note that the long-term linear trends are removed and the uncertainties ($1-\sigma$) are computed based on the numerical study.

7.5. Summary

In this study, we have analyzed the impact of the chosen parameterization on the mass anomaly estimates from GRACE data when the mascon approach with or without data weighting is applied. The zero-order Tikhonov regularization was applied in the data inversion. We analyzed the impact at different temporal scales by considering long-term linear trends, interannual mass variations, mean mass anomalies per calendar month, and time-series of monthly mass anomalies. Both synthetic and real GRACE data were considered.

In the simulation study, errors of four types (i.e., parameterization error, random error, leakage and AOD error) were simulated. In this way, we have found that the parameterization error and the random error, as well as the bias introduced by the regularization, are the major contributors to the total error budget of the estimates produced both with and without data weighting. For long-term linear trend estimates, the parameterization error is the dominant error type. This is due to a significant reduction in the random noise when estimating a linear trend by using a large number of monthly solutions as input. For inter-annual mass variations and mean mass per calendar month, the parameterization error dominates when the number of mascons is small; as the number of mascons increases, the random error takes over. For monthly mass anomalies, the random error is the most critical error type for almost all parameterizations. This is consistent with the fact that the use of data weighting (which is designed to suppress random noise) is effective in all the scenarios, except for the estimation of the long-term trend at the drainage system scale. The AOD error and the leakage error are small contributors to the total error budget, regardless of the temporal scales considered.

7

Remarkably, we find that the best estimates of the long-term linear trends integrated over the whole of Greenland are obtained when the number of mascons is large, while the regularization is not applied. This can be explained by the fact that random noise is subject to strong spatial correlations and is efficiently averaged out when the estimates are integrated over all of Greenland. On the other hand, the use of a large number of mascons suppresses the other important contributor to the error budget, i.e., the parameterization error. In this situation, the regularization is not advisable, since the bias introduced by the regularization is not compensated by a reduction in errors.

We have applied our findings to process real GRACE data. First, the long-term linear trend over the period 2003–2013 for all of Greenland is estimated to be around -281 Gt/yr .

This value is in good agreement with previous trend estimates in Velicogna et al. (2014) and Schrama et al. (2014). In the numerical study, we find that the estimates for all of Greenland suffer from only small errors (i.e., 0.8 Gt/yr with data weighting and 2 Gt/yr without data weighting). Note that the uncertainty of the trend estimates may be larger in reality, since there are other sources of error, e.g., GIA, sea level rise, etc.

We also consider the mass anomaly estimates at intermediate and short time scales using RMS differences between de-trended time-series from GRACE and from the RACMO2.3 model. These differences, as well as the results based on synthetic data, lead us to conclude that i) the optimal data weighting based on the full error covariance matrices of GRACE solutions is advisable and ii) the optimal way to parameterize the Greenland area is to divide it into 23 mascons (each with an area of $\sim 90,000 \text{ km}^2$). Smaller mascons may slightly worsen the estimation of inter-annual variability, while larger mascons yield inferior results in most of the cases considered (the latter can be explained by the impact of the parameterization errors). Similar recommendations apply also to the trend estimates at the drainage system scale, with the exception that the aforementioned optimal data weighting is not required.

8

Conclusions

The primary goal of this book is to continue the investigation of the Greenland ice sheet (GrIS) mass balance using multiple data sources. The main objectives are two folds: i) to develop a more accurate GRACE data processing scheme; ii) an illustrate the potential of combining GRACE-based mass estimates, ice discharge observations, and regional climate model output, complemented by simple physical constraints, to better understand the GrIS mass variations on different time scales. Improving the estimates of (the natural and forced) mass variations associated with individual processes is of key importance for robust projections of future GrIS mass changes and their contribution to sea level rise.

1. The variant of mascon approach proposed by Ran et al. (2018a) is summarized in this book. It can be considered as an improvement of the computational procedure proposed by Forsberg and Reeh (2007) and Baur and Sneeuw (2011). The approach consists of two main steps. In the first step, time series of gravity disturbances are computed using time series of GRACE spherical harmonic models. The data points are located at an average satellite altitude (here, 500 km), and are homogeneously distributed over an area including Greenland and a surrounding buffer zone. Importantly, instead of using scaled unit matrices to model the noise in the gravity disturbance as done in (Forsberg and Reeh, 2007; Baur and Sneeuw, 2011), we use full noise covariance matrices. In the second step, the synthesized gravity disturbances are used as observations to estimate mascon mass anomalies using weighted-least squares.
 - (a) The main methodological developments are the following.
 - We take into account the full-noise variance-covariance matrices C_d of gravity disturbances. They are propagated from the full-noise covariance matrices of the spherical harmonic coefficients using the law of covariance propagation. Since the matrices C_d appear to be ill-conditioned, with a gradually decreasing eigenvalue spectrum, we developed a methodology to approximately invert them.

- We develop refined parameterizations of all of Greenland, including equal-area mascons and taking into account the geometry of the coastline.
 - We develop an approach to achieve spectral consistency between data and model, and demonstrated its importance. Monthly GRACE solutions and gravity disturbances synthesized from these solutions are bandlimited to the maximum spherical harmonic degree. Mascons, however, are strictly spoken not bandlimited. Without making data and model spectrally consistent, the estimated mascons are biased toward zero, in particular when a weighted least-squares estimator is used with the inverse data noise covariance matrix as the weight matrix. The bias is more pronounced the more eigenvalues of the noise covariance matrix are retained when computing an approximate inverse.
- (b) Based on simulation experiments considering parameterization error, random error, leakage, and AOD error, a set of optimal data processing parameters has been selected for estimating mass anomalies of the GrIS over a one-year interval: this set comprises a buffer zone of 800 km, retaining the 600 largest eigenvalues of the noise covariance matrix when computing an approximate inverse, and using 23 mascons of about $90,000 \text{ km}^2$ each to parameterize all of Greenland. We also show that estimating monthly mass anomalies or a long-term linear trend requires a different set of processing parameters.
- (c) Using a weighted least-squares estimator, mass anomalies per mascon were estimated from CSR RL05 monthly GRACE solutions for the period February 2003 to December 2013. By integrating the mass anomalies per mascon over the whole of Greenland, the long-term linear trend of mass loss is estimated to be $-286 \pm 21 \text{ Gt/yr}$. This value is in agreement with previous estimates: $-280 \pm 58 \text{ Gt/yr}$ (Velicogna et al., 2014) for the period January 2003 to December 2013 and $-278 \pm 19 \text{ Gt/yr}$ (Schrama et al., 2014) for the period February 2003 to June 2013. We used a temporal regularization method of Ditmar et al. (2018) to evaluate the random noise level of the estimates per drainage system. In this way, we find that data weighting can suppress random noise by a factor of 1.5 to 3.0, depending on the drainage system.
- (d) The mass anomalies derived from GRACE include SMB and ice discharge. According to Van den Broeke et al. (2009), ice discharge manifests itself mostly as a long-term trend, while the seasonal mass variations are largely attributed to surface processes. Therefore, the seasonal SMB provided by the RACMO 2.3 model is used to validate seasonal signals estimated from

GRACE data. In particular, we use RACMO 2.3 to compare the weighted least-squares estimator with the ordinary least-squares estimator. We find that the former improves on the latter in the range of 24% to 47%, depending on the drainage system, while the improvement is small for all of Greenland. We explain the latter by a significant reduction of random errors, but also by the meltwater retention signal, which probably dominates the difference between GRACE-based and SMB-based mass anomalies for the whole of Greenland.

2. We analyze the Greenland mass budget at various temporal and spatial scales, by combining GRACE data, SMB model output, and ice discharge estimates from other data. This is new compared to previous studies, that focus on the GrIS, which covers only ~81% of Greenland's territory (the remaining 19% are tundra and isolated glaciers, which also contribute to the mass variations estimated with GRACE, especially on the intra-annual scale). We considered two different data sets of ice discharge estimates. The first set has already been presented in Enderlin et al. (2014). It was used to reconstruct the 2003–2012 multi-year mass trends and accelerations, as well as to separate the contributions of SMB and ice discharge, and covers 178 outlet glaciers with annual resolution. The second dataset, which is used to examine intra-annual variations in ice discharge, has been computed in this book and covers 55 marine-terminating glaciers with sub-annual resolution for the period 2009–2013. Ice discharge observations of these glaciers at the monthly scale are estimated by multiplying ice flow velocities (provided by Moon et al. (2014)) with ice thickness values (Morlighem et al., 2015). We perform the analysis at the drainage system scale. Similar to Van den Broeke et al. (2009), we divide Greenland into 5 drainage systems. We refer to these drainage systems as: (a) North (N); (b) Northwest (NW); (c) Southeast (SE); (d) Southwest (SW); and (e) Northeast (NE).
 - (a) According to RACMO 2.3, the SMB accumulates mass at a mean rate of 231 ± 122 Gt/yr over the period 2003–2012. In contrast to previous studies (Van den Broeke et al., 2009; Velicogna et al., 2014), we compute the absolute SMB accumulation and not a relative accumulation with respect to an assumed equilibrium over the period 1960–1990.
 - (b) We denote the difference between the non-detrended monthly GRACE- and SMB-based mass anomaly estimates as "Total-SMB" ("Total minus SMB"). The trend of Total-SMB is -508 ± 124 Gt/yr over the period 2003–2012, which is consistent with the ice discharge estimate of 520 ± 31 Gt/yr in Enderlin et al. (2014). By combining the GRACE-based estimates, the SMB model and the ice discharge, we closed the budget of the long-term trend of Greenland mass

variations. At the drainage system scale, the budget is closed except for the SE and N drainage systems. The misclosure is probably caused by deficiencies of RACMO 2.3, which overestimates precipitation in the SE drainage system and underestimates precipitation in the N drainage system.

- (c) We also close the budget of the long-term acceleration of mass variations over Greenland. Our estimates of accelerations in SMB-related ($-29.7 \pm 2.7 \text{ Gt/yr}^2$), ice discharge-related ($2.5 \pm 1.5 \text{ Gt/yr}^2$), and total ($-31.1 \pm 8.1 \text{ Gt/yr}^2$) mass anomalies are consistent: the residual does not exceed 1 Gt/yr^2 , which is well within the error bar. The two largest contributors to the observed acceleration are the SW and NW drainage systems.
 - (d) By analyzing the ice discharge on a monthly time scale, we find that the ice discharge in the NW drainage system shows a noticeable seasonal variation ($\sim 10\%$), while the seasonality of ice discharge in the SE drainage system is negligible.
 - (e) To analyze the mean annual cycle of total (GRACE) and cumulative SMB (RACMO2.3) mass anomalies over the period 2003–2013, we divide the entire period into 11 overlapping 13-month time intervals, each starting in December of the previous year and ending in December of the current year. Then, the mean mass anomaly for each calendar month is estimated by linear regression. A remarkable seasonal cycle is observed in the “Total-SMB” residuals, which can not be attributed to ice discharge, because the ice discharge can not be zero or could not increase in summer. We suggest that the seasonal variations of non-SMB mass anomalies (“Total-SMB”) may be caused by a delayed meltwater runoff. To estimate the instantaneous amount of meltwater subject to runoff, we fit the Total-SMB residuals in two periods before and after the flat feature (April-May and September-November) with a linear function. In this way, we find that meltwater is retained in Greenland between May and October, with a maximum in the month of July of about 100 Gt.
3. In order to understand the impact of the parameterization on the mass anomaly estimates, we perform a simulation study over the period 2003–2013. The signal is generated by combining the altimetry trend over the period 2003–2009 from ICESat and de-trended SMB mass anomalies from RACMO2.3. To make the simulation more realistic, all relevant error sources (i.e., parameterization error, leakage, AOD error, and random error) are taken into account. Thereafter, we do a similar analysis using real GRACE data. We find that the parameterization has a strong effect on the estimates at different temporal scales.
- (a) We have shown that the parameterization error and the random error are the

two main contributors to the total error budget of the estimates produced both with and without data weighting. An exception is the long-term linear trend estimates. Here, the parameterization error is the dominant error source for any number of mascons. We explain this by the fact that in this case the random noise is significantly reduced due to the large number of months used in the estimate. For the mean mass anomalies per calendar month, we find that the random error plays a major role only when the size of the mascons is small, while the parameterization error dominates when mascons of large size are used. For monthly mass anomalies, we find that the random error dominates the error budget when the number of mascons ranges from 8 to 54, while the parameterization error plays an important role only when 6 mascons are used. The AOD errors and the leakage are small for estimates at different temporal scales. Using real GRACE data, we find that most findings of the simulation study are confirmed.

- (b) We have shown that the optimal parameterization depends on the target. If one is interested in the long-term trend at the drainage system scale, a large number of mascons should be used in combination with the ordinary least-squares estimator. If the goal is to estimate long-term trend over all of Greenland, a large number of mascons and data weighting should be used. For mean mass variations per calendar month, we find that it is better to divide Greenland into 12–23 mascons in combination with data weighting. Finally, when the target are monthly mass anomalies, large-size mascons (e.g., 8 mascons) in combination with data weighting provide the best results.
4. The products released by different research groups—JPL, CSR, and GSFC—show noticeable discrepancies. To understand them, we compare these mascon products with mascon solutions computed in-house using a varying regularization parameter.
- (a) We show that the observed discrepancies are likely dominated by differences in the applied regularization. Furthermore, we present a numerical study aimed at an in-depth analysis of regularization-driven biases in the solutions.
- (b) We demonstrate that our simulations are able to reproduce 60%–80% of the biases observed in the real data, proving that our simulations are sufficiently realistic. After that, we demonstrate that the quality of mascon-based estimates can be improved by an appropriate modification of the applied regularization: no correlation between mascons is assumed when they belong to different drainage systems.
- (c) Using both simulations and real data analysis, we show that the improved

regularization mitigates signal leakage between drainage systems by 11%–56%. Finally, we validate various mascon solutions over the SW drainage system, using trends from i) the GOCO-06S model and (ii) the Input-Output Method as control data. In general, the in-house computed trend estimates are consistent with the trends from the CSR and JPL solutions and the trends from the control data.

Refererces

- A, G., Wahr, J., and Zhong, S. (2013). Computations of the viscoelastic response of a 3-d compressible earth to surface loading: An application to glacial isostatic adjustment in antarctica and canada. *Geophysical Journal International*, 192(2): 557–572.
- Baur, O. (2013). Greenland mass variation from time-variable gravity in the absence of GRACE. *Geophysical Research Letters*, 40(16): 4289–4293.
- Baur, O. and Sneeuw, N. (2011). Assessing Greenland Ice mass loss by means of point-mass modeling: A viable methodology. *Journal of Geodesy*, 85: 607–615.
- Beighley, R. E., Ray, R. L., He, Y., Lee, H., Schaller, L., Andreadis, K. M., Durand, M., Alsdorf, D. E., and Shum, C. K. (2011). Comparing satellite derived precipitation datasets using the hillslope river routing (hrr) model in the congo river basin. *Hydrological Processes*, 25(20): 3216–3229.
- Bettadpur, S. (2012). UTCSR Level-2 Processing Standards Document for Level-2 Product Release 0005, GRACE 32742, CSR Publ. GR-12-xx, Rev. 4.0, University of Texas at Austin. Technical report.
- Bevis, M., Harig, C., Khan, S. A., Brown, A., Simons, F. J., Willis, M., Fettweis, X., van den Broeke, M. R., Madsen, F. B., Kendrick, E., Caccamise, D. J., van Dam, T., Knudsen, P., and Nylen, T. (2019). Accelerating changes in ice mass within greenland, and the ice sheet's sensitivity to atmospheric forcing. *Proceedings of the National Academy of Sciences*, 116(6): 1934–1939.
- Bonin, J. and Chambers, D. (2013). Uncertainty estimates of grace inversion modeling technique over greenland using a simulation. *Geophysical Journal International*, 194: 212–229.
- Chandler, D., Wadham, J., Lis, G., Cowton, T., Sole, A., Bartholomew, I., Telling, J., Nienow, P., Bagshaw, E., Mair, D., et al. (2013). Evolution of the subglacial drainage system beneath the Greenland Ice Sheet revealed by tracers. *Nature Geoscience*, 6(3): 195–198.
- Chen, J., Rodell, M., Wilson, C., and Famiglietti, J. (2005). Low degree spherical harmonic influences on gravity recovery and climate experiment (grace) water storage estimates. *Geophysical Research Letters*, 32(14).
- Chen, J., Wilson, C., and Tapley, B. (2006). Satellite gravity measurements confirm accelerated melting of Greenland Ice Sheet. *Science (New York, N.Y.)*, 313: 1958–1960.
- Chen, J., Wilson, C., Tapley, B., and Grand, S. (2007). GRACE detects coseismic and postseismic deformation from the Sumatra-Andaman earthquake. *Geophysical Research Letters*, 34(13): PO.
- Cheng, M., Tapley, B., and Ries, J. (2013). Deceleration in earth's oblateness. *Journal of Geophysical Research: Solid Earth*, 118.
- Christensen, J. H., Christensen, O. B., Lopez, P., Van Meijgaard, E., and Botzet, M. (1996). The hirham4 regional atmospheric climate model. *DMI Scientific report*, 4: 51.
- Condi, F., Ries, J., and Tapley, B. (2004). The new grace gravity mission and its value to exploration. In *SEG Technical Program Expanded Abstracts 2004*, pages 728–729. Society of Exploration Geophysicists.
- Croteau, M. J., Loomis, B., Luthcke, S. B., and Nerem, R. S. (2014). Experiments with GRACE Global Mascon Solutions. In *AGU Fall Meeting Abstracts*, volume 2014, pages G33A–0416.

- Dahle, C., Flechtner, F., Gruber, C., König, D., König, R., Michalak, G., and Neumayer, K.-H. (2012). GFZ GRACE level-2 processing standards document for level-2 product release 0005. Technical report.
- Davis, C. H. (1998). Elevation Change of the Southern Greenland Ice Sheet. *Science*, 279(5359): 2086–2088.
- De Linage, C., Rivera, L., Hinderer, J., Boy, J.-P., Rogister, Y., Lambotte, S., and Biancale, R. (2009). Separation of coseismic and postseismic gravity changes for the 2004 sumatra-andaman earthquake from 4.6 yr of grace observations and modelling of the coseismic change by normal-modes summation. *Geophysical Journal International*, 176(3): 695–714.
- Ditmar, P., Teixeira da Encarnação, J., and Hashemi Farahani, H. (2012). Understanding data noise in gravity field recovery on the basis of inter-satellite ranging measurements acquired by the satellite gravimetry mission grace. *Journal of Geodesy*, 86(6): 441–465.
- Ditmar, P., Tangdamrongsub, N., Ran, J., & Klees, R. (2018). Estimation and reduction of random noise in mass anomaly time-series from satellite gravity data by minimization of month-to-month year-to-year double differences. *Journal of Geodynamics*, 119: 9–22.
- Dobslaw, H., Flechtner, F., Bergmann-Wolf, I., Dahle, C., Dill, R., Esselborn, S., Sasgen, I., and Thomas, M. (2013). Simulating high-frequency atmosphere-ocean mass variability for dealiasing of satellite gravity observations: AOD1B RL05. *Journal of Geophysical Research: Oceans*, 118(7): 3704–3711.
- Duan, X. J., Guo, J. Y., Shum, C. K., and van der Wal, W. (2009). On the postprocessing removal of correlated errors in GRACE temporal gravity field solutions. *Journal of Geodesy*, 83(11): 1095–1106.
- Enderlin, E. M., Howat, I. M., Jeong, S., Noh, M. J., van Angelen, J. H., and van den Broeke, M. R. (2014). An improved mass budget for the Greenland Ice Sheet. *Geophysical Research Letters*, 41(3): 866–872.
- Ettema, J., van den Broeke, M. R., van Meijgaard, E., van de Berg, W. J., Bamber, J. L., Box, J. E., and Bales, R. C. (2009). Higher surface mass balance of the Greenland Ice Sheet revealed by high-resolution climate modeling. *Geophysical Research Letters*, 36(12): L12501.
- Felikson D, Urban T J, Gunter B C, et al. (2017) Comparison of Elevation Change Detection Methods From ICESat Altimetry Over the Greenland Ice Sheet. *IEEE Transactions on Geoscience & Remote Sensing*, 55(10): 5494–5505.
- Fettweis, X., Gallée, H., Lefebvre, F., and Van Ypersele, J.-P. (2005). Greenland surface mass balance simulated by a regional climate model and comparison with satellite-derived data in 1990–1991. *Climate Dynamics*, 24(6): 623–640.
- Forsberg, R. and Reeh, N. (2006). Mass change of the Greenland Ice Sheet from grace. In *1st Meeting of the International Gravity Field Service: Gravity Field of the Earth*. Springer Verlag.
- Forsberg, R. and Reeh, N., editors (2007). *Mass change of the Greenland Ice Sheet from GRACE*, volume 73, Harita Dergisi, Ankara. Gravity Field of the Earth 1st meeting of the International Gravity Field Service.
- Forsberg, R., Sørensen, L., and Simonsen, S. (2017). Greenland and antarctica ice sheet mass changes and effects on global sea level. *Surveys in Geophysics*, 38(1): 89–104.
- Forster, R. R., van den Broeke, M. R., Miège, C., Burgess, E. W., van Angelen, J. H., Lenaerts, J. T.,

- Koenig, L. S., Paden, J., Lewis, C., Gogineni, S. P., et al. (2014). Extensive liquid meltwater storage in firn within the Greenland Ice Sheet. *Nature Geoscience*, 7(2): 95–98.
- Gent, P. R., Danabasoglu, G., Donner, L. J., Holland, M. M., Hunke, E. C., Jayne, S. R., Lawrence, D. M., Neale, R. B., Rasch, P. J., Vertenstein, M., Worley, P. H., Yang, Z. L., and Zhang, M. (2011). The community climate system model version 4. *Journal of Climate*, 24(19): 4973–4991.
- González, Á. (2010). Measurement of Areas on a Sphere Using Fibonacci and Latitude-Longitude Lattices. *Mathematical Geosciences*, 42(1): 49–64.
- Han, S.-C., Shum, C., Bevis, M., Ji, C., and Kuo, C. (2006). Crustal dilatation observed by grace after the 2004 sumatra-andaman earthquake. *Science (New York, N.Y.)*, 313: 658–662.
- Hansen, P. C. (1992). Analysis of discrete ill-posed problems by means of the l-curve. *SIAM review*, 34(4): 561–580.
- Heki, K. and Matsuo, K. (2010). Coseismic gravity changes of the 2010 earthquake in central chile from satellite gravimetry. *Geophys. Res. Lett.*, 37.
- Jacob, T., Wahr, J., Pfeffer, W., and Swenson, S. (2012). Recent contributions of glaciers and ice caps to sea level rise. *Nature*, 482: 514–518.
- Jekeli, C. (1981). Modifying Stokes' function to reduce the error of geoid undulation computations. *Journal of Geophysical Research*, 86(B8): 6985–6990.
- Joughin, I., Alley, R. B., and Holland, D. M. (2012). Ice-sheet response to oceanic forcing. *Science*, 338(6111): 1172–1176.
- Khan, S. A., Aschwanden, A., Bjørk, A. A., Wahr, J., Kjeldsen, K. K., and Kjaer, K. H. (2015). Greenland Ice Sheet mass balance: A review. *Reports on Progress in Physics*, 046801: 1–26.
- King, M., Howat, I., Candela, S., Noh, M.-J., Jeong, S., Noël, B., Van den Broeke, M., Wouters, B., and Negrete, A. (2020). Dynamic ice loss from the Greenland Ice Sheet driven by sustained glacier retreat. *Communications Earth & Environment*, 1(1): 1.
- Korona, J., Berthier, E., Bernard, M., Rémy, F., and Thouvenot, E. (2009). Spirit. spot 5 stereoscopic survey of polar ice: Reference images and topographies during the fourth international polar year (2007–2009). *ISPRS Journal of Photogrammetry and Remote Sensing*, 64(2): 204–212.
- Kvas, A., Brockmann, J. M., Krauss, S., Schubert, T., Gruber, T., Meyer, U., Mayer-Gürr, T., Schuh, W.-D., Jäggi, A., and Pail, R. (2021). Goco06s – a satellite-only global gravity field model. *Earth System Science Data*, 13(1): 99–118.
- Landerer, F. and Swenson, S. (2012). Accuracy of scaled grace terrestrial water storage estimates. *Water Resources Research*, 48: 4531.
- Larour, E., Seroussi, H., Morlighem, M., and Rignot, E. (2012). Continental scale, high order, high spatial resolution, ice sheet modeling using the ice sheet system model (issm). *Journal of Geophysical Research: Earth Surface*, 117(F1). F01022.
- Longuevergne, L., Scanlon, B. R., and Wilson, C. R. (2010). Grace hydrological estimates for small basins: Evaluating processing approaches on the high plains aquifer, usa. *Water Resources Research*, 46(11): W11517.
- Loomis, B., Luthcke, S., and Sabaka, T. (2019a). Regularization and error characterization of grace mascons. *Journal of Geodesy*, 93.
- Loomis, B., Richey, S., Arendt, A., Appana, R., Deweese, Y.-J., Forman, B., Kumar, S., Sabaka, T., and Shean, D. (2019b). Water storage trends in high mountain asia. *Frontiers in Earth Science*, 7:

- 235.
- Loomis, B., Rachlin, K., Wiese, D., Landerer, F., and Luthcke, S. (2020). Replacing grace/grace-fo c30 with satellite laser ranging: Impacts on antarctic ice sheet mass change. *Geophysical Research Letters*, 47.
- Luthcke, S., Zwally, H., Abdalati, W., Rowlands, D., Ray, R., Nerem, R., Lemoine, F., McCarthy, J., and Chinn, D. (2006a). Recent greenland ice mass loss by drainage system from satellite gravity observations. *Science (New York, N.Y.)*, 314: 1286–1289.
- Luthcke, S., Rowlands, D., Lemoine, F., Klosko, S., Chinn, D., and McCarthy, J. (2006b). Monthly spherical harmonic gravity field solutions determined from GRACE inter-satellite range-rate data alone. *Geophysical Research Letters*, 33(2): L02402.
- Luthcke, S., Sabaka, T., Loomis, B., Arendt, A., McCarthy, J., and Camp, J. (2013). Greenland and gulf of alaska land-ice evolution from an iterated grace global mascon solution. *Journal of Glaciology*, 59: 613–631.
- Mankoff, K., Solgaard, A., Colgan, W., Ahlstrøm, A., Khan, S., and Fausto, R. (2020). Greenland Ice Sheet solid ice discharge from 1986 through march 2020. *Earth System Science Data*, 12: 1367–1383.
- Miège, C., Forster, R. R., Brucker, L., Koenig, L. S., Solomon, D. K., Paden, J. D., Box, J. E., Burgess, E. W., Miller, J. Z., McNerney, L., Brautigam, N., Fausto, R. S., and Gogineni, S. (2016). Spatial extent and temporal variability of greenland firn aquifers detected by ground and airborne radars. *Journal of Geophysical Research: Earth Surface*, 121(12): 2381–2398.
- Moon, T., Joughin, I., Smith, B., and Howat, I. (2012). 21st-century evolution of Greenland outlet glacier velocities. *Science (New York, N.Y.)*, 336(6081): 576–578.
- Moon, T., Joughin, I., Smith, B., Van Den Broeke, M. R., Van De Berg, W. J., Noël, B., and Usher, M. (2014). Distinct patterns of seasonal Greenland glacier velocity. *Geophysical Research Letters*, 41(20): 7209–7216.
- Morlighem, M., Rignot, E., Mouginot, J., Seroussi, H., and Larour, E. (2015). Icebridge bedmachine greenland, version 2. *NASA DAAC at the National Snow and Ice Data Center, Boulder, Colorado, USA* (doi: 10.5067/AD7B0HQNSJ29).
- Mouginot, J., Rignot, E., Scheuchl, B., Fenty, I., Khazendar, A., Morlighem, M., Buzzi, A., and Paden, J. (2015). Fast retreat of zachariæ isstrøm, northeast greenland. *Science*, 350(6266): 1357–1361.
- Muller, P. M. and Sjogren, W. L. (1968). Mascons: lunar mass concentrations. *Science (New York, N.Y.)*, 161(3842): 680–684.
- Noël, B., van de Berg, W. J., van Meijgaard, E., Kuipers Munneke, P., van de Wal, R. S. W., and van den Broeke, M. R. (2015). Evaluation of the updated regional climate model racmo2.3: Summer snowfall impact on the Greenland Ice Sheet. *The Cryosphere*, 9(5): 1831–1844.
- Noël, B., van Kampenhout, L., Lenaerts, J., van de Berg, W., and Van Den Broeke, M. (2021). A 21st century warming threshold for sustained Greenland Ice Sheet mass loss. *Geophysical Research Letters*, 48(5): e2020GL090471.
- Panet, I., Mikhailov, V., Diament, M., Pollitz, F., King, G., De Viron, O., Holschneider, M., Biancale, R., and Lemoine, J.-M. (2007). Coseismic and post-seismic signatures of the sumatra 2004 december and 2005 march earthquakes in grace satellite gravity. *Geophysical Journal International*, 171: 177–190.

- Peltier, W., Argus, D., and Drummond, R. (2014). Space geodesy constrains ice age terminal deglaciation: The global ice-6g_c (vm5a) model. *Journal of Geophysical Research: Solid Earth*, 120(1): 450–487.
- Ramillien, G., Cazenave, A., and Brunau, O. (2004). Global time variations of hydrological signals from grace satellite gravimetry. *Geophysical Journal International*, 158(3): 813–826.
- Ramillien, G., Famiglietti, J., and Wahr, J. (2008). Detection of continental hydrology and glaciology signals from grace: A review. *Surveys in Geophysics*, 29: 361–374.
- Ran, J. (2017). Analysis of mass variations in greenland by a novel variant of the mascon approach.
- Ran, J., Ditmar, P., Klees, R., and Farahani, H. (2018a). Statistically optimal estimation of greenland ice sheet mass variations from grace monthly solutions using an improved mascon approach. *Journal of Geodesy*, 92(3): 299–319.
- Ran, J., Ditmar, P., and Klees, R. (2018b). Optimal mascon geometry in estimating mass anomalies within greenland from grace. *Geophysical Journal International*, 214(3): 2133–2150.
- Ran, J., Vizcaino, M., Ditmar, P., van den Broeke, M. R., Moon, T., Steger, C. R., Enderlin, E. M., Wouters, B., Noël, B., Reijmer, C. H., Klees, R., Zhong, M., Liu, L., and Fettweis, X. (2018c). Seasonal mass variations show timing and magnitude of meltwater storage in the Greenland Ice Sheet. *The Cryosphere*, 12(9): 2981–2999.
- Ran, J., Ditmar, P., Liu, L., Xiao, Y., Klees, R., and Tang, X. (2021). Analysis and mitigation of biases in Greenland Ice Sheet mass balance trend estimates from grace mascon products. *Journal of Geophysical Research: Solid Earth*, 126(7): e2020JB020880.
- Rennermalm, A. K., Smith, L. C., Chu, V., Box, J., Forster, R. R., Van den Broeke, M., Van As, D., and Moustafa, S. E. (2013). Evidence of meltwater retention within the Greenland Ice Sheet. *The Cryosphere*, 7: 1433–1445.
- Rodell, M., Famiglietti, J., Chen, J., Seneviratne, S., Viterbo, P., Holl, S., and Wilson, C. (2004). Basin scale estimate of evapotranspiration using grace and other observations. *Geophysical Research Letters*, 31.
- Rowlands, D. D., Luthcke, S. B., Klosko, S. M., Lemoine, F. G. R., Chinn, D. S., McCarthy, J. J., Cox, C. M., and Anderson, O. (2005). Resolving mass flux at high spatial and temporal resolution using GRACE intersatellite measurements. *Geophysical Research Letters*, 32(4): 1–4.
- Rowlands, D. D., Luthcke, S. B., McCarthy, J. J., Klosko, S. M., Chinn, D. S., Lemoine, F. G., Boy, J.-P., and Sabaka, T. J. (2010). Global Mass Flux Solutions from GRACE: A Comparison of Parameter Estimation Strategies - Mass Concentrations Versus Stokes Coefficients. *Journal of Geophysical Research Solid Earth*, 115(B1): 1–19.
- Sabaka, T., Rowlands, D., Luthcke, S., and Boy, J. P. (2010). Improving global mass flux solutions from gravity recovery and climate experiment (grace) through forward modeling and continuous time correlation. *Journal of Geophysical Research*, 115(B11).
- Sasgen, I., Martinec, Z., and Bamber, J. (2010). Combined grace and insar estimate of west antarctic ice mass loss. *J. Geophys. Res.*, 115(F4).
- Savcenko, R. and Bosch, W. (2010). EOT11a—Empirical ocean tide model from multi-mission satellite altimetry. Technical Report Report No 89.
- Save, H., Bettadpur, S., and Tapley, B. (2016). High resolution csr grace rl05 mascons. *Journal of Geophysical Research: Solid Earth*, 121(10), 7547–7569.

- Scanlon, B., Zhang, Z., Save, H., Wiese, D., Landerer, F., Long, D., Longuevergne, L., and Chen, J. (2016). Global evaluation of new grace mascon products for hydrologic applications. *Water Resources Research*, 52: 9412–9429.
- Schlegel, N.-J., Wiese, D. N., Larour, E. Y., Watkins, M. M., Box, J. E., Fettweis, X., and van den Broeke, M. R. (2016). Application of grace to the evaluation of an ice flow model of the Greenland Ice Sheet. *The Cryosphere Discussions*, 2016: 1–35.
- Schmidt, R., Schwintzer, P., Flechtner, F., Reigber, C., Güntner, A., Doell, P., Ramillien, G., Cazenave, A., Petrovic, S., Jochmann, H., and Wünsch, J. (2006). Grace observations of changes in continental water storage. *Global and Planetary Change*, 50: 112–126.
- Schrama, E. and Wouters, B. (2011). Revisiting Greenland Ice Sheet mass loss observed by grace. *J. Geophysical Research.*, 116(B2).
- Schrama, E., Wouters, B., and Rietbroek, R. (2014). A mascon approach to assess ice sheet and glacier mass balances and their uncertainties from grace data. *Journal of Geophysical Research: Solid Earth*, 119(7): 6048–6066.
- Selmes, N., Murray, T., and James, T. (2011). Fast draining lakes on the Greenland Ice Sheet. *Geophysical Research Letters*, 38(15): 116–119.
- Shepherd, A., Ivins, E., Aa, G., Barletta, V., Bentley, M., Bettadpur, S., Briggs, K., Bromwich, D., Forsberg, R., Galin, N., Horwath, M., Jacobs, S., Joughin, I., King, M., Lenaerts, J., Li, J., Ligtenberg, S., Luckman, A., Luthcke, S., and Zwally, H. (2012). A reconciled estimate of ice-sheet mass balance. *Science (New York, N.Y.)*, 338: 1183–1189.
- Siemes, C., Ditmar, P., Riva, R., Slobbe, D., Liu, X., and H. Farahani, H. (2013). Estimation of mass change trends in the earth's system on the basis of grace satellite data, with application to greenland. *Journal of Geodesy*, 87: 69–87.
- Simpson, M. J., Milne, G. A., Huybrechts, P., and Long, A. J. (2009). Calibrating a glaciological model of the Greenland Ice Sheet from the last glacial maximum to present-day using field observations of relative sea level and ice extent. *Quaternary Science Reviews*, 28(17): 1631–1657.
- Slater, D., Nienow, P., Cowton, T., Goldberg, D., and Sole, A. (2015). Effect of near terminus subglacial hydrology on tidewater glacier submarine melt rates. *Geophysical Research Letters*, 42(8): 2861–2868.
- Slobbe, D., Ditmar, P., and Lindenbergh, R. (2009). Estimating the rates of mass change, ice volume change and snow volume change in greenland from icesat and grace data. *Geophysical Journal International*, 176(1): 95–106.
- Sørensen, L., Simonsen, S. B., Nielsen, K., Lucas-Picher, P., Spada, G., Adalgeirsdottir, G., Forsberg, R., and Hvidberg, C. (2011). Mass balance of the Greenland Ice Sheet (2003–2008) from icesat data—the impact of interpolation, sampling and firn density. *The Cryosphere*, 5: 173–186.
- Stedinger, J. R. and Tasker, G. D. (1986). Regional hydrologic analysis, 2, model-error estimators, estimation of sigma and log-pearsong type 3 distributions. *Water Resources Research*, 22(10): 1487–1499.
- Stocker, T. F., Qin, D., Plattner, G.-K., Tignor, M., Allen, S. K., Boschung, J., Nauels, A., Xia, Y., Bex, V., and Midgley, P. M. (2013). Climate change 2013: The physical science basis. Technical report. 1535 pp.
- Sun, W., Okubo, S., Fu, G., and Araya, A. (2009). General formulations of global co-seismic

- deformations caused by an arbitrary dislocation in a spherically symmetric earth model—applicable to deformed earth surface and space-fixed point. *Geophysical Journal International*, 177: 817–833.
- Sun, Y., Ditmar, P., and Riva, R. (2016a). Observed changes in the earth's dynamic oblateness from grace data and geophysical models. *Journal of Geodesy*, 90(1): 81–89.
- Sun, Y., Riva, R., and Ditmar, P. (2016b). Optimizing estimates of annual variations and trends in geocenter motion and j_2 from a combination of grace data and geophysical models. *Journal of Geophysical Research: Solid Earth*, 121(11).
- Swenson, S. (2012). Grace monthly land water mass grids netcdf release 5.0. ver. 5.0. PO. DAAC, CA, USA. Dataset accessed [2016-12-01] at <http://dx.doi.org/10.5067/TELND-NC005>, 10.
- Swenson, S. and Wahr, J. (2006). Post-processing removal of correlated errors in GRACE data. *Geophysical Research Letters*, 33(8): L08402.
- Swenson, S., Chambers, D., and Wahr, J. (2008). Estimating geocenter variations from a combination of grace and ocean model output. *Journal of Geophysical Research*, 113(B8).
- Syed, T., Famiglietti, J., Rodell, M., Chen, J., and Wilson, C. (2008). Analysis of terrestrial water storage changes from grace and gldas. *Water Resources Research*, 44(2).
- Tapley, B. D., Bettadpur, S., Ries, J. C., Thompson, P. F., and Watkins, M. M. (2004). GRACE measurements of mass variability in the Earth system. *Science (New York, N.Y.)*, 305(5683): 503–505.
- Tapley, B. D., Watkins, M. M., Flechtner, F., Reigber, C., Bettadpur, S. V., Rodell, M., Sasgen, I., Famiglietti, J. S., Landerer, F. W., Chambers, D. P., Reager, J. T., Gardner, A. S., Save, H., Ivins, E. R., Swenson, S. C., Boening, C., Dahle, C., Wiese, D. N., Dobslaw, H., Tamisiea, M. E., and Velicogna, I. (2019). Contributions of grace to understanding climate change. *Nature Climate Change*, 9: 358–369.
- Thomas, R., Akins, T., Csatho, B., Fahnestock, M., Gogineni, P., Kim, C., and Sonntag, J. (2000). Mass balance of the Greenland Ice Sheet at high elevations. *Science*, 289(5478): 426–428.
- Thompson, P. F., Bettadpur, S., and Tapley, B. D. (2004). Impact of short period, non-tidal, temporal mass variability on GRACE gravity estimates. *Geophysical Research Letters*, 31(6): L06619.
- Tikhonov, A. (1963a). Regularization of incorrectly posed problems. *Soviet Math.*, 4: 1624–1627.
- Tikhonov, A. (1963b). Solution of incorrectly formulated problems and the regularization method. *Soviet Math. Dokl.*, 4: 1035–1038.
- Van Angelen, J., Van den Broeke, M., Wouters, B., and Lenaerts, J. (2014). Contemporary (1960–2012) evolution of the climate and surface mass balance of the Greenland Ice Sheet. *Surveys in geophysics*, 35(5): 1155–1174.
- van den Broeke, M., Bamber, J., Ettema, J., Rignot, E., Schrama, E., Berg, W., Meijgaard, E., Velicogna, I., and Wouters, B. (2009). Partitioning recent greenland mass loss. *Science (New York, N.Y.)*, 326: 984–986.
- van den Broeke, M. R., Enderlin, E. M., Howat, I. M., and Noël, B. P. (2016). On the recent contribution of the Greenland Ice Sheet to sea level change. *The Cryosphere*, 10(5): 1933.
- Velicogna, I. (2009). Increasing rates of ice mass loss from the Greenland and Antarctic ice sheets revealed by GRACE. *Geophysical Research Letters*, 36(19): L19503.
- Velicogna, I. and Wahr, J. (2005). Greenland mass balance from GRACE. *Geophysical Research*

- Letters*, 32(18): 1–4.
- Velicogna, I. and Wahr, J. (2006). Acceleration of greenland ice mass loss in spring 2004. *Nature*, 443: 329–331.
- Velicogna, I. and Wahr, J. (2013). Time-variable gravity observations of ice sheet mass balance: Precision and limitations of the grace satellite data. *Geophysical Research Letters*, 40(12): 3055–3063.
- Velicogna, I., Sutterley, T., and Van den Broeke, M. (2014). Regional acceleration in ice mass loss from greenland and antarctica using grace time-variable gravity data. *Geophysical Research Letters*, 41(22), 8130–8137.
- Velicogna, I., Mohajerani, Y., Aa, G., Landerer, F., Mouginot, J., Noël, B., Rignot, E., Sutterley, T., Van den Broeke, M., Wessem, J., and Wiese, D. (2020). Continuity of ice sheet mass loss in greenland and antarctica from the grace and grace follow-onmissions. *Geophysical Research Letters*, 47(8): e2020GL087291.
- Wahr, J., Molenaar, M., and Bryan, F. (1998). Time variability of the earth's gravity field: Hydrological and oceanic effects and their possible detection using grace. *Journal of Geophysical Research*, 103: 30205–30230.
- Wahr, J., Wingham, D., and Bentley, C. (2000). A method of combining icesat and grace satellite data to constrain antarctic mass balance. *Journal of Geophysical Research: Solid Earth*, 105(B7): 16279–16294.
- Wahr, J., Swenson, S., and Velicogna, I. (2006). Accuracy of GRACE mass estimates. *Geophysical Research Letters*, 33(6): L06401.
- Wang, L., Shum, C., Simons, F., Tapley, B., and Dai, C. (2012). Coseismic and postseismic deformation of the 2011 tohoku-oki earthquake constrained by grace gravimetry. *Geophysical Research Letters*, 39: 7301.
- Watkins, M., Wiese, D., Yuan, D., Boening, C., and Landerer, F. (2015). Improved methods for observing earth's time variable mass distribution with grace using spherical cap mascons. *Journal of Geophysical Research: Solid Earth*, 120(4): 2648–2671.
- Wiese, D. N. (2016). Grace monthly land water mass grids netcdf release 5.0.
- Wiese, D. N., Landerer, F. W., and Watkins, M. M. (2016). Quantifying and reducing leakage errors in the jpl rl05m grace mascon solution. *Water Resources Research*, 52(9): 7490–7502.
- Wingham, D., Ridout, A., Scharroo, R., Arthern, R., and Shum, C. (1998). Antarctic elevation change from 1992 to 1996. *Science*, 282(October): 1996–1999.
- Wouters, B., Chambers, D., and Schrama, E. (2008). Grace observes small-scale mass loss in greenland. *Geophysical Research Letters*, 35(20).
- Wouters, B., Bamber, J. L., van den Broeke, M. R., Lenaerts, J. T. M., and Sasgen, I. (2013). Limits in detecting acceleration of ice sheet mass loss due to climate variability. *Nature Geoscience*, 6(8): 613–616.
- Xu, G. (2010). *Sciences of Geodesy-I: Advances and Future Directions*. Springer Science & Business Media.
- Yi, S., Wang, Q., and Sun, W. (2016). Basin mass dynamic changes in China from grace based on a multibasin inversion method. *Journal of Geophysical Research: Solid Earth*, 121(5): 3782–3803.
- Zwally (2002). ICESat's laser measurements of polar ice, atmosphere, ocean and land.

- Journal of Geodynamics*, 34: 405–445.
- Zwally, H. J., Giovinetto, M. B., Beckley, M. A., and Saba, J. L. (2012). Antarctic and greenland drainage systems, gsfc cryospheric sciences laboratory. Available at ic.esat4.gsfc.nasa.gov/cryo_data/ant_grn_drainage_systems.php, 1: 2015.

A

Eigenvalue decomposition of the noise covariance matrix C_d

A statistically-optimal inversion of gravity disturbances into mass anomalies per mascon requires the inversion of the noise covariance matrix C_d . Since this matrix is ill-conditioned, some kind of regularization is required. Here, we use an eigenvalue decomposition

$$C_d = Q \Lambda Q^T. \quad (\text{A.1})$$

To minimize the loss of significant digits during the computations, we do not compute the noise covariance matrix explicitly but use the following procedure.

We start with Eq. (4.2) in matrix-vector form:

$$\mathbf{d} = \mathbf{F} \boldsymbol{\delta} \mathbf{p}, \quad (\text{A.2})$$

where the vector $\boldsymbol{\delta} \mathbf{p}$ includes the SHCs of a monthly GRACE solution (ΔC_{lm} , ΔS_{lm}), and \mathbf{F} is the matrix of the spherical harmonic synthesis that maps the SHCs into gravity disturbances. If the noise covariance matrix of the SHCs is C_{δ_p} and no constraints are applied when estimating the SHCs,

$$C_{\delta_p} = \mathbf{N}^{-1}, \quad (\text{A.3})$$

where \mathbf{N} is the normal matrix used in the computation of the SHCs from GRACE level-1b data. The Cholesky decomposition of this matrix is:

$$\mathbf{N} = \mathbf{L} \mathbf{L}^T. \quad (\text{A.4})$$

According to the law of covariance propagation, the noise covariance matrices C_{δ_p} and C_d are related to each other as

$$C_d = \mathbf{F} C_{\delta_p} \mathbf{F}^T. \quad (\text{A.5})$$

A substitution of Eqs. (A.3) and (A.4) in Eq. (A.5) gives

$$C_d = \mathbf{F} (\mathbf{L} \mathbf{L}^T)^{-1} \mathbf{F}^T = \mathbf{F} (\mathbf{L}^{-1})^T \mathbf{L}^{-1} \mathbf{F}^T = \mathbf{H} \mathbf{H}^T, \quad (\text{A.6})$$

where

$$\mathbf{H} = \mathbf{F} (\mathbf{L}^{-1})^T. \quad (\text{A.7})$$

Let

$$\mathbf{H} = \mathbf{U} \Sigma \mathbf{V}^T, \quad (\text{A.8})$$

be the SVD of the matrix \mathbf{H} , where Σ is the matrix of singular values, and \mathbf{U} and \mathbf{V} is the matrix of left and right singular vectors, respectively. Equation (A.8) and the equality

$$\mathbf{V}^T \mathbf{V} = \mathbf{I}, \quad (\text{A.9})$$

allow Eq. (A.6) to be re-written as

$$\mathbf{C}_d = \mathbf{U} \Sigma \mathbf{V}^T \mathbf{V} \Sigma^T \mathbf{U}^T = \mathbf{U} \Sigma \Sigma^T \mathbf{U}^T. \quad (\text{A.10})$$

It is easy to see that $\Sigma \Sigma^T$ is a square diagonal matrix with elements λ_i defined as

$$\lambda_i = \sigma_i^2 \quad (i = 1, \dots, N_d), \quad (\text{A.11})$$

where σ_i are the singular values forming the matrix Σ and N_d is the number of data points. Therefore, the representation of the matrix \mathbf{C}_d given by Eq. (A.10) satisfies the properties of the eigendecomposition, so that λ_i are the eigenvalues of \mathbf{C}_d ,

$$\mathbf{Q} = \mathbf{U}, \quad \text{and} \quad \mathbf{\Lambda} = \Sigma \Sigma^T. \quad (\text{A.12})$$

Thus, the operations prescribed by Eqs. (A.4), (A.7), (A.8), and (A.12) provide the eigenvalue decomposition of the matrix \mathbf{C}_d without the need to compute this matrix explicitly.

In order to demonstrate the superior stability of the proposed computational procedure, we perform the following experiment. We use the normal equation matrix for the monthly GRACE solution of August 2006 from DMT. We explicitly compute the noise covariance matrix \mathbf{C}_d and perform an eigenvalue decomposition of this matrix. Alternatively, we follow the procedure outlined above. Fig. A.1 shows the eigenvalues of \mathbf{C}_d for both procedures. The direct computation of the eigenvalues of \mathbf{C}_d provides only the first 900 eigenvalues. The flattening of the eigenvalue spectrum beyond an index of about 900 is caused by numerical roundoff errors, and is at the level of the largest eigenvalue times machine epsilon for IEEE double precision arithmetic. Using the proposed procedure, the first 1,400 eigenvalues can be computed before numerical roundoff errors become dominant. From this, we conclude that the proposed procedure is numerically more stable, and therefore better suited to deal with ill-conditioned noise covariance matrices when computing a weighted least-squares solution.

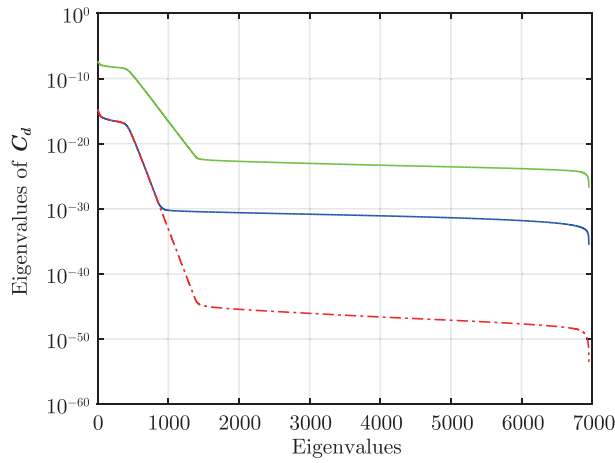


Figure A.1 Eigenvalues of the matrix C_d computed directly (blue) and using the procedure suggested in this book (red). The singular values of the matrix H are shown in green.

B

Robustness of GRACE-based estimates at the intra-annual time scale

In this appendix, we investigate the robustness of GRACE-based estimates of mass anomalies on the intra-annual time scale. In this way, we want to understand to what extent they can be interpreted as signal or noise. The mean annual cycle of the “Total-SMB” differences shows three periods of almost null month-to-month variations (nearly flat segments in Fig. 5.11): February–March, May–July, and November–December. If we assume that the main contributor to Total-SMB variations is ice discharge, these flat features are unphysical: ice discharge cannot stop. Therefore, they should be explained either by meltwater retention or by errors in the RACMO2.3 and GRACE-based estimates.

To assess the possible impact of errors in RACMO2.3 and in GRACE-based mass anomalies, we estimate mass anomalies from GRACE data using different processing parameters. These include: i) using a weighted least-squares estimator with the inverse of the noise covariance matrix \mathbf{C}_d as the weight matrix or using the ordinary least-squares estimator; ii) retaining a different number of eigenvalues of \mathbf{C}_d when computing a weighted least-squares estimate of the mass anomalies (i.e., 200, 400 and 600 eigenvalues, respectively); iii) a different handling of the surrounding ocean (i.e., parameterization with one patch, parameterization with four patches (cf. Fig. B.1), and no parameterization, respectively); iv) a different choice of spherical harmonic degree-one coefficients (i.e., from Swenson et al. (2008), Cheng et al. (2013), and Sun et al. (2016a), respectively). Note that only one parameter varies at a time, while the other parameters are defined as in the primary data processing scheme. To make the investigation more comprehensive, we also compare the Total-SMB annual cycles derived from different GRACE-based estimates (i.e., the estimates computed in this book, from Wouters et al. (2008), and from Watkins et al. (2015), respectively).

The results are shown in Figs. B.1–B.5. Obviously, the presence and appearance of the quasi-null Total-SMB monthly variations during February–March and November–December vary from case to case. For example, when the surrounding ocean is parameterized with four patches, the February–March feature becomes less flat; when using an ordinary least-squares estimator, the November–December flat feature is not significant either, similar to the estimates of Wouters et al. (2008). The flat features of February–March and November–December do not appear in the Total-SMB differences obtained with the JPL mascon solutions of Watkins et al. (2015). On the other hand, the flat feature of May–July persists, no matter what processing parameters are chosen and which GRACE product is used. Therefore, we suggest that the May–June feature is not triggered by noise in the estimates, but is likely physical. Most likely, this signal is caused by meltwater retention.

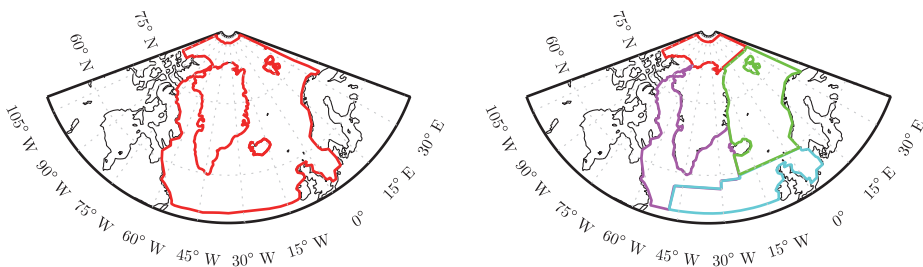
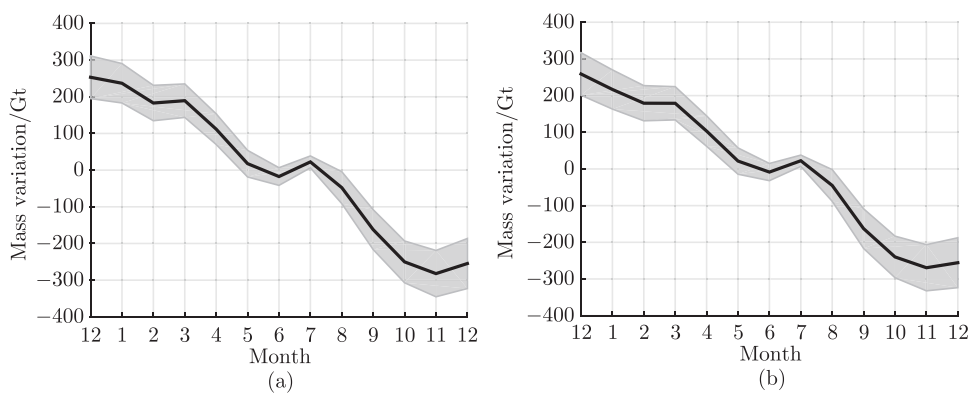


Figure B.1 Parameterization of the ocean area around Greenland with one (left) and four (right) patches.



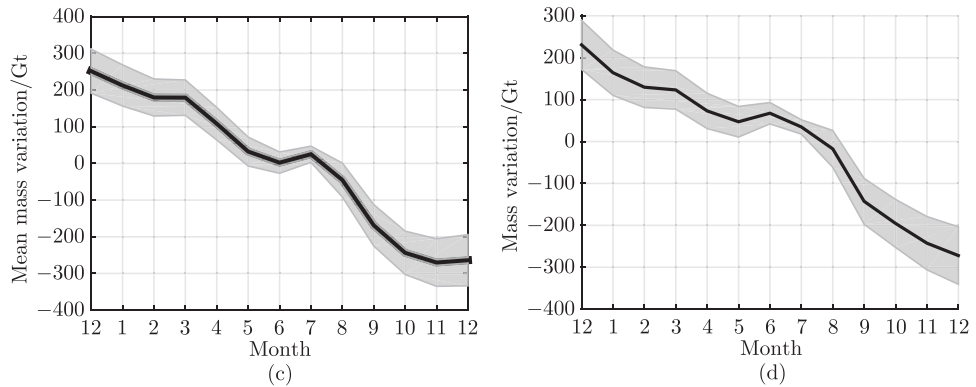


Figure B.2 Mean annual cycle of “Total-SMB” mass anomalies estimated using different approaches to data weighting and the matrix C_d inversion: data weighting based on matrix C_d , retaining 200 (a), 400 (b), or 600 (c) eigenvalues; no data weighting (d).

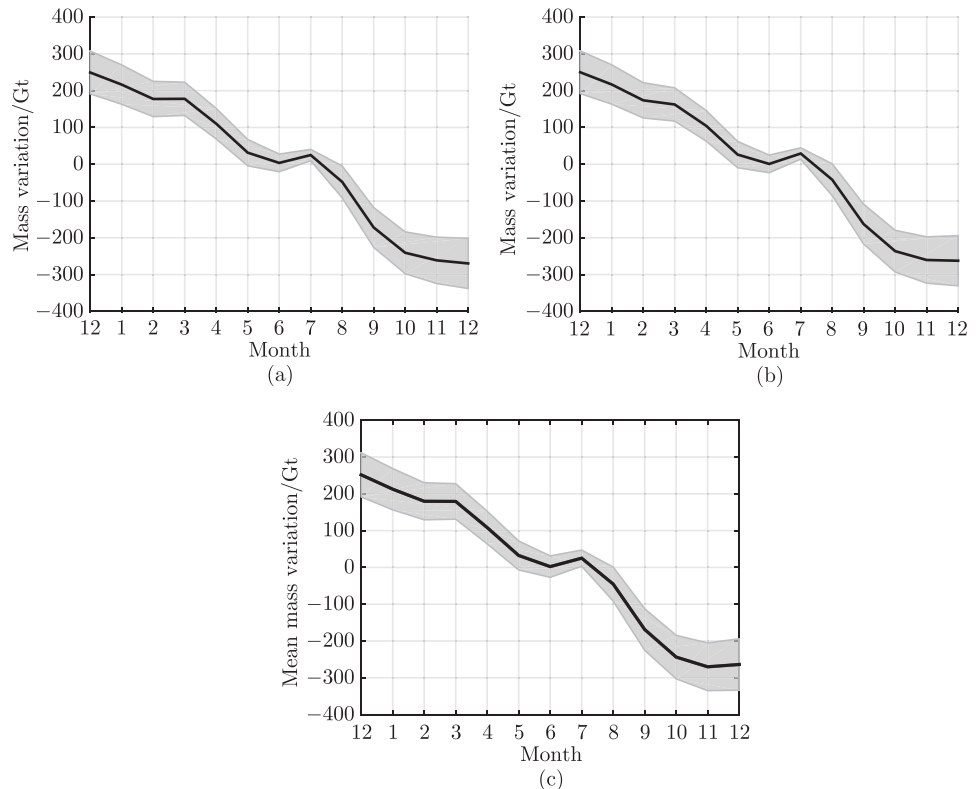


Figure B.3 Mean annual cycle of “Total-SMB” mass anomalies estimated using different parameterizations of the ocean surrounding the GrIS: one patch (a), four patches (b), and no parameterization (c).

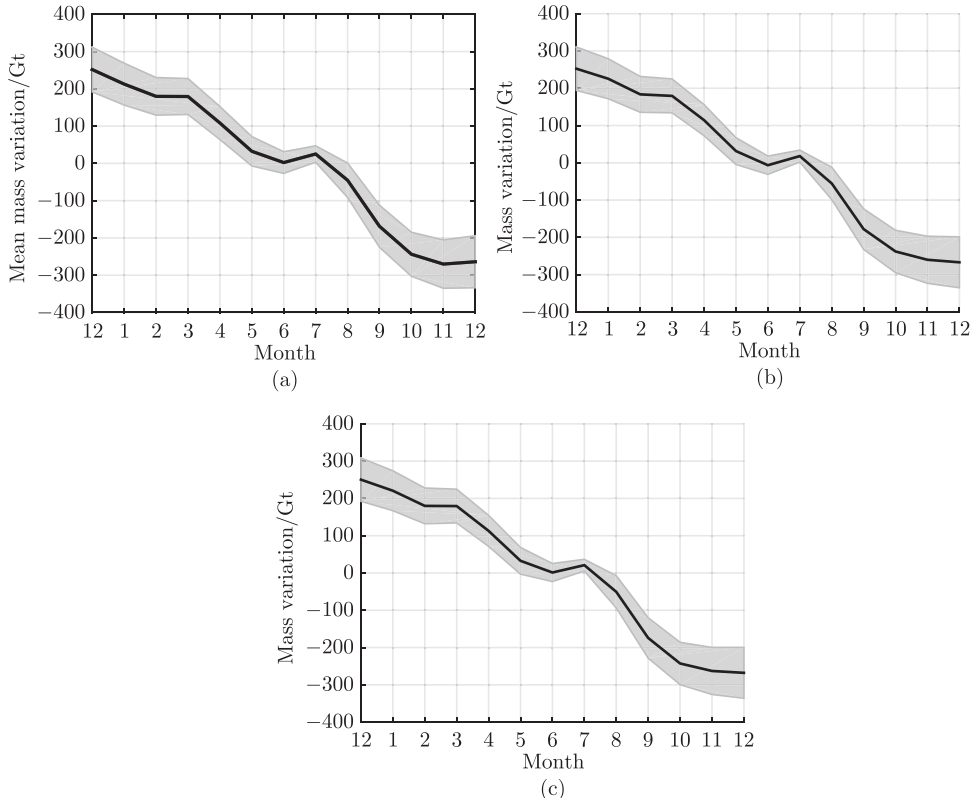


Figure B.4 Mean annual cycle of "Total-SMB" mass anomalies estimated with different degree-one coefficients: from Swenson et al. (2008) (a), Cheng et al. (2013) (b), Sun et al. (2016a) (c).

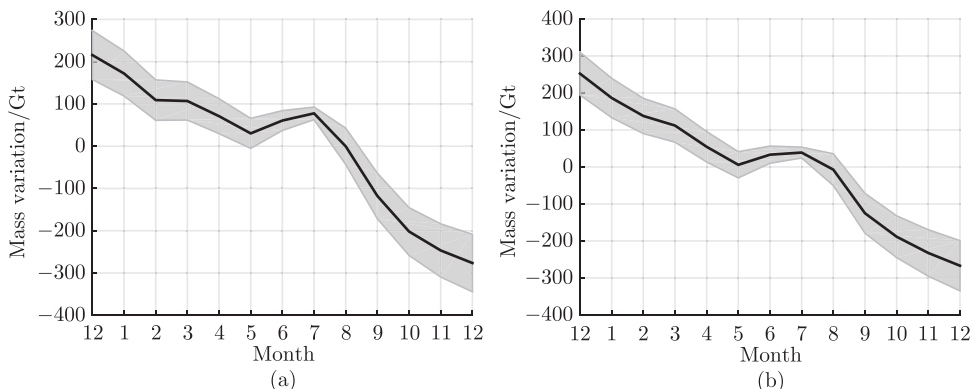


Figure B.5 Mean annual cycle of "Total-SMB" mass anomalies using the GRACE-based mass anomalies from Wouters et al. (2008) (a) and Watkins et al. (2015) (b).

C

Supporting Information for Chapter 6

According to Tikhonov (1963a) and (1963b), after introducing $g(\varphi, \lambda)$ as a continuous analog of the unknown vector x (where φ and λ are the latitude and longitude on a spherical surface Ω_a), the general form of the regularization functional $\Phi(x)$ can be written as

$$\Phi(x) = \int_{\Omega_a} \left[\kappa_0(\varphi, \lambda) g^2(\varphi, \lambda) + \kappa_1(\varphi, \lambda) (\nabla g(\varphi, \lambda))^2 + \dots + \kappa_n(\varphi, \lambda) (\nabla^n g(\varphi, \lambda))^2 \right] d\Omega_a \quad (C.1)$$

where ∇ is the surface gradient operator; $\kappa_0(\varphi, \lambda), \kappa_1(\varphi, \lambda), \dots, \kappa_n(\varphi, \lambda)$ are prior non-negative functions; and index n defines the order of the Tikhonov regularization. Obviously, the general form of the regularization functional given by Eq. C.1 leaves a lot of freedom and, therefore, requires further specification. In practice, the regularization functional typically contains the derivative of only one chosen order, e.g., the zero order or the first order. Furthermore, the associated function $\kappa_n(\varphi, \lambda)$ is assumed to be constant, so that it gets absorbed by the regularization parameter a . Then, the practical definition of the zero-order Tikhonov regularization functional becomes:

$$\Phi_0(x) = \int_{\Omega_a} g^2(\varphi, \lambda) d\Omega_a \approx \sum_i \sum_k x_i R_{i,k} x_k = \mathbf{x}^T \mathbf{R} \mathbf{x} \quad (C.2)$$

where x_i and x_k are the i - and k -th elements of the vector x , respectively; and $R_{i,k}$ is an element of the zero-order Tikhonov regularization matrix with entries defined as follows:

$$R_{i,k} = \begin{cases} \text{area}_i & i = k \\ 0 & i \neq k \end{cases} \quad (C.3)$$

Table C.1 Leakage of trend signal from the NW drainage system to other drainage systems caused by regularization. Signals in the other drainage systems are set equal to 0.

	N	NW	NE	SW	SE
Trend recovered with $\alpha = 10^{-25}$ (Gt/yr)	1.56	-146.58	-0.18	-1.78	0.03
Trend recovered with $\alpha = 10^{-24}$ (Gt/yr)	3.47	-136.72	-6.60	-4.44	2.03
True trend (Gt/yr)	0.00	-148.04	0.00	0.00	0.00
Bias for $\alpha = 10^{-25}$ (Gt/yr)	1.56	1.46	-0.18	-1.78	0.03
Bias for $\alpha = 10^{-24}$ (Gt/yr)	3.47	11.32	-6.60	-4.44	2.03
Relative bias (Gt/yr)	1.92	9.86	-6.42	-2.66	2.00

Table C.2 The same as Table C.1, but for the SW drainage system.

	N	NW	NE	SW	SE
Trend recovered with $\alpha = 10^{-25}$ (Gt/yr)	-0.26	0.77	0.22	-20.44	-1.55
Trend recovered with $\alpha = 10^{-24}$ (Gt/yr)	-0.18	-0.20	-0.12	-16.09	-4.45
True trend (Gt/yr)	0.00	0.00	0.00	-21.27	0.00
Bias for $\alpha = 10^{-25}$ (Gt/yr)	-0.26	0.77	0.22	0.84	-1.55
Bias for $\alpha = 10^{-24}$ (Gt/yr)	-0.18	-0.20	-0.12	5.19	-4.45
Relative bias (Gt/yr)	0.08	-0.97	-0.34	4.35	-2.90

Table C.3 The same as Table C.1, but for the SE drainage system.

	N	NW	NE	SW	SE
Trend recovered with $\alpha = 10^{-25}$ (Gt/yr)	-0.06	4.10	-0.66	-2.83	-99.03
Trend recovered with $\alpha = 10^{-24}$ (Gt/yr)	-0.35	3.75	-2.62	-9.86	-88.96
True trend (Gt/yr)	0.00	0.00	0.00	0.00	-99.00
Bias for $\alpha = 10^{-25}$ (Gt/yr)	-0.06	4.10	-0.66	-2.83	-0.03
Bias for $\alpha = 10^{-24}$ (Gt/yr)	-0.35	3.75	-2.62	-9.86	10.04
Relative bias (Gt/yr)	-0.28	-0.34	-1.96	-7.02	10.07

where, $area_i$ is the area of mascon i. Similarly, the first-order Tikhonov regularization functional is defined as:

Table C.4 The same as Table C.1, but for the N drainage system.

	N	NW	NE	SW	SE
Trend recovered with $\alpha = 10^{-25}$ (Gt/yr)	-19.09	-0.45	0.27	-0.13	0.08
Trend recovered with $\alpha = 10^{-24}$ (Gt/yr)	-16.63	-1.42	-0.25	-0.16	0.11
True trend (Gt/yr)	-19.70	0.00	0.00	0.00	0.00
Bias for $\alpha = 10^{-25}$ (Gt/yr)	0.61	-0.45	0.27	-0.13	0.08
Bias for $\alpha = 10^{-24}$ (Gt/yr)	3.07	-1.42	-0.25	-0.16	0.11
Relative bias (Gt/yr)	2.46	-0.97	-0.52	-0.04	0.03

Table C.5 The same as Table C.1, but for the NE drainage system.

	N	NW	NE	SW	SE
Trend recovered with $\alpha = 10^{-25}$ (Gt/yr)	-0.81	3.37	10.95	0.27	-0.56
Trend recovered with $\alpha = 10^{-24}$ (Gt/yr)	0.44	6.34	9.91	-0.03	-0.90
True trend (Gt/yr)	0.00	0.00	13.41	0.00	0.00
Bias for $\alpha = 10^{-25}$ (Gt/yr)	-0.81	3.37	-2.45	0.27	-0.56
Bias for $\alpha = 10^{-24}$ (Gt/yr)	0.44	6.34	-3.50	-0.03	-0.90
Relative bias (Gt/yr)	1.25	2.97	-1.04	-0.30	-0.34

$$\Phi_1(x) = \int_{\Omega_a} (\nabla g(\varphi, \lambda))^2 d\Omega_a \quad (C.4)$$

For the chosen panelization of the GrIS with mascons, the technical implementation of Eq. S4 is described in Sect. 6.2.2, see also Table. 6.1.

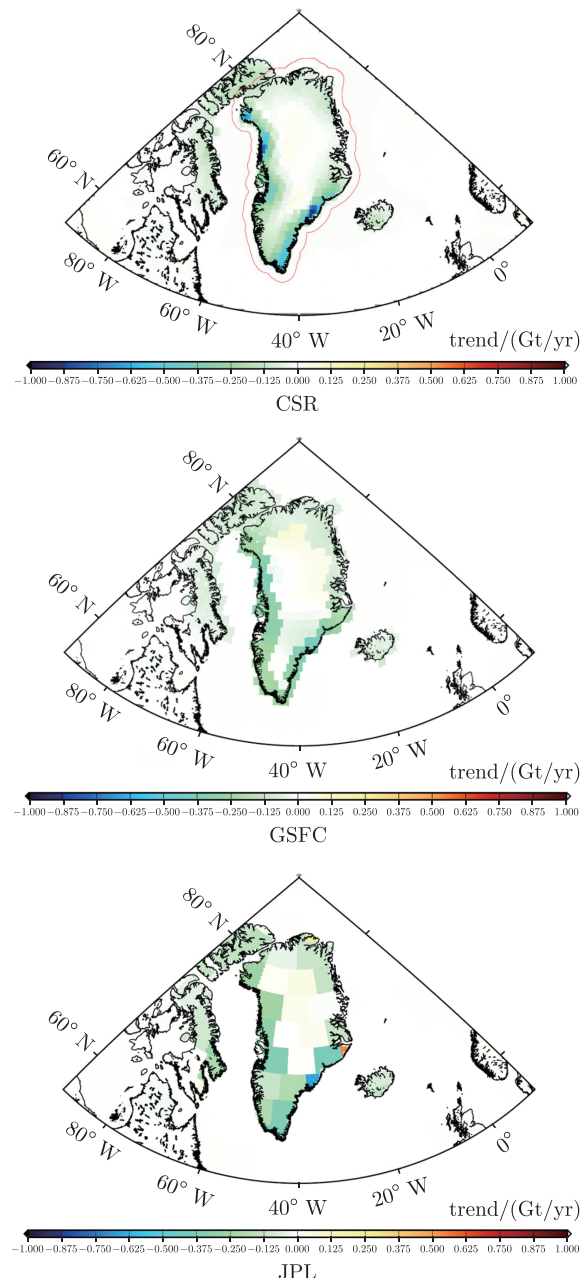


Figure C.1 The spatial pattern of estimated trends over 2003–2014 from different mascon products. The units are Gt/yr.

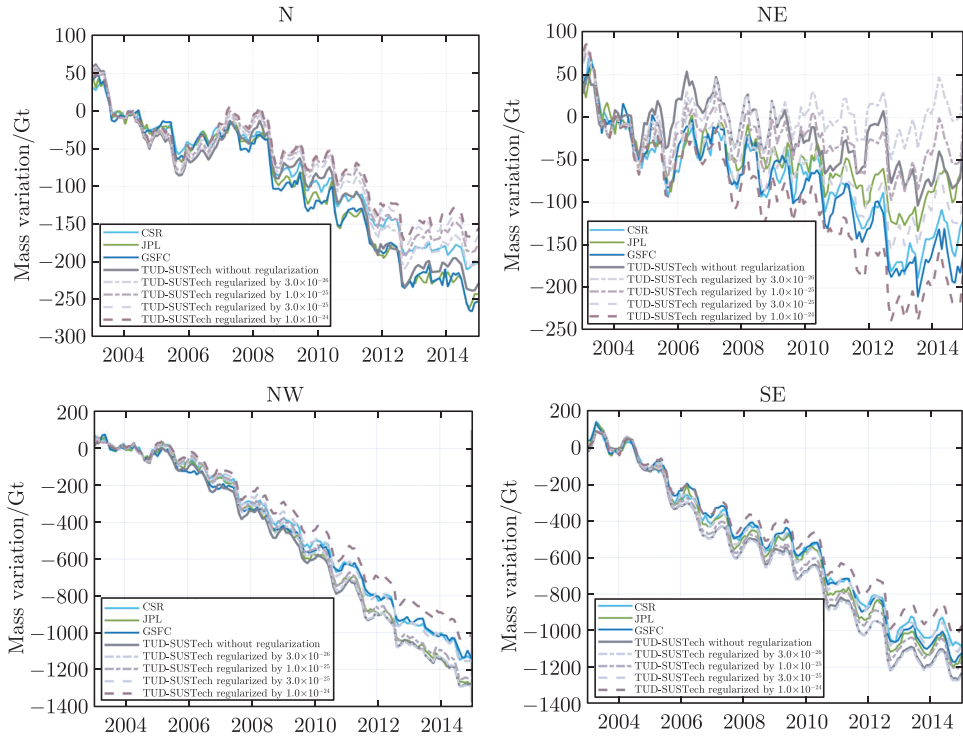


Figure C.2 Similar to Fig. 6.3, but for the N, NE, NW, and SE drainage systems.

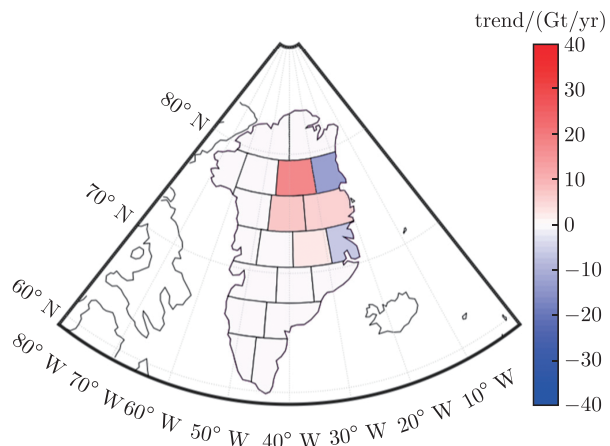


Figure C.3 Spatial pattern of the estimated trend in the NE drainage system. The units are Gt/yr.

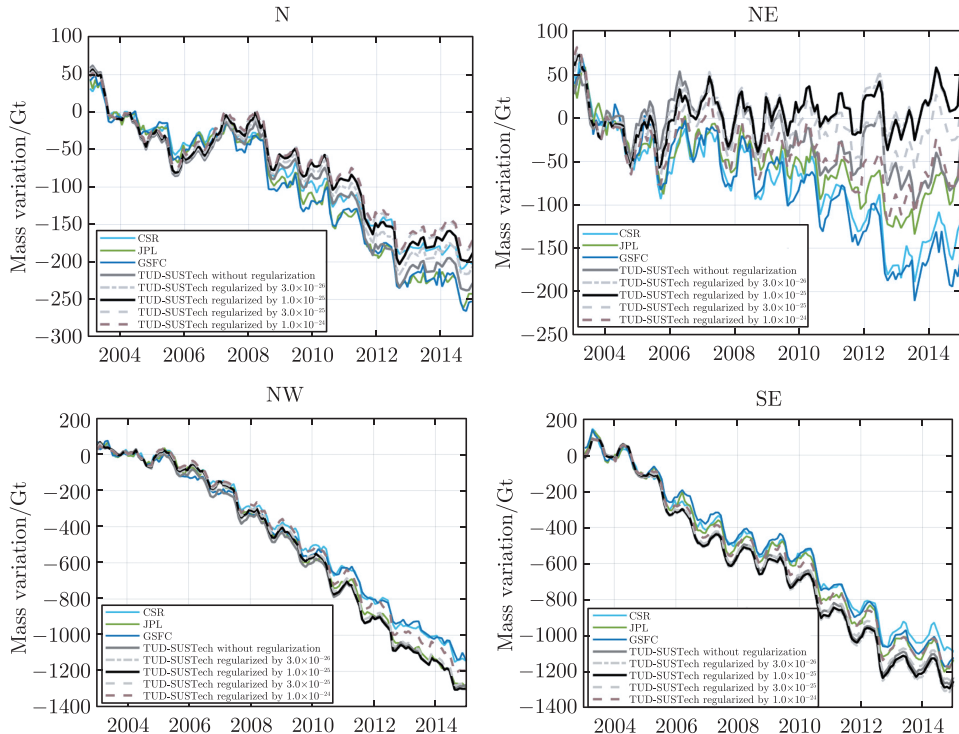


Figure C.4 Similar to Fig. 6.8, but for the N, NE, NW, and SE drainage systems.

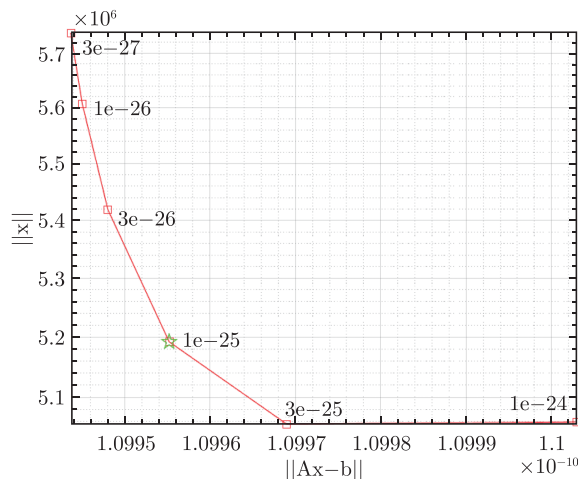
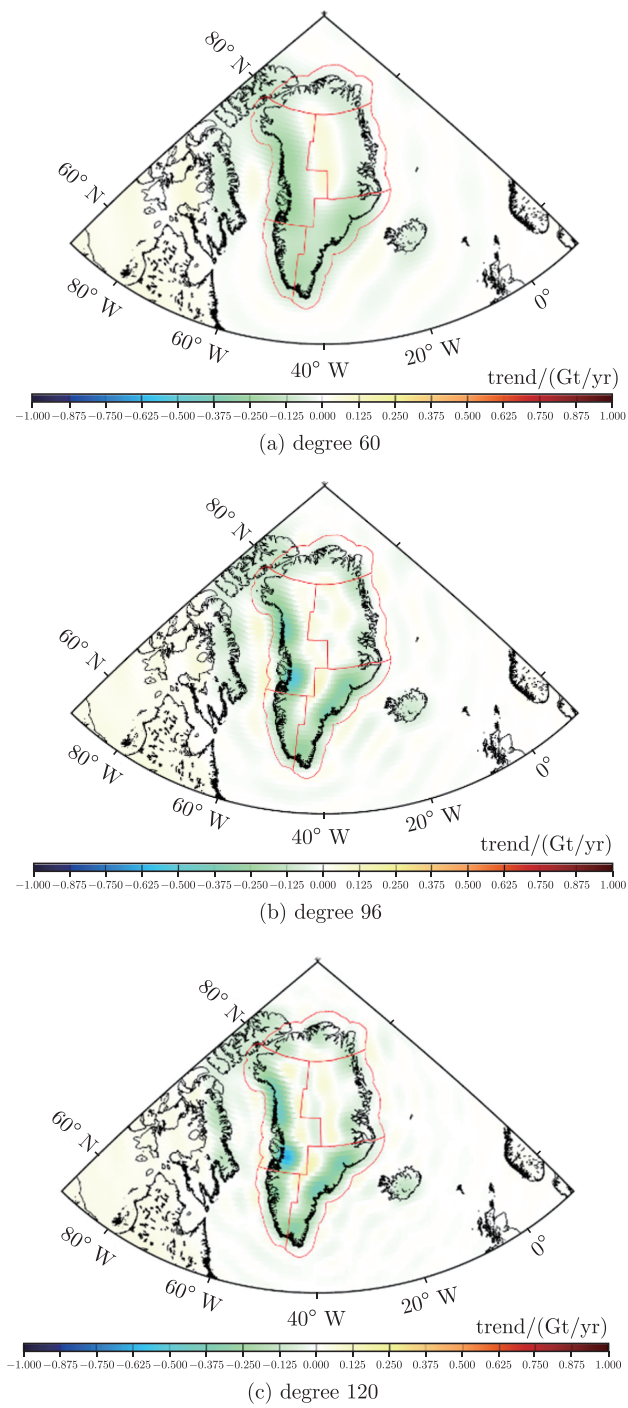


Figure C.5 The choice of optimal regularization factor using L-curve.



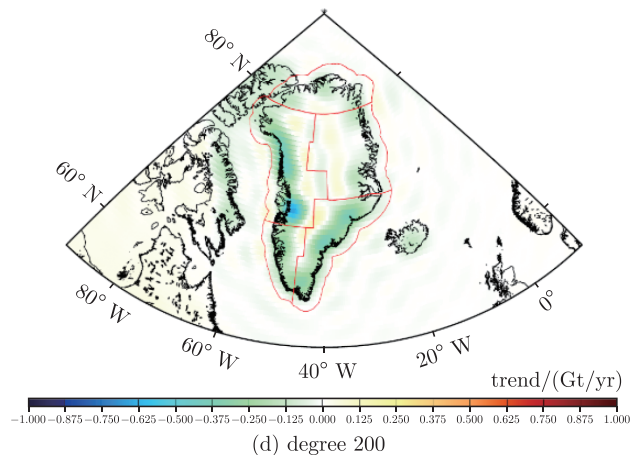


Figure C.6 The trend of Greenland Ice Sheet from GOCO-06S truncated at different degrees: 60, 96, 120, and 200.

